Spin States in Bismuth and Its Surfaces: Hyperfine Interaction

Zijian Jiang

Dissertation submitted to the Faculty of the
Virginia Polytechnic Institute and State University
in partial fulfillment of the requirements for the degree of

Doctor of Philosophy
in
Physics

Jean J. Heremans, Chair
Victoria Soghomonian
Kyungwha Park
Satoru Emori

December 17, 2020
Blacksburg, Virginia

Keywords: bismuth, mica, Si(111), hyperfine interaction, Edelstein effect, nuclear spin polarization, Overhauser field, weak antilocalization.

Spin States in Bismuth and Its Surfaces: Hyperfine Interaction

Zijian Jiang

(ABSTRACT)

The hyperfine interaction between carrier spins and nuclear spins is an important component in exploring spin-dependent properties in materials with strong spin orbit interaction. However hyperfine interaction has been less studied in bismuth (Bi), a heavy element exhibiting a strong Rashba-like spin-orbit interaction in its two-dimensional surface states due to the broken spatial inversion symmetry. In this dissertation we experimentally explore the carrier spin polarization due to transport under strong spin-orbit interaction and the nuclear polarization resulting from the relatively unexplored hyperfine interaction on Bi(111) films. The carrier and nuclear spin polarizations are expected to dynamically interact, a topic with ramifications to other materials where surface states with noteworthy properties play a role. To achieve this goal, an optimized van der Waals epitaxy growth technique for Bi(111) on mica substrates was developed and used, resulting in flat Bi surfaces with large grain sizes and a layered step height of 0.39 ± 0.015 nm, corresponding to one Bi(111) bilayer height. A comparison between Bi(111) films grown on three different substrates (mica, InSb(111)B, and Si(111)) is discussed, for which scanning electron microscopy and atomic force microscopy are applied to obtain the structural and morphological characteristics on the film surface. Magnetotransport measurements are carried out to extract the transport properties of the Bi(111) films. Using the high quality Bi(111) film deposited on mica, we develop quantum magnetotransport techniques as delicate tools to study hyperfine interaction. The approach is based on measuring quantum corrections to the conductivity due to weak antilocalization, which depend on the coherence of the spin state of the carriers. The carrier spin polarization is generated by a strong DC current in the Bi(111) surface states (here called the Edelstein effect), which then induces dynamic nuclear polarization by hyperfine interaction. Quantum transport antilocalization measurements in the Bi(111) thin-films grown on mica indicate a suppression of antilocalization by the in-plane Overhauser field from the nuclear polarization, and allow for the quantification of the Overhauser field, which is shown to depend on both polarization duration and the DC current magnitude. Various delay times between the polarization and the measurement result in an exponential decay of the Overhauser field, driven by relaxation time T1. We observe that in the Bi surface states, the appreciable electron density and strong spin-orbit interaction allow for dynamic nuclear polarization in the absence of an external magnetic field.

Spin States in Bismuth and Its Surfaces: Hyperfine Interaction

Zijian Jiang

(GENERAL AUDIENCE ABSTRACT)

This dissertation focuses on the heavy element bismuth (Bi), a semimetal with strong spin-orbit interaction at its two-dimensional surface. Given the challenge to grow high quality Bi(111) films, we present an optimized van der Waals epitaxy technique to grow Bi(111) films on mica substrates, which show a flat surface with large grain sizes and a layered step height of 0.391 $\pm$ 0.015 nm, corresponding to one Bi(111) bilayer height. To demonstrate the high quality of the Bi(111) surface, a comparison of surface morphology was conducted among Bi(111) films deposited on three different substrates (mica, Si(111), and InSb(111)B), along with a comparison between their electronic transport properties. By applying a DC current on the high quality Bi(111) film on mica, a carrier spin polarization is established via mainly what we here call the Edelstein effect, which then induces dynamic nuclear polarization by hyperfine interaction and generates a non-equilibrium nuclear spin polarization without externally applied magnetic field. We quantified the Overhauser field from the nuclear polarization all-electrically by conducting quantum transport antilocalization experiments, which showed a suppression of antilocalization by the in-plane Overhauser field. Comparative measurements indicated that the magnitude of the Overhauser field depends on the spin-polarizing DC current magnitude and the polarization duration. The experiments also show that antilocalization forms a sensitive probe for hyperfine interaction and nuclear polarization.

Dedication

To my parents and brother.

Acknowledgments

I would like to express my most sincere thanks to my advisor, Prof. Jean J. Heremans, for his continuous support and insightful guidance of my Ph.D. research and study. His professionalism, patience, and humor have influenced my whole doctoral career, leading me to grow as a serious physics researcher. I am also deeply grateful to Prof. Victoria G. Soghomonian, my co-advisor who provided priceless assistance and instructions throughout these years. Her kindness, passion for research, and erudition have inspired me to be meticulous about everything in my research. I wish to thank my committee members, Prof. Kyungwha Park, Prof. Chenggang Tao, and Prof. Satoru Emori not only for serving as my committee members, but also for their brilliant comments and suggestions to my thesis defense. I would like to give my special thanks to our collaborator and committee member Prof. Satoru Emori, who offered many interesting projects that widened my knowledge of condensed matter physics from various perspectives. I would like to thank all my lab colleagues, Dr. Yuantao Xie, Dr. William Rieger, and Adbhut Gupta, for the help they provided and the discussions we shared. My special thanks goes to my ex-roommate Dr. Yuantao Xie, I'm still missing those days when we studied together, did experiments together, and hung out together. I wish to thank my family, because without their spiritual and financial support, I would not have been able to go through the harder times over these years, and this dissertation is dedicated to them.

Contents

List of Figures

List of Tables

Chapter 1

Introduction

Quantum spin physics and spin-dependent transport has led to the exploration of spin-dependent properties in metals, semimetals and bulk or heterostructured semiconductors [15, 16, 17, 18] and spin orbit interaction(SOI) in the solid-state has led to new quantum states of matter [19, 20, 21, 22, 23, 24, 25, 26]. Spin interactions between carriers and local moments form one of the key parameters in spin physics, and among these interactions is hyperfine interaction, referring to the coupling of carrier spins to the nuclear spins. Hyperfine interaction is relatively less studied, particularly in Bi, a heavy element that often appears as constituent of quantum materials of current interest.

1.1 Bismuth and Its Surface States

Bi has strong spin-orbit interaction in its 2-dimensional (2D) surface and interface states (as observed in e.g. Bi/Ag(111)) [27, 28, 29, 30, 31]. The distinctive magnetotransport properties [32, 33] and signatures of electron-electron interactions [34] make Bi valuable to study the science and applications of spin physics in the solid-state. Moreover, thin to ultrathin Bi films have been observed to support 1D edge states with possible topological and spin-dependent properties [35, 36, 37, 38, 39], and 2D bismuthene is of growing interest [40, 41, 42]. Studies of spin-dependent and quantum-coherent electronic transport properties in Bi can help unravel the questions Bi and its surfaces have raised in recent years. A mesoscopic approach emphasizing spin and quantum coherence, combined with quantum transport, and the use of low temperatures (T) and high magnetic fields (B), can help shed light on low-dimensional physics under strong SOI in the presence of other spin interactions, such as hyperfine interaction. For this, thin films are necessary because they allow lithographic patterning, and continued improvement of film quality forms an important part. We note that the surface called Bi(001) in the simplified-hexagonal notation used previously by our group [5, 43], is Bi(111) in the rhombohedral notation [44] which we will use here. Figure 1.1 illustrates the hexagonal structure and the rhombohedral structure of Bi, with C_1 the bisectrix axis, C_2 the binary axis, and C_3 the trigonal axis.

Bi is a semimetal, and the small electron and hole pockets of the bulk Bi Fermi surface produce low and equal electron and hole densities in bulk crystalline Bi, namely both $\sim 3 \times 10^{23}$ m^{-3} for $T \lesssim 30$ K [45]. Somewhat higher but still equal and quite low electron and

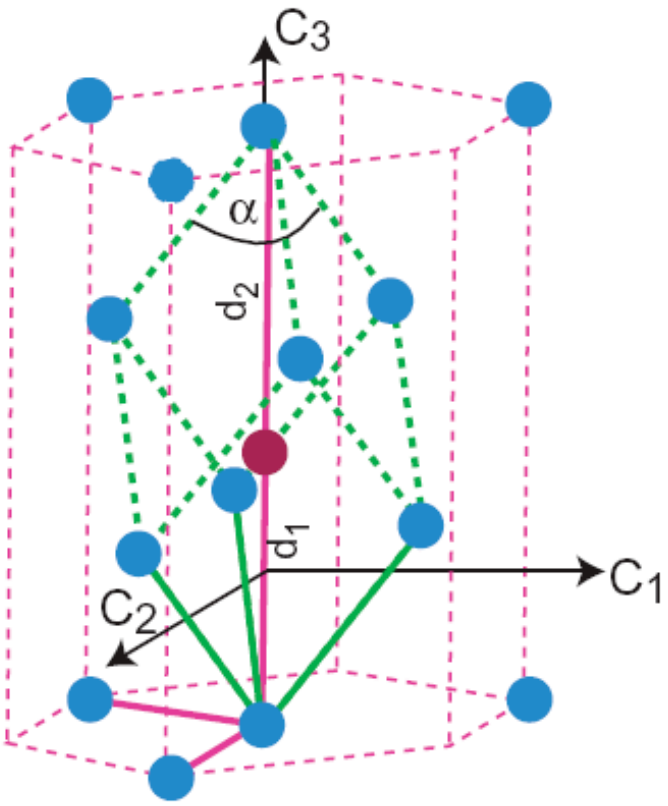

Figure 1.1: Lattice structure of Bi. Dashed green lines denote the rhombohedral unit cell and dashed pink line lines denote the hexagonal unit cell. The solid green and pink lines are the vectors spanning the rhombohedral and hexagonal lattice, respectively. C_3 is the trigonal axis, which is (001) axis in hexagonal notation, and (111) in rhombohedral notation. Sourced from [1] with permission.

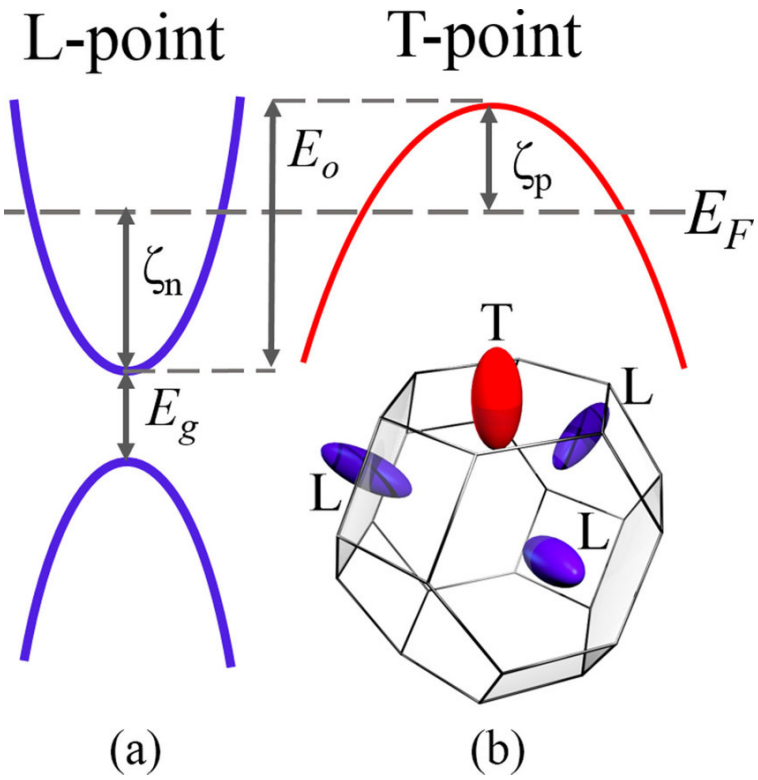

Figure 1.2: (a) Schematic drawing of the bulk band structure of Bi near the Fermi level. There is an approximately $E_o = 40$ meV overlap between the valence and conduction bands. This small overlap makes Bi a semimetal. (b) Simplified Fermi surface of Bi. Semimetallic behavior of Bi is created by SOI, by producing a hole pocket at the $\bar{\Gamma}$(T) point, and three electron pockets at the $\bar{M}$(L) point. Sourced from [2] with permission.

hole densities are observed at higher T, namely both up to $\sim 24.5 \times 10^{23}$ m^{-3} at $T = 300$ K [45]. The low carrier density produces a small Fermi wavevector $k_F \approx 2.1 \times 10^8$ m^{-1} (3D value for $T \lesssim 30$ K). A long Fermi wavelength $\lambda_F \approx 30$ nm (3D value for $T \lesssim 30$ K) also results, making quantization effects in applied B or at reduced dimensions accessible [46, 47]. Carriers in Bi have Dirac properties [34, 48], long mean-free-path (~ 1 mm at 4.2 K) [49, 50], and large SOI. Bi nanowires [51, 52, 53, 54] have yielded insights, but quantum transport in purpose-made mesoscopic Bi geometries has not been extensively studied [5, 55, 56], which is where one of our innovative contributions lies. SOI creates the semimetallic behavior in bulk Bi by producing a hole pocket at the T point, elongated along the trigonal axis, and three electron pockets with their long axes almost in the (111) plane of the film, as shown in Figure 1.2(b), which leads to an approximately 40 meV overlap between the valence (T point) and conduction (L point) bands, illustrated in Figure 1.2(a) as E_0. The semimetallic behavior of Bi comes from this small overlap. The effective masses of the electrons and holes in bulk Bi are extremely small ($\sim 0.001\ m_e$, where m_e is the free-electron mass), which leads to very large mobilities at low temperatures ($\sim 10^3$m^2/Vs).

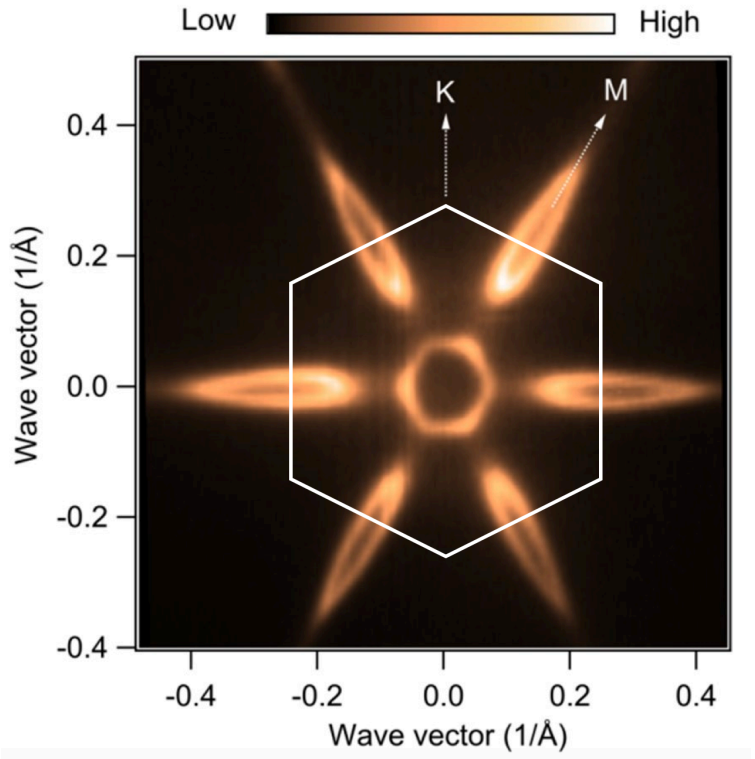

Figure 1.3: The Bi(111) 2D Fermi surface contains a central electron pocket at the central T point and six hole ellipses at the L points. Compared to Figure 1.2(b), the carriers have flipped their positions from bulk Bi. Sourced from [3] with permission.

Spatial inversion symmetry exists in the bulk but is broken normal to a surface yielding two Rashba-like surface spin subbands. The Bi(111) surface hosts a surface band [1] centered around the surface-$\bar{\Gamma}$ point [57] occupied by electrons (as shown in Figure 1.3), and spin-split by Rashba-like SOI [1, 28, 29, 44, 58]. Transport experiments have noted the role of surface states [5, 53, 54, 59, 60]. The surface 2D carrier density N_S is estimated at 0.2-2 $\times$ 10^{12} cm^{-2} [53, 60], and the effective mass m^* at 0.4-0.8 m_e (where m_e is the free-electron mass) with the very high but anisotropic Rashba parameter α averaging to $\alpha \approx 1 \times 10^{-10}$ eVm [27, 28, 29]. Evidence exists to classify Bi(111) surfaces as 2D topological insulators with concomitant edge states [35, 36, 37, 38]. Complications are that 6 small spin-split hole surface pockets exist also [1] (as shown in Figure 1.3) and that the transport data may contain Bi surface and semimetallic bulk contributions [5, 52, 53, 59].

1.2 Spin-Orbit Interaction and Quantum Transport

SOI in solids originates from a spatial asymmetry (from an effective electric field **E**) interacting with the carrier spin and momentum. For instance in semiconductor heterostructures,

Rashba-type SOI [27, 61, 62, 63, 64] occurs due to the symmetry breaking normal to the plane of the carrier layer, and the same effective electric field creates carrier confinement. At surfaces and interfaces, where asymmetry in the carrier potential exists due to crystal termination, a Rashba-like term can exist, as is the case for Bi [1, 27, 28, 29, 31, 44, 58, 65, 66, 67, 68]. In III-V semiconductors, also a Dresselhaus SOI term [69] occurs due to crystalline inversion asymmetry.

Yet, a Rashba-like term linear in momentum dominates on the Bi(111) surface with its surface band [1]. The Rashba energy dispersion can [62] be written as:

$$E(k) = \frac{\hbar^2 k^2}{2m^*} \pm \alpha k. \tag{1.1}$$

Here $\mathbf{k}$ denotes the wavevector in the plane of the 2D carrier system (*i.e.* in the plane of the surface states). The $\pm$ distinguishes the two spin subbands, and α is the Rashba parameter. The spin-splitting at the Fermi wavevector k_F (associated with Fermi energy E_F) is then $2\alpha k_F$. The surface α for Bi(111) surface states is anisotropic, but can reach up to $\alpha \approx 3.5 \times 10^{-10}$ eVm (in Bi/Ag(111) surface alloys) [27, 28, 29, 31, 65], much larger than for the InSb-, InAs- and InGaAs-based heterostructures that have formed the subject of prior transport-based studies of Rashba SOI, including by our group before (3×10^{-12} eV m [70, 71, 72, 73] for InSb; α up to $8{\times}10^{-12}$ eVm for InAs [73, 74, 75]; $\alpha \approx 1.5...15{\times}10^{-12}$ eVm for InGaAs). Because Bi has inversion symmetry in the bulk, Dresselhaus SOI is absent.

Under Rashba-type SOI, the magnetic moment μ due to a carrier spin will tend to lie normal to $\mathbf{E}$ and $\mathbf{k}$. This spin-momentum locking by SOI is expressed in an effective B, $\mathbf{B}_{SOI}$, dependent on $\mathbf{k}$, for Rashba SOI given by $B_{SOI} = \frac{2\alpha k_F}{g\mu_B}$, where μ_B is the Bohr magneton and g the g-factor. $\mathbf{B}_{SOI}$ locks the spin precession axis normal to $\mathbf{E}$ and $\mathbf{k}$, and will tend to align spin $\parallel \mathbf{B}_{SOI}$. For Rashba-type SOI, $\mathbf{B}_{SOI}$ lies in the plane of the carriers (i.e. in the Bi(111) plane) and normal to $\mathbf{k}$. As order of magnitude for Bi(111), $B_{SOI} \approx 300$ T, a very high field commensurate with the strong SOI.

The strength of the SOI (here Rashba parameter α) can be determined by quantifying its effect on spin decoherence using quantum transport techniques. In particular, our group has used the weak-localization (WL, Figure 1.4(a)) and weak-antilocalization (WAL, Figure 1.4(b)) quantum corrections to the conductivity to determine quantum phase (i.e. orbital) and spin coherence properties of materials and mesoscopic structures [5, 70, 75, 76, 77, 78, 79, 80, 81, 82].

The corrections result from quantum interference of electron waves on exact time-reversed trajectories at low T ($< \sim 10$ K) [63, 76, 77, 78, 79, 80]. In a disordered system, for a localized but randomly scattered electron, pairs of time reversed propagating trajectories should always exist, and they interfere quantum-mechanically with each other. In the absence of SOI, time-reversed paths have the same phase accumulation and same probability amplitudes, which leads to a constructive interference and the electron is more likely to be localized, resulting in an increase in the resistance at low B. A perpendicularly applied

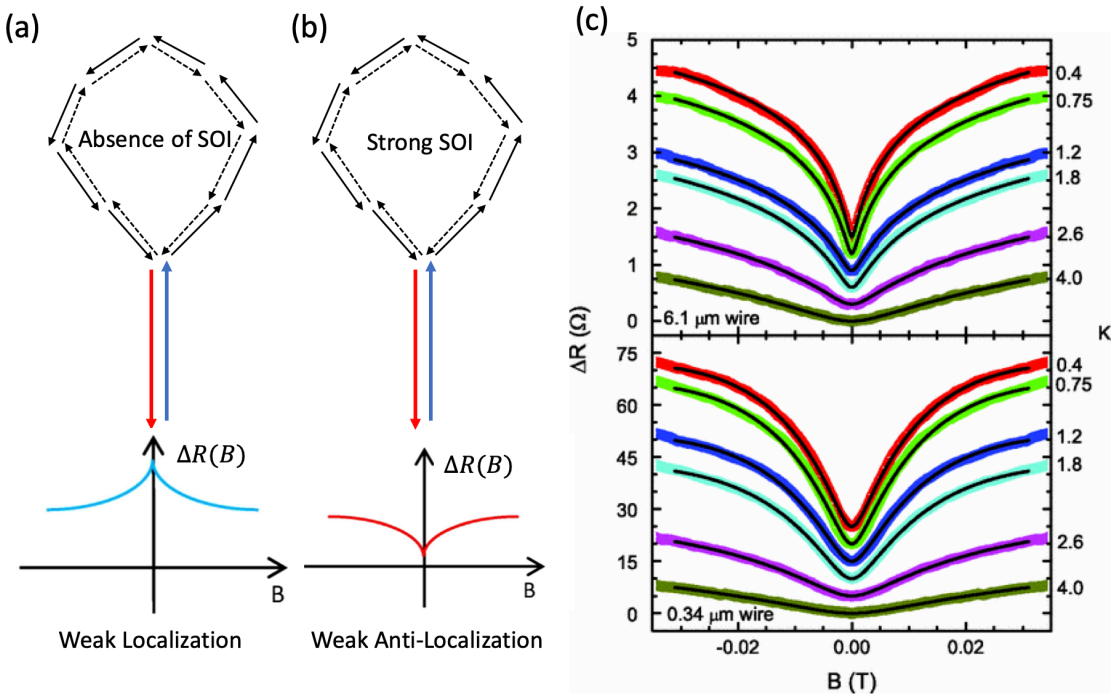

Figure 1.4: (a) Weak localization occurs due to constructive interference along time-reversed paths in the absence of SOI. (b) Weak anti-localization occurs due to destructive interference along time-reversal paths in the presence of strong SOI. (c) MR (offset) due to WAL, characteristic of SOI, in a wide Bi region (top) and a Bi wire of width 340 nm (bottom), parametrized in temperature T. The quantum correction characteristically fades with increasing T. Color lines are experimental data, black lines a fit to [4] (sourced from [5] with permission).

B creates an Aharonov-Bohm phase and yields the distinctive negative magnetoresistance (MR, resistance R vs B) [63, 83] of WL, decreasing the resistance, as shown in Figure 1.4(a). In systems with strong SOI, the locking between electron spin and momentum results in opposite electron spin directions between a pair of time-reversed paths. In this case the interference between time-reversed paths is destructive at low B, causing low resistance. When an external B is applied, the time-reversal symmetry breaking will weaken the quantum interference effect, increasing the resistance. So this strong SOI promotes destructive spin interference [63, 83] and induces WAL, characterized by positive MR at low B (Figure 1.4(b)). The MR from WAL depends on quantum and spin coherence and can be used to quantify the orbital quantum phase coherence length L_ϕ, the SOI-limited spin coherence length L_{SO} [4, 14, 63, 76, 77, 78, 84, 85], and the magnetic spin-flip length L_S due to interaction with magnetic species [78, 79, 82, 84, 85]. The literature contains theoretical models [4, 14] of WAL to which the data can be fitted (Figure 1.4(c)) to obtain values for these lengths, and values are grouped within $\sim 30\%$ model-to-model. For unpatterned Bi thin films grown on SiO_2, our group typically measures $L_\phi \approx 0.8$ nm and $L_{SO} \approx 80$ nm at $T < 1$ K [5, 43]. Electron-electron interactions have a strong effect on L_ϕ [86, 87, 88, 89, 90], while their effect on L_{SO} is less studied.

To asses the phase coherence length L_ϕ and the SOI spin coherence length L_{SO}, it is necessary to first calculate other transport properties of Bi films or mesoscopic structures. The carrier densities and mobilities are obtained through van der Pauw and Hall measurements, whose setups are indicated in Figure 1.5. Since Bi is at minimum a two-carrier system containing both electrons and holes, we use a two-carrier model to describe the relations among resistivity, carrier mobility, and carrier density:

$$\rho_{xx} = \frac{1}{e}\frac{(n\mu + p\nu) + (n\mu\nu^2 + p\nu\mu^2)B^2}{(n\mu + p\nu)^2 + \mu^2\nu^2B^2(p-n)^2}, \tag{1.2}$$

$$\rho_{xy} = \frac{1}{e}\frac{(p\nu^2 - n\mu^2) + \mu^2\nu^2B^2(p-n)}{(n\mu + p\nu)^2 + \mu^2\nu^2B^2(p-n)^2}B, \tag{1.3}$$

where n and p are electron and hole densities, μ and ν are electron and hole mobilities. By fitting the magnetoresistance $R_{xx}(B)$ using equation (1.2) and fitting $R_{xy}(B)$ using equation (1.3), we can obtain carrier densities and mobilities, and other transport properties can be determined accordingly, as shown in Table 1.1.

We organize our dissertation as follows. Chapter 2 describes the improved growth of Bi(111) films on different substrates (*e.g.*, InSb, Si(111), mica), where the growth methods on each substrate will be discussed in detail. In chapter 3, we characterize the Bi(111) films on those substrates by the surface morphology, the transport properties, and quantum phase coherence properties of the films. Atomic force microscopy (AFM) and scanning electron microscopy (SEM) are used to obtain Bi(111) film surface images, and quantum transport and quantum coherence properties of Bi(111) films with variable thicknesses are illustrated.

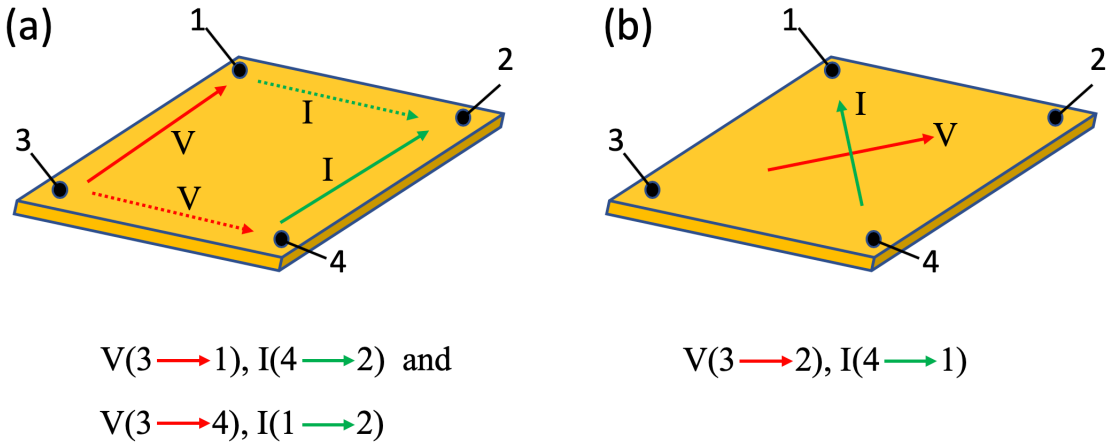

Figure 1.5: (a) Van der Pauw measurement setup on a sample film with four contacts. In a lock-in amplifier measurement, by applying an AC current along one side of the sample, an AC voltage difference will be measured on the other side. Both R_a and R_b are quantified by $\frac{V}{I}$. (b) Hall measurement setup. A magnetic field $\mathbf{B}$ will be applied perpendicular to the sample surface.

Table 1.1: Transport properties

transport property	**definition**
τ_0	The elastic scattering time, describing a process in which the carrier's momentum eigenstate is conserved, $\tau_0 = \frac{\mu m^*}{e}$
$R_\square$	Sheet resistance ($\Omega/\square$), $R_\square = \frac{ne^2\tau_0}{m^*}$
ρ	Resistivity, $\rho = R_\square d$, with d the thickness of a sample
k_F	Fermi wavevector, in 2D: $n = \frac{k_F^2}{2\pi}$
v_F	Fermi velocity, $v_F = \frac{\hbar k_F}{m^*} = \frac{\hbar\sqrt{2\pi n}}{m^*}$
l_0	Electron mean free path, the distance travelled by an electron between successive collisions, $l_0 = v_F\tau_0$
D	Diffusion coefficient, $D = \frac{1}{2}v_F l_0 = \frac{1}{2}v_F^2\tau_0$
λ_F	Fermi wavelength, in 2D: $\lambda_F = \sqrt{\frac{2\pi}{n}}$
l_ϕ	Quantum phase coherence length, the average length for the carrier's eigenstate to be conserved, $l_\phi = \sqrt{D\tau_\phi}$, where τ_ϕ is the phase coherence time
l_{SO}	Spin-orbit coherence length, the average length in which the propagating spin of the carrier remain unchanged, $l_{SO} = \sqrt{D\tau_{SO}}$, where τ_{SO} is the spin-orbit coherence time

In chapter 4, a study [91] of hyperfine interaction (HI) and dynamic nuclear polarization (DNP) is discussed. There the Edelstein effect and HI are used to establish a net local nuclear spin polarization (NP) by DNP. We studied the effect of the NP on the carriers using quantum transport approaches sensitive to carrier spin coherence and the effective Zeeman fields induced by HI [91]. Chapter 5 lists some other published papers and our contributions in those work.

Chapter 2

Bi Film Growth and Low-Temperature Techniques

Bi single crystals of high crystalline quality and high purity are relatively straightforwardly obtained by careful melting and crystallization. However when it comes to growth of high quality Bi(111) films, the story is different. A variety of methods have been applied to grow Bi(111) thin films on different substrates, including thermal evaporation deposition [5, 8, 36, 43, 92, 93, 94], pulsed laser deposition (PLD) [95], and molecular beam epitaxy (MBE) [47, 96, 97, 98], among which thermal evaporation and MBE are the two most popular ones. We note that most often thin film growth will present a Bi(111) surface (trigonal axis perpendicular to the film plane and substrate). The work presented in this dissertation chose to use thermal evaporation deposition method. The details about the growth system are illustrated in Appendix A.

Bi was previously deposited on SiO_2 substrates [5, 43] by our group. AFM and XRD show that the films have ~ 1 μm sized crystals oriented with the trigonal axis perpendicular to the substrate and random in-plane [55] such that the surface orientation is Bi(111) [44]. The Bi growth on SiO_2 showed that Bi growth starts with island formation [43], where continuous films do not arise until a 20 nm thick film is deposited. High quality Bi layers can grow on SiO_2 on top of a 20 nm Bi wetting layer, leading to a two-stage deposition process [5, 43]. It was determined that for films thicker than 80 nm, the transport properties of the disordered wetting layer (as a shunt) can reasonably be ignored. A 3-carrier transport analysis (active electrons and holes, and 20 nm wetting layer) yields 3D carrier densities n or p and mobilities μ or ν, with electrons at $n = 2.5\times10^{23}$ m^{-3} and $\mu = 0.3$ m^2/Vs and holes at $p = 1.4\times10^{23}$ m^{-3} and $\nu = 0.4$ m^2/Vs (nearly compensated, as in the bulk). And it was confirmed that Bi forms a ~ 2 nm thick high-quality native oxide, not affecting the surface states' transport properties [44].

This chapter introduces continued improvement of film quality by growing Bi(111) films on different substrates under variable conditions. We explored and developed the use of high quality Bi(111) films grown on InSb(111)B, Si(111), and mica as substrates. We first explain and describe the Bi(111) film growth method on the three substrates (Section 2.1,2.2,2.3), especially for Bi(111) growth on mica. We will show how we succeeded in obtaining Bi(111) film flakes in μm size. In addition to the fabrication technique, we will also present our low-temperature (4 K and 0.4 K) measurement techniques in this chapter.

2.1 Bi(111) Growth on InSb(111)B

For Stranski-Krastanov epitaxial growth, the choices of substrate to grow Bi(111) are always limited by the surface dangling bonds, lattice mismatch, surface states and the ability to clean the surface. Especially a smaller lattice mismatch between Bi and the substrate plays an important role to prevent pseudomorphic growth because of the existence of absorption-active centers (i.e., dangling bonds) on the surfaces [99]. The in-plane lattice mismatch between Bi and InSb(111)B is only 0.8% (in-plane hexagonal lattice constant 4.48 Å for Bi(111) as shown in Figure 2.1(b), 4.58 Å for InSb(111), as shown in Figure 2.1(a)), making InSb(111)B a desirable substrate to grow Bi(111) films.

The atomic planar structure of Bi(111) [100] emulates the InSb(111) zinc-blende structure such that the growth direction of Bi on InSb(111)B is parallel to the trigonal axis of Bi, yielding Bi(111) as desired. The parallel conduction through the substrate is of greater concern than for growths on SiO_2, but has proven manageable (conductance of Bi layer $\sim 10\times$ larger than InSb substrate at low T). We note that similar growth of Sb on GaSb(111) [101] and Sn on InSb(111) [102, 103] is presently pursued in other groups. InSb(111)B is a fairly polar surface, which may narrow the parameter space in growth temperature and growth rate in which smooth growth of Bi(111) can occur (as our preliminary results show).

The InSb(111)B wafer is first cleaved to square or rectangular pieces by using a carbide pen. When scoring the substrate wafer, a piece of clean lens paper should be put between the wafer and a piece of glass. When using a finger to press the top side of the wafer, again the lens paper should be used to avoid any contact between the substrate surface and skin. We clean the substrate to remove any organic contaminants from the surface by using trichloroethylene (TCE), acetone (ACE), and isopropanol (IPA) in sequence, rinsing for 3 minutes in each. The substrate is then blown dry with N_2 and put into a clean container. We prepare the InSb(111)B face with (2×2) reconstruction by heating it under ultra high vacuum for 5 hours at 300 °C [103]. The surface reconstruction is indicated by Figure 2.1. The source Bi (99.9999%, so 6N pure) is thermally evaporated under 1×10^{-8} Torr onto InSb(111)B surface. A 20 nm thick Bi film is deposited at rate of 0.45 Å/s and substrate temperature of 100 °C as the wetting layer and another 55 nm thick (active) layer is grown on top of the wetting layer at 250 °C [5] at the same growth rate. To increase the grain size and decrease surface roughness, post-growth annealing is carried out, with sample temperature 250 °C for 2 hours (cfr Chapter 3).

To perform transport measurements on the film, we need to connect the Bi device to a 14 dual-inline package (DIP) header. We first make electrical contacts in each corner on the sample by melting Wood's metal, which is an eutectic alloy of 50% bismuth, 26.7% lead, 13.3% tin, and 10% cadmium by mass, with melting point 70 °C. When melting Wood's metal, we set the temperature of soldering iron at about 130 °C, which is much lower than the melting point of Bi (271 °C). Then Au wire is soldered to each contact on the film, we glue the Bi device to a DIP header and solder the free ends of the Au wires to the DIP

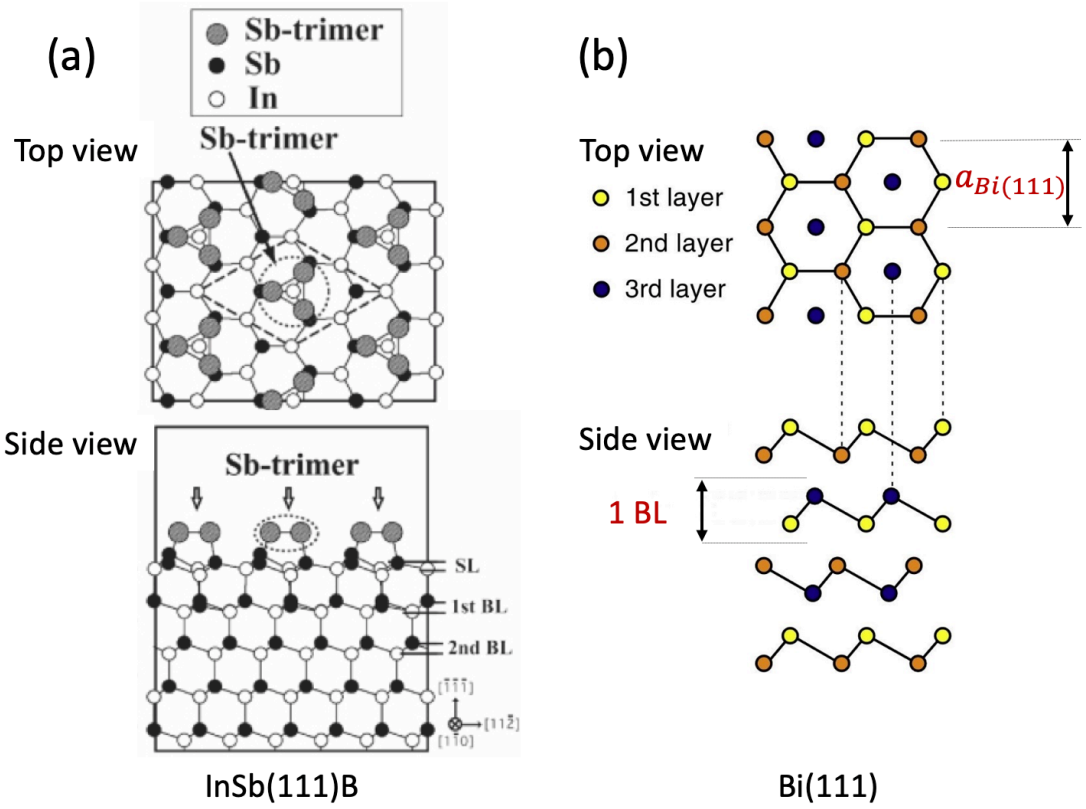

Figure 2.1: (a) Top view and side view of InSb(111)B 2×2 reconstruction, indicated by dashed lines. Sourced from [6] with permission. (b) Top view and side view of Bi(111), with lattice constant $a_{Bi(111)} = 4.48$ Å, bilayer height 1 $BL_{Bi(111)} = 3.9$ Å.

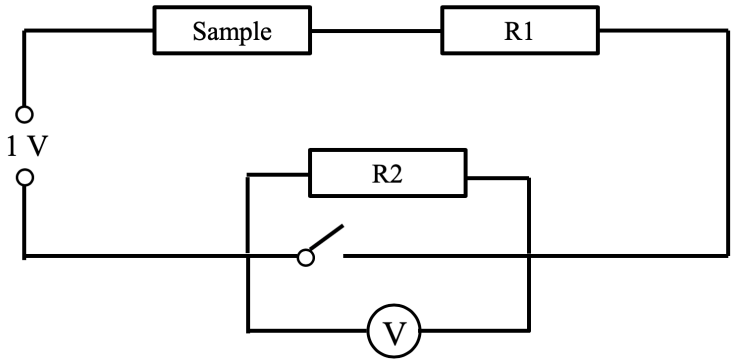

Figure 2.2: Circuit for contact testing.

header pins with In, whose melting point is 156.6 °C (the soldering iron is set to about 250 °C here). After trimming the extended Au wires, the DIP header with the Bi device is tested to make sure the contacts are connected well. The device packaging procedure is the same for all the Bi(111) films grown on different substrates.

Before taking quantum transport measurements on the sample, the stability of the contacts needs to be tested, using a simple serial circuit. The circuit is shown in Figure 2.2, where the resistor R1 can be adjusted to from 100 KΩ to 1 GΩ (10 MΩ is used most often). The value of R2 is 10 KΩ, the 1 V rms AC voltage source is given by a lock-in amplifier and the voltage measurement uses the same lock-in amplifier. Each time we test two contacts which are connected to the circuit, and the resistance between the two contacts is expected to be about several hundred Ohms. If the tested contacts on the sample are usable and Ohmic, then the measured voltage across R2 should be very close to 1 mV when the switch is open, while a smaller voltage (< 0.95 mV) means the contacts are non-Ohmic. This contact testing method applies to all the Bi(111) samples.

2.2 Bi(111) Growth on Si(111)

We also pursued the use of Si(111) as substrate. Growth of Bi(111) or other Bi allotropes on Si(111) has been explored in the literature [8, 36, 58, 98, 104, 105, 106] especially for the growth of ultrathin Bi(111) films. Though the lattice mismatch between Bi(111) and Si(111) is large ($a_{Bi(111)} = 4.48$ Å, $a_{Si(111)} = 3.84$ Å), there is a magic lattice mismatch between them:

$$6 \times a_{Bi(111)} = 7 \times a_{Si(111)}, \tag{2.1}$$

as shown in Figure 2.3, leading to the surprisingly perfect alignment of Bi(111) phase on the Si(111) 7×7 reconstructed surface [8].

The four stages of the deposition of Bi(111) on Si(111) 7×7 surface have been described in [8]. As shown in Figure 2.4 (a) - (d), stage I occurs when the thickness is less than 2 ML of Bi{012}, with 1 ML of Bi{012} = 0.318 nm. In this stage, small islands of Bi{012} start to be formed, with the islands height 6.6 to 13.0 Å. Stage II (2-4 ML) shows the connection between the small islands to form larger islands of Bi{012} phase. The relationship between the surface stability and the number of Bi{012} layers has been discussed in [8], revealing that even-number layer Bi{012} film is very stable and forms a very flat surface. Bi(111) surface appears in the third stage (4-6 ML), and due to the stability of Bi{012} phase, the transformed Bi(111) phase is observed in STM with a very smooth surface [8]. The Bi{012} phase totally disappears in stage 4 (> 6 ML), resulting in a very smooth Bi(111) film morphology.

In contrast to most work using Si(111), we are less interested in the Bi{012} phase (which survives up to thicknesses of ∼ 2 nm), but rather in the hexagonal Bi(111) phase appearing at higher thicknesses, because the Bi(111) phase represents bulk Bi properties and because quantum transport in the ultrathin Bi films characteristic of the Bi{012} phase presents difficulties that will obscure the present specific objectives. To flash off the SiO_2 layer and to prepare the Si(111) 7×7 reconstruction as starting point for Bi deposition, we recently built a new Bi growth stage capable of stable temperature control up to 1250 °C in UHV conditions, as shown in Appendix A.

Before the deposition of Bi on Si(111), Si(111) wafers were cut to 0.4 cm × 0.4 cm squares which were cleaned outside the vacuum chamber with TCE, ACE and IPA. The Si(111) 7×7 reconstruction was prepared by a pure annealing treatment inside the chamber under 1×10^{-8} Torr : (i) The Si(111) sample was outgassed at 600 °C for 5 hr to remove the oxide layer. (ii) Substrate temperature was raised rapidly to 1200 °C (in less than 3 min), flashing the sample for 2 min. (iii) The sample surface was cooled down slowly to avoid $\sqrt{3} \times \sqrt{3}$ reconstruction [8, 93, 94]. Bi was deposited onto the Si(111) 7×7 surface at room temperature, at a rate of 0.35 BL_{111} /min (∼ 0.14 nm/min) [8, 94]. The deposition rate and film thickness were measured by a quartz microbalance monitor to within an accuracy of < 5 %. To increase the grain size and decrease the surface roughness of Bi(111) surface, the film samples were annealed at 95 ± 5 °C for 1 hr (cfr Chapter 3) and then left in the chamber to cool before venting with dry nitrogen. We tried different annealing temperature ranging from 80 °C to 120 °C, and we will discuss how annealing affects the surface morphology in Chapter 3.

2.3 Bi(111) Growth on Mica

The van der Waals epitaxy (vdWE), a method developed by Koma et al. [107, 108, 109, 110, 111, 112], opens up a new route to heteroepitaxy without considering the lattice mismatch due to the lack of covalent bonding across the van der Waals gap of Bi and the substrate. In conventional Stranski-Krastanov epitaxial growth, the bonding or interaction between

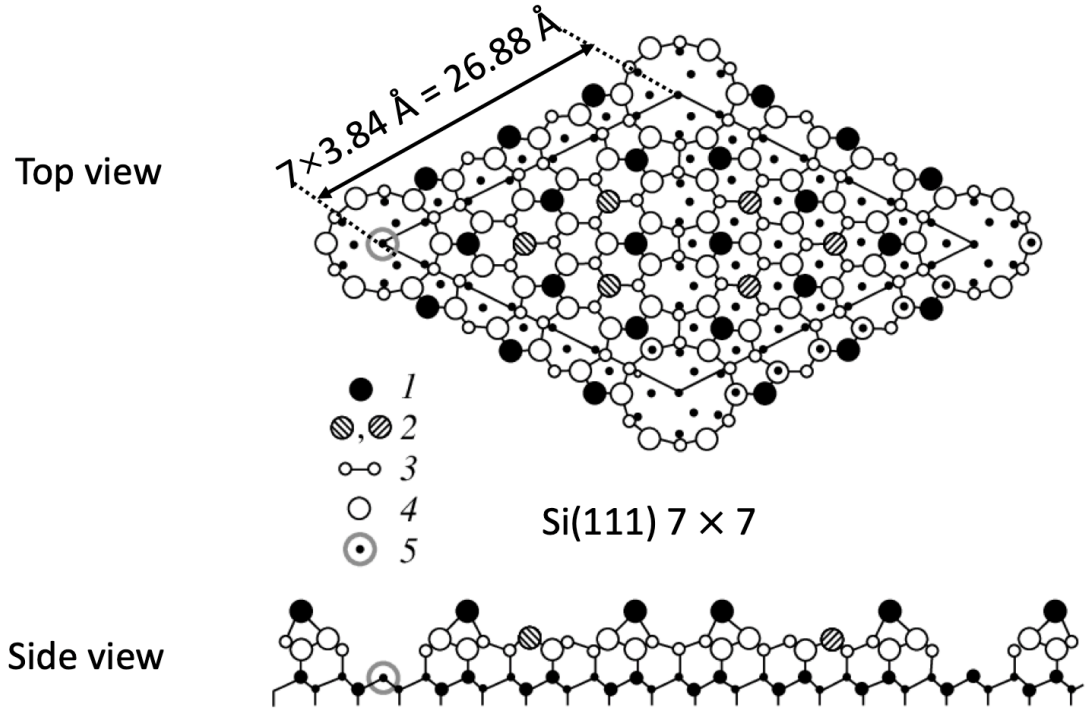

Figure 2.3: (a) Top view and side view of Si(111) 7×7 reconstructed surface. 5 different kinds of atoms are defined by their unique positions. only adatoms 1 and rest atoms 2 have dangling bonds. Sourced from [7] with permission.

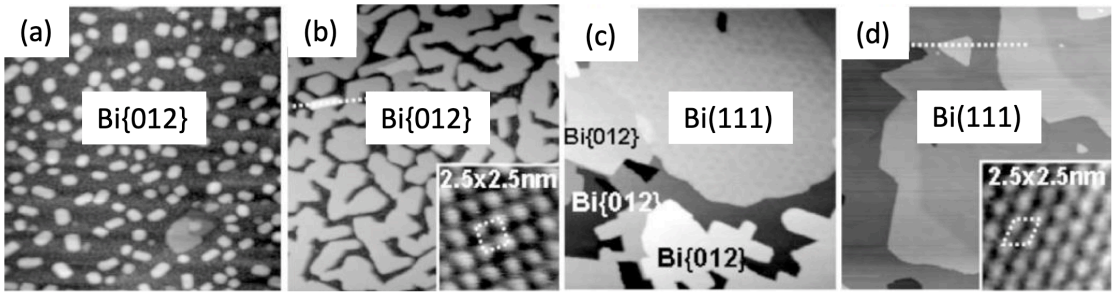

Figure 2.4: STM images of four stages of Bi deposition on Si(111) 7×7 taken by [8] at RT: (a) stage I (< 2 ML), (b) stage II (2 - 4 ML), (c) stage III (4 - 6 ML), and (d) stage IV (> 6 ML). Sourced from [8] with permission.

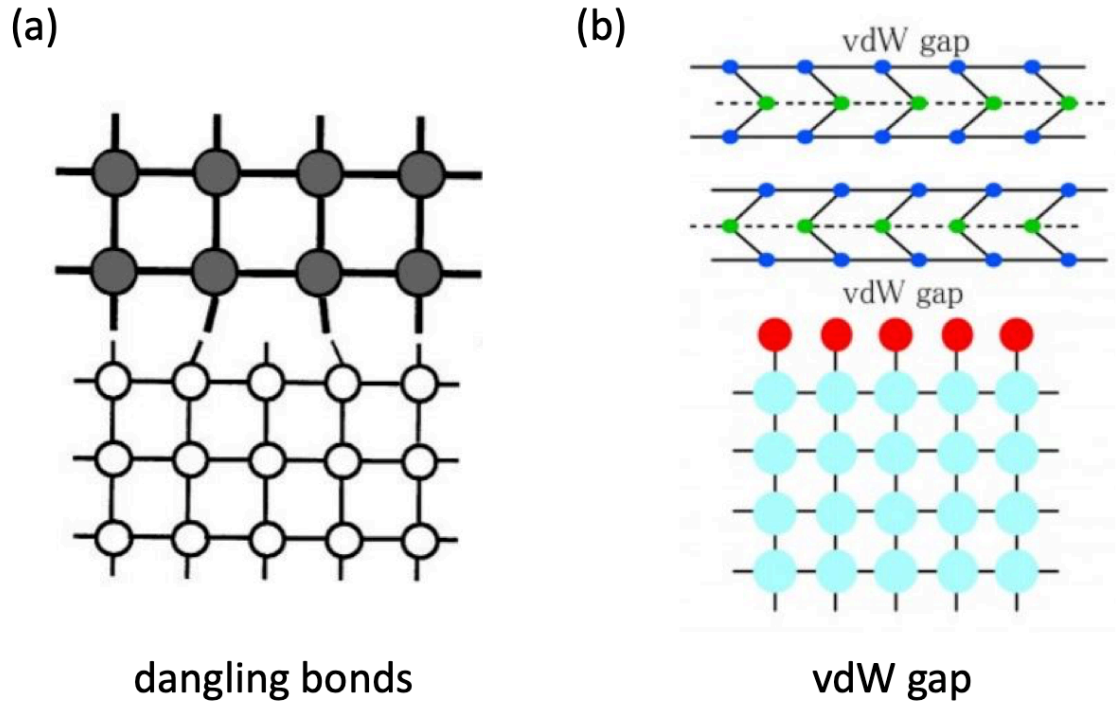

Figure 2.5: (a) Dangling bonds between film surface and the substrate when both of them have dangling bonds. (b) Van der Waals gap when one of the materials doesn't have dangling bonds. Sourced from [9] with permission.

the substrate and epilayer is often covalent or ionic; however, in vdWE the interaction is non-bonding and hence weak, where the substrate and/or the epilayer possess a van der Waals surface without dangling bonds, realized in 2D materials with naturally completely terminated surfaces, such as graphene and mica [113]. The interfaces connected by dangling bonds and van der Waals gap (vdW gap) are shown in Figure 2.5 (a) and (b). The weak vdW gap usually results in a clean and flat surface on the films. Epilayers of Sb, Ge and Ge/Sb on mica show high crystalline quality [99, 114], leading to mica as the substrate for the present Bi thin film growth.

Muscovite mica can be easily cleaved along the {001} planes by using a tape due to its weak vdW gap interfaces, resulting in a very flat surface. The {001} surface structure is shown in Figure 2.6, which is associated with the chemical formula $KAl_2(Si_3Al)O_{10}(OH)_2$, and the top layer (2.6 (b)) shows a quasi hexagonal arrangement, with the lattice constant a_{mica} = 519 pm, b_{mica} = 904 pm [111]. Even though epitaxial Bi layer has considerable lattice-mismatch with mica substrate, due to the weak interaction between the deposited Bi layer grows unstrained at the outset, with a lattice constant of a_{Bi} = 448 pm, the bulk lattice constant of Bi in a plane normal to the trigonal axis.

Before deposition, the mica substrate is freshly cleaved by a tape, and to remove absorbed

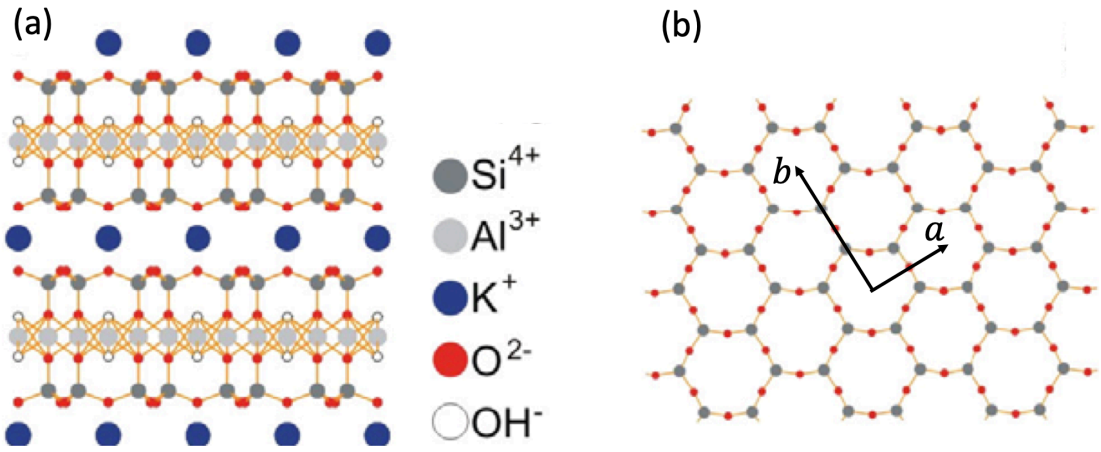

Figure 2.6: Side view (a) and top view (b) of muscovite mica {001} surface. The {001} surface top layer in (b) shows a hexagonal arrangement, with $a = 0.519$ nm, $b = 0.904$ nm. Sourced from [10] with permission.

surface water, the mica substrate was preheated at 250 °C for at least 24 hr under ultra-high vacuum. Then Bi was thermally evaporated at a base pressure of 10^{-8} Torr at room temperature through an Al shadowmask with apertures of diameters ~ 500 μm which was placed on the mica surface (see Figure 2.7 (a)). Varying thicknesses of Bi were deposited at a rate of 0.35 BL_{111} /min (~ 0.14 nm/min). To increase the grain size and decrease the surface roughness of Bi(111) surface, the film samples were annealed at 95 $\pm$ 5 °C for 1 hr (cfr Chapter 3) and then left in the chamber to cool before venting with dry nitrogen. On the resulting shadowmasked Bi film samples of diameter ~ 350 µm, photolithographically patterned Au was applied as contacts with a representative distance of 25 μm between two contacts (see Figure 2.7 (b)). The whole procedure of making such Bi(111) film flakes is described in Figure 2.8.

The reason why we use small Bi(111) film flakes is that quantum transport on the whole film seems to be dependent on how the whole film stays together. Though the cleaved surface of mica is very flat, some cracks still appear on the surface due to its fragility, leading to unrepresentative transport results on the grown Bi film. Before we carried out the shadow mask growth, we had also tried PMMA transfer and PDMA stamp methods to obtain a Bi(111) film flake. Researchers working with graphene and 2D materials (MoS_2 etc.) often use small flakes or grains. They put many flakes or grains on a substrate (e.g. SiO_2 or other), use SEM to find a good flake or grain, and at the same time use electron beam lithography to make contacts to the chosen flake or grain. We had decided to fabricate Bi(111) film flakes accordingly, by using two popular methods: PMMA and PDMS transfer. For PMMA transfer (Figure 2.9), first we spin-coat PMMA on Bi(111) grown on mica, and then use ultrasonic agitation for 2 min in water, then peel off Bi(111) from mica with water assist and then use acetone to remove the PMMA and transfer the Bi(111) film flake on our target

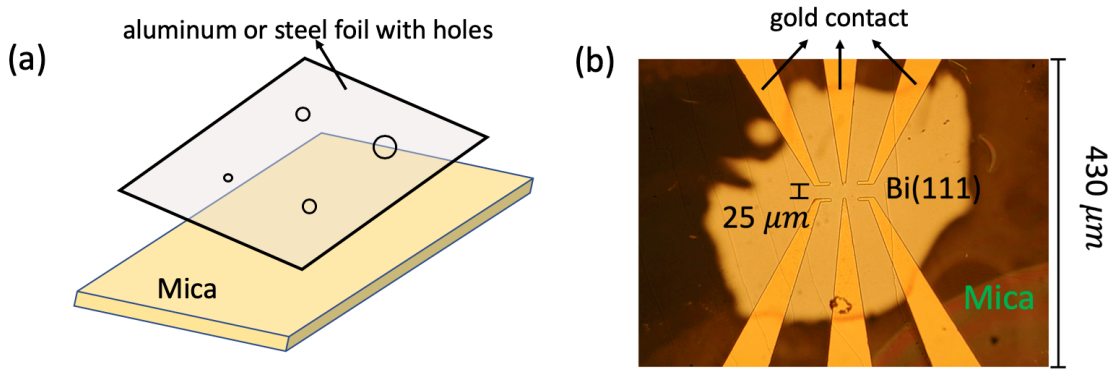

Figure 2.7: (a) Schematic description of growth of Bi(111) film on mica through an Al shadowmask. (b) Optical micrograph of Bi film samples grown on mica by van der Waals epitaxy, with lithographic Au contacts. The diameter of the sample is $\sim$ 350 μm; distance between contacts $\sim$ 25 μm.

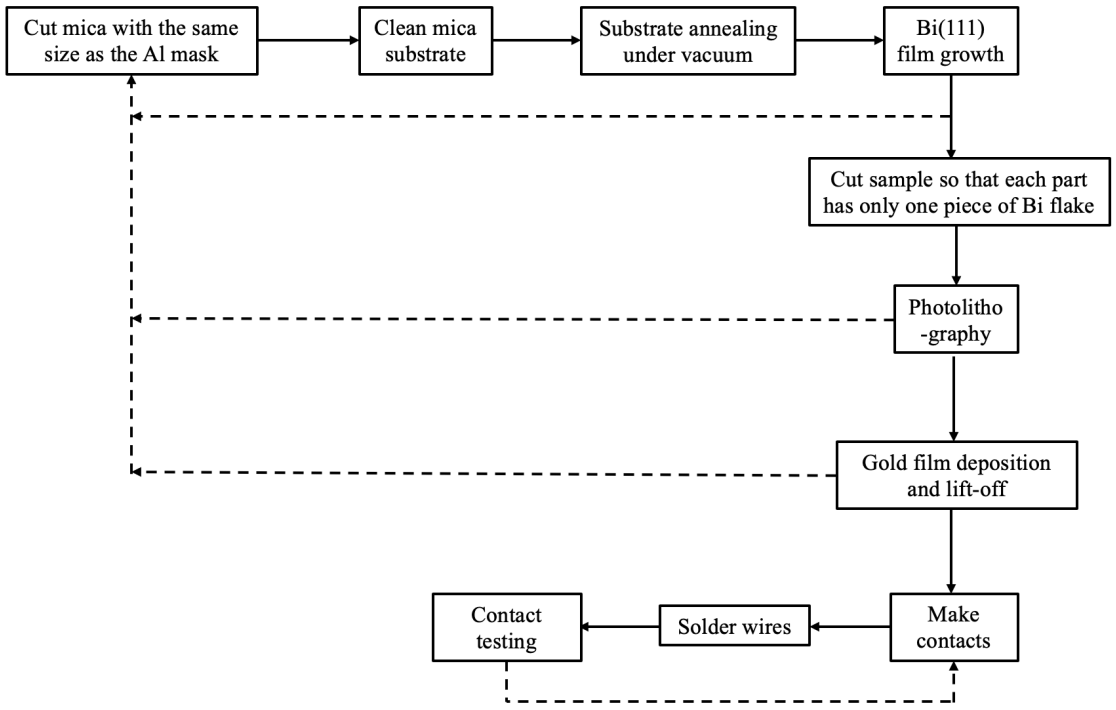

Figure 2.8: Diagram for growing Bi(111) film flakes on mica substrate. The dashed backward arrow means redo it due to some failure.

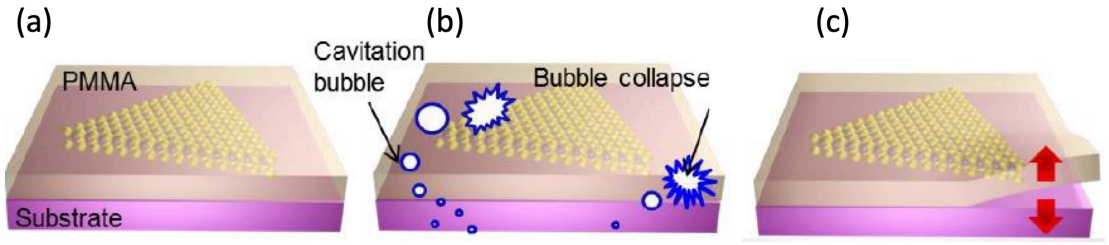

Figure 2.9: PMMA transfer method to transfer Bi(111) film flake from mica to the targeted substrate SiO_2. (a) Spin-coating PMMA on Bi(111) grown on mica. (b) Ultrasonic agitation for 2 minutes in water. (c) Peeling off Bi(111) film flake from mica with water assistance. Sourced from [11] with permission.

substrate: SiO_2. A big problem is that with the use of water and acetone, the Bi(111) film surface wrinkles a lot. PDMS transfer is a dry transfer without water (Figure 2.11). We put PDMS on the surface of Bi(111) on mica, and then peel off PDMS, with some flakes of Bi(111) adhering to it, and then press on the target substrate, and we peel the PDMS off. Figure 2.10(a) shows the SEM images of a PMMA-transferred Bi film flake on SiO_2, with irregular flake shapes and many cracks on the surface. We also checked the surface quality by enlarging the magnification (Figure 2.10(b)), which shows a fairly flat surface with large triangular terraces. However, neither the PMMA transfer nor PDMS stamp methods can control the size of the film flake, and neither method can peel off pure Bi(111). There are always some layers of mica peeled off together with Bi(111), making the flake very thick. It is hard to adhere such Bi flakes to a SiO_2 substrate, leading to a difficulty in making contacts (the Bi film flake can be easily blown off from SiO_2 when lift-off for the Au contact is performed). The shadowmask growth method was developed to solve the problems. Firstly, we don't need to transfer the film flakes to other substrates; secondly the Bi flake can adhere to mica very well and won't be blown off.

To summarize, the growth of high quality Bi(111) films has been carried out on three different substrates by us. When growing Bi(111) films on InSb(111)B 2×2 and Si(111) 7×7 reconstructed surfaces, the very small lattice mismatch between Bi(111) and InSb(111)B and the magic lattice mismatch between Bi(111) and Si(111) 7×7 surface make high quality growth possible under Stranski-Krastanov (S-K) growth mode, in which the interface between the Bi(111) film and the substrate shows dangling bonds. The growth of Bi(111) film on mica is van der Waals epitaxial growth (vdWE). Mica has a completely terminated surface without dangling bonds, and the vdW gap between Bi(111) and mica is so weak that Bi can grow unstrained. This chapter mainly discussed the growth method of Bi(111) on the three different substrates, and we summarize all the growth parameters in Table 2.1. We will compare the surface quality and transport results of Bi(111) films or film flakes on the three substrates in chapter 3.

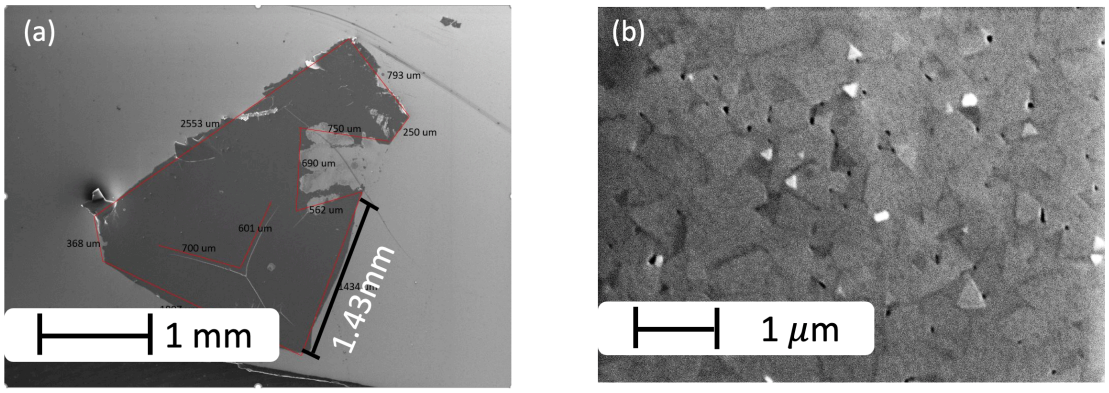

Figure 2.10: (a) SEM image of a 40 nm thick Bi(111) film flake, grown on mica, fabricated by the PMMA transfer. (b) Magnified SEM image of the same flake showing a fairly flat surface with apparent large triangular terraces.

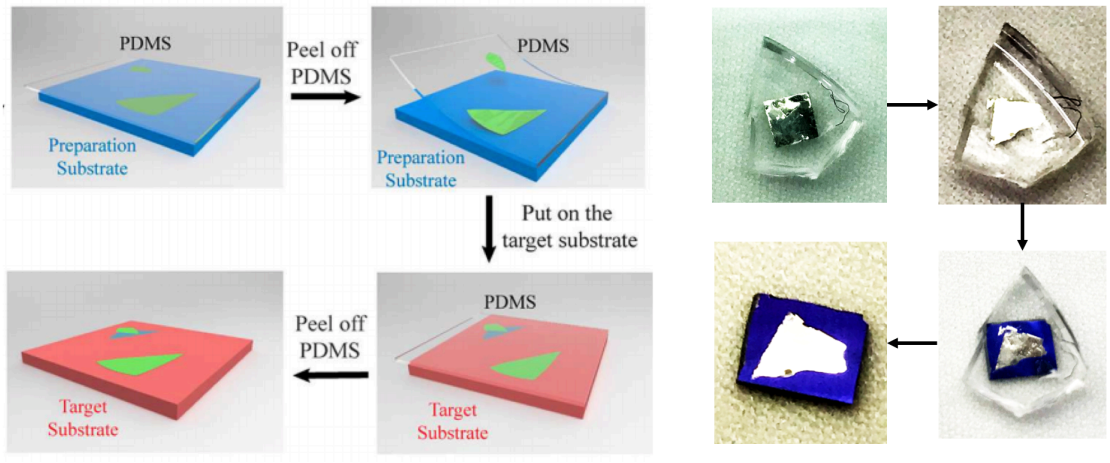

Figure 2.11: Procedures of PDMS stamping method to transfer a film to another substrate. Sourced from [12] with permission. The right figure shows the transfer of a Bi(111) film flake from mica to SiO_2.

Table 2.1: Parameters used for Bi growth (cfr Chapter 3)

substrate	**InSb(111)B**	**Si(111)**	**Mica**
Substrate preparation	Anneal at 300 °C for 5 hours	Anneal at 600 °C for 3 hours Flash heat at 1200 °C for 2 min Cool down at the rate < 2 °C/s	Freshly cleaved by a tape Anneal at 250 °C for 24 hours
Pressure	$\sim 10^{-8}$ Torr	$\sim 10^{-8}$ Torr	$\sim 10^{-8}$ Torr
Growth rate	0.5 Å/s	0.35 BL_{111}/min $\sim$ 1.4 Å/min	0.35 BL_{111}/min $\sim$ 1.4 Å/min
Growth temperature	20 nm at 100 °C 55 nm at 250 °C	Room temperature	Room temperature
Post-growth annealing	250 °C for 2 hours	80 - 100 °C for 1 hour	90 - 100 °C for 1 hour
Film thickness	75 nm	10 - 40 nm	10 - 40 nm

2.4 Photolithography

In order to make contacts on the Bi(111) film flakes on mica, the photolithography technique is used to pattern Au film contacts since the flake is too small to directly make four Wood's metal contacts on it. The mask used here has a six-leg pattern as shown in Figure 2.7 (b), which is the portion unshadowed with FeO so that the photoresist (ma P 1210) can be exposed and removed by a UV light source from the surface, enabling the deposition of Au film on it. The photolithography mask aligner used here (see Figure 2.12) contains a UV light source capable of emitting 365 nm ultra-violet light, a movable stage, and a microscope (Karl Suss, model MJB3). The procedure of Au film patterning is described as follow.

First, the mica substrate with Bi film flakes is glued to a glass cover slip. Then the photoresist is spin-coated on the sample by a spin-coater, Specialty Coating Systems model P-6000. When mounting the sample on the spin-coater, we center the glass slide exactly so that the chuck's grooves are completely covered, otherwise the photoresist may flow onto the stage. Minimal amount of photoresist is dripped onto the sample (only covering the sample), since again too much resist may enter the vacuum line or flow down the stem. We start the coater, with parameters set to 3000 rpm for 30 s. Then we softbake the sample in a 90 °C oven for exactly 30 minutes in order to cure the photoresist.

Subsequently the sample is placed on the movable stage of the photolithography machine, covered by the six-leg shadow mask. A UV exposure time of 3 s is used. Prior to exposure the lamp should be warmed up for minimum of 30 minutes, and two blank exposures (no sample and no mask) of 15 s each should be performed for autocalibration of the system. The exposed device then is developed by a developer solution of Microchem 303A 1 : 8 (1 part 303A, 8 parts H_2O), developed for 30 s, and immediately rinsed in DI water for at least 40 s. After blow drying the sample, we check the surface photoresist pattern under an optical microscope to make sure the pattern is sharp and clear.

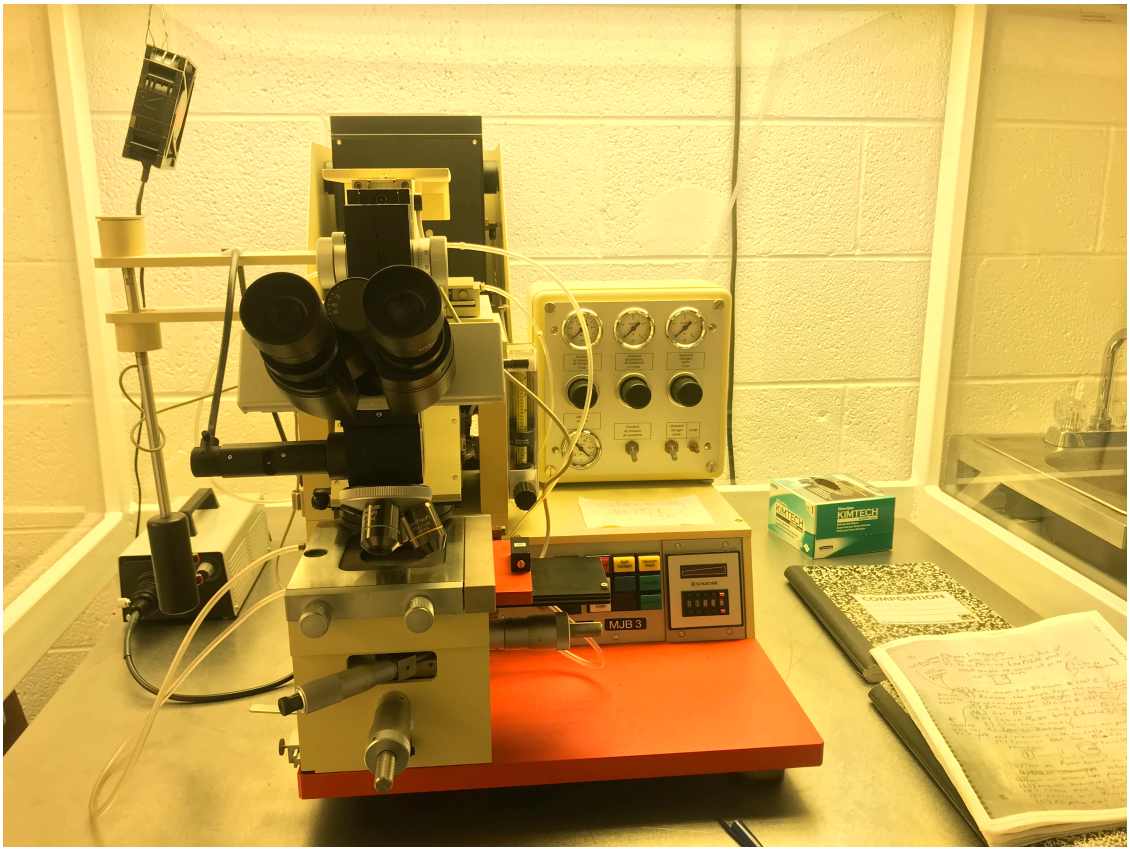

Figure 2.12: Photolithographic mask aligner used to pattern the Au film contacts.

Figure 2.13: The thermal evaporator used to deposit Au film Ohmic contacts.

Au film Ohmic contacts are deposited by evaporation on the sample in a thermal evaporator (Edwards Auto 306, with turbomolecular pump), which is depicted in Figure 2.13. The evaporation procedure requires several steps. To pump the chamber to a low pressure level (7-8 $\times$ 10^{-7} Torr) efficiently, liquid N_2 is poured into a cold trap while pumping. 10 nm thick Cr and 70 nm thick Au are deposited onto the sample surface in sequence, where the film thickness is monitored by a quartz crystal balance. To remove the photoresist and the unnecessary part of the Au film, the sample is soaked into acetone for about 30 minutes, using a syringe to wash the Au film out if necessary. Then we soak the sample in fresh acetone for about 30 minutes to make sure all the photoresist has been removed from the sample surface. Then we clean the sample with isopropanol and blow dry the sample with dry N_2. Now the sample looks exactly like in Figure 2.7 (b), and is ready for wiring. Instead of applying contacts on the corners of the film, we put Wood's metal solder on the thicker end of each Au leg.

2.5 Low-temperature Techniques

Transport measurements are performed from room temperature to about 4.0 K or 0.4 K, which can be achieved in two types of cryostats.

When samples only need to be cooled down to 4.0 K, a ^{4}He cryogen-free system is used. As depicted in Figure 2.14 (a), the sample chamber (in purple) is filled ^{4}He at low pressure as thermal exchange gas, and a pulse-tube cryofridge (Cryomech PT405) cools the sample down. It takes about 3-4 hours to cool the sample down to $\sim$ 4.0 K. The magnet, water-cooled, is driven by a large DC current, capable of magnetic fields to 1.375 T. The temperature can be controlled and varied from 4.0 K to $\sim$ 30 K by using a resistive heater on the device probe, controlled by a temperature controller (Lake Shore).

When 0.4 K is needed, the ^{3}He System is used, as shown in Figure 2.15. We first cool down the system with liquid nitrogen since it is much cheaper than liquid helium. Liquid helium is filled in the dewar after all the liquid nitrogen is removed (otherwise the liquid nitrogen will solidify). The sample can be cooled down to about 1.1 K with ^{4}He. To cool the system down to 0.4 K, ^{3}He is liquefied into the sample chamber and then evaporated to its original reservoir. The whole process takes long and requires experience. The superconducting magnet is capable of magnetic fields up to 9 T and its control has higher magnetic field resolution than the setup for the cryogen-free system, achieving more accurate measurements.

Usually we apply the magnetic field perpendicularly to the film plane. However sometimes an in-plane magnetic field is required during measurements. This can be achieved by simply rotating the sample holder probe by 90 ° at room temperature before the cooling procedure is initiated. But in vacuum (usual for cryogenic measurements), we are unable to rotate the sample probe by this method. In that case, a rotating sample probe is used, where the sample holder can be controlled by a linear manipulator activated by a rotary motion (see Figure 2.16(a)). Typically the manipulator is capable of rotating the sample holder by 360 °. Figure 2.16(b) shows part of the probe, with the header holding the sample rotated by the manipulator to achieve in-plane magnetic field. Using the rotating sample probe both an in-plane and perpendicular magnetic field can be achieved.

When performing measurements, the electrical connections between the sample and the instruments are achieved by using a switch box, as shown in Figure 2.17. There are more than 14 switches/pins on the box panel, corresponding to the pins on the DIP header. The temperature of the sample is monitored and controlled by temperature controller (either model LS311 or LS370AC). The DC current used for the generation of carrier spin polarization by the Edelstein effect on the sample surface (see Chapter 4) is supplied by a Yokogawa GS200 DC voltage/current source. The AC current to measure the magnetotransport properties is supplied by a voltage-controlled current source (SRS model C5580), where the AC voltage originates from a lock-in amplifier, which is also used for measuring the resulting AC sample voltages. The lock-in amplifiers we use include SRS model SR830, EG&G model 116, and SRS models SR124 and SR2124. The magnet power supplies are a Power Ten current

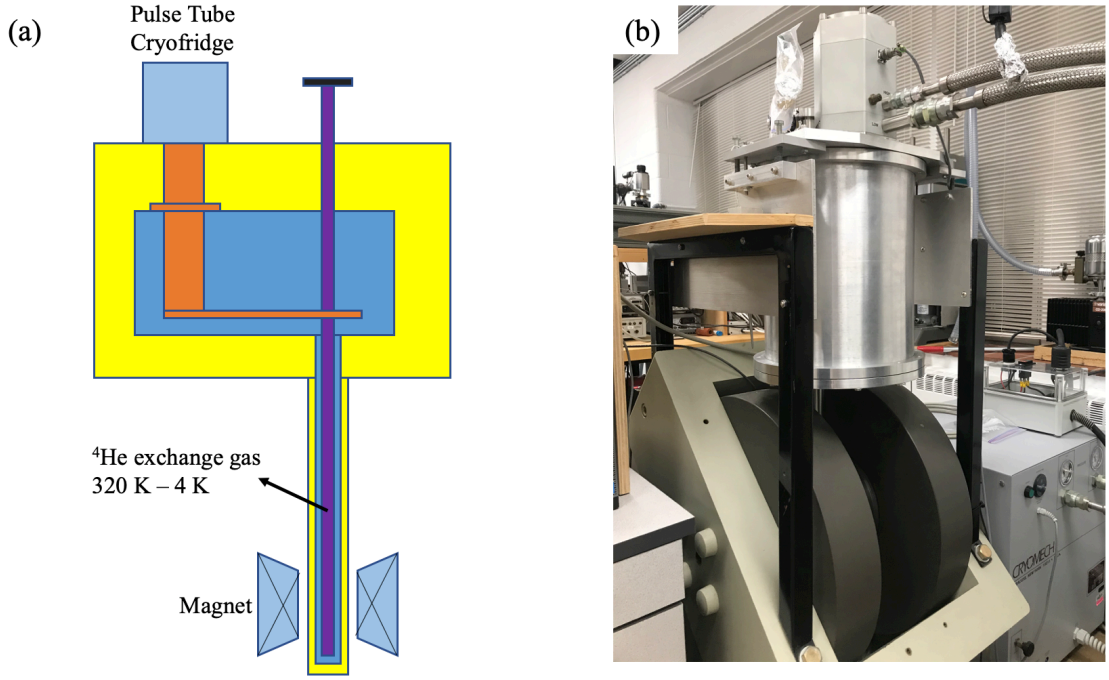

Figure 2.14: (a) Schematics of the cryogen-free pulse tube cryofridge system, which can lower the temperature to $\sim$ 4 K. (b) The corresponding cryostat equipment.

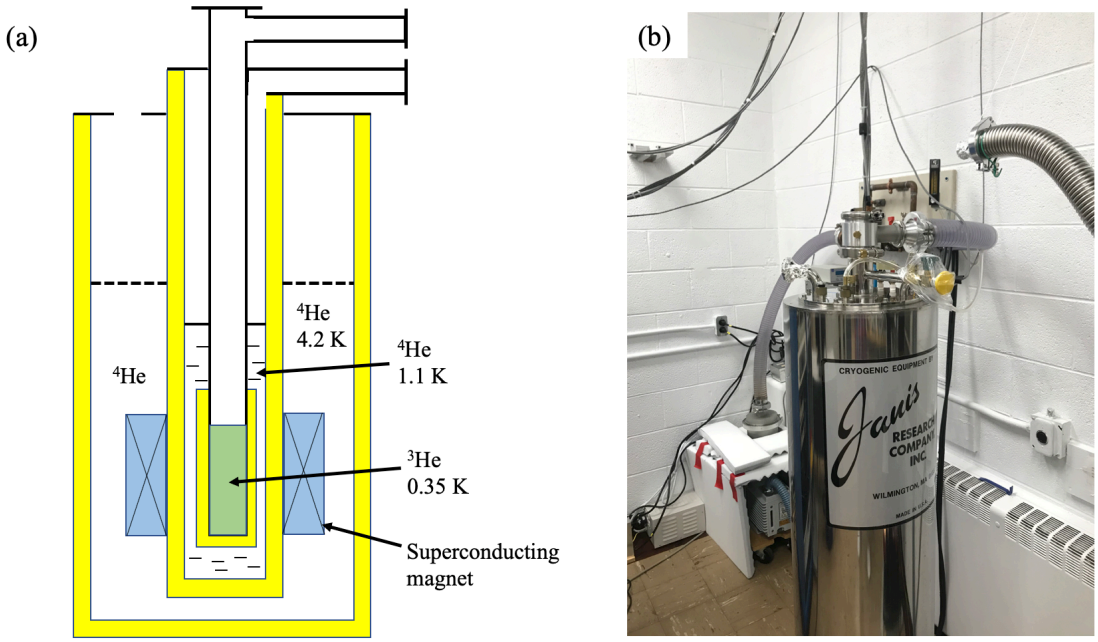

Figure 2.15: (a) Schematics of the ^{3}He cryogenic system, which can lower the temperature to $\sim$ 0.35 K. (b) The corresponding cryostat equipment.

Figure 2.16: (a) The linear manipulator that controls the rotation of the sample holder to achieve various magnetic field orientations relative to the film plane.(b) The Janis tilting probe sample holder, by tilting which both parallel and perpendicular magnetic field can be achieved.

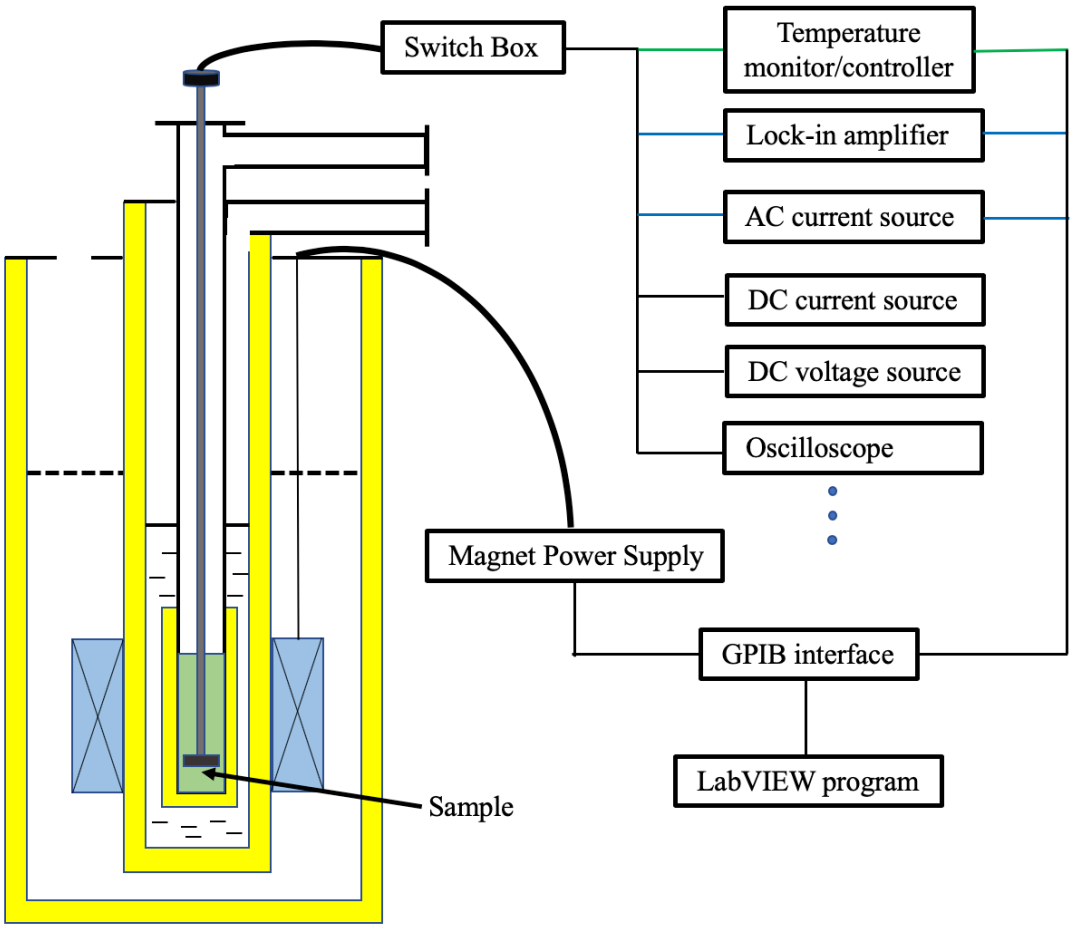

Figure 2.17: Schematic of the measurement setups.

source (model P63C-60166) with a GMW current reversal switch (model 5970-160), a Kepco current source (model BOP 20-20D), and a Cryomagnetics CS-4 superconducting magnet supply. Some instruments mentioned above are connected via a general purpose interface bus (GPIB), through an optical isolator which isolates the noise from the computer. The data are acquired by LabViEW programs in the computer.

Chapter 3

Bi(111) Film Characterization

The growth of high quality Bi(111) films is challenging. As discussed in the last chapter, we explored and developed methods for growth of high quality Bi(111) films on various substrates. In our experiments, Bi has been deposited onto InSb(111)B, Si(111), and mica substrates, and growth methods were discussed in detail in Chapter 2. To evaluate the qualities of the Bi(111) films, we first use scanning electron microscopy (SEM) and atomic force microscopy (AFM) to obtain the structural and morphological characteristics on the film surface. We prefer a film surface with apparent layered structure, large grain sizes, and fewer defects. Many factors can contribute to good surface quality: type of substrate, proper substrate preparation, growth temperature, growth rate, post-growth annealing process, film thickness, etc. We have given the optimal range of those parameters in Chapter 2. In this chapter, we will present the SEM and AFM micrographs of the films with varying substrates, varying annealing processes, and varying film thicknesses, to illustrate why those parameters were considered optimal.

Apart from the morphological analyses, in this chapter we will also show quantum transport and magnetotransport properties of the Bi(111) films. We will show why InSb(111)B is not suitable for growing Bi(111) films though the lattice mismatch between InSb(111)B and Bi(111) is the lowest among the substrates used in this dissertation. We grew 10, 20, 40, 60 and 1000 nm thick Bi(111) films on Si(111) and/or mica, and the electronic transport properties will be be discussed and compared. We will show the dependence of the carrier densities and mobilities (extracted from the magnetoresistance curves and Hall measurements) on the temperature, film thickness and the substrate. Weak antilocalization of thin Bi(111) films ($\leq$ 40 nm) on mica and Si(111) is analyzed from the low temperature magnetoresistance. ILP (theory of Iordanskii, Lyanda-Geller, and Pikus) [14] fitting is used to obtain the quantum phase decoherence time τ_ϕ and the SOI spin decoherence time τ_{SO}, and their dependence on the film thickness and the substrate will also be illustrated.

3.1 Bi(111) Film Surface Morphology

The SEM (LEO/Zeiss EVO 40) and AFM (Bruker) used here are depicted in Figure 3.1. For the SEM the electron current should be set to about 35-40 pA, and a fine focus is required while zooming in. Both experience and patience are needed. The AFM is easier to use,

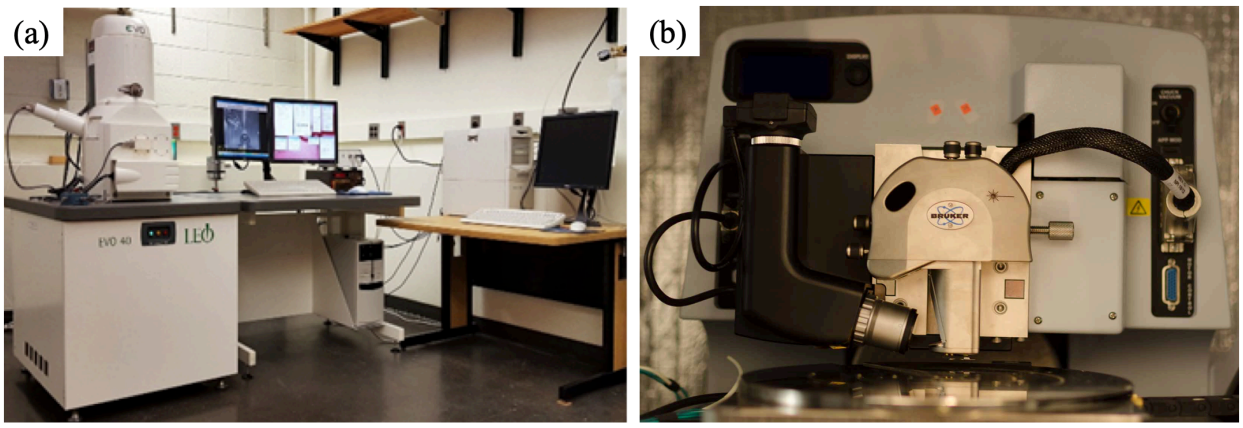

Figure 3.1: (a) The scanning electron microscope and electron-beam lithography system. (b) The atomic force microscope in Virginia Tech's Micro and Nano Fabrication Laboratory (cleanroom).

keeping in mind that the sample should be very clean and mounted on a clean glass slide, since the vacuum process needs a large sample area. The surface morphological analyses is performed by using ancillary software provided in the computer. AFM measurements usually use two parameters to evaluate the roughness of a surface: Ra and Rq, where Ra is the roughness average, and Rq the root mean square of roughness. The definitions of Ra and Rq are shown below:

$$Ra = \frac{1}{l_r}\int_0^{l_r} |z(x)|dx, Rq = \sqrt{\frac{1}{l_r}\int_0^{l_r} z^2(x)dx}. \tag{3.1}$$

The smaller either Ra and/or Rq are, the less rough the surface is.

Bi(111) films were deposited on three different substrates, InSb(111)B, Si(111), and mica, and the surface morphology of the film surface was analyzed by using SEM and AFM. In our research, SEM is used to obtain micrographs for all the substrates, while AFM is only used for the latter two. There is also only one thickness of Bi(111) film grown on InSb(111)B, namely 75 nm, while 10 nm, 20 nm, 40 nm, and 60 nm Bi(111) films were grown on the other two substrates. Figures 3.2(a,b,c) shows the SEM micrographs of Bi(111) films on the three substrates (75 nm Bi for InSb(111)B, 40 nm Bi for Si(111), 40 nm Bi for mica). It is apparent that for Bi grown on InSb(111)B and Si(111), there are more defects on the surface compared to Bi grown on mica, appearing as a larger number of white bright grains higher than the surrounding territory. The fewer defects on the Bi(111) on mica are also much smaller, showing large-scale uniformity. Figure 2.10(b) depicts another example of 40 nm Bi(111) on mica, with both representative areas showing a large grain size up to ~ 1 μm. The grains exhibit characteristic triangular or hexagonal growth patterns (highlighted in red contours in Figure 3.2(c)), corroborating the rhombohedral crystal structure of Bi thin films with the trigonal axis (C_3 axis in Figure 1.1) perpendicular to the plane. However, in

Figures 3.2(a,b) such patterns cannot be found in the SEM micrographs of the Bi(111) films grown on InSb(111)B or Si(111).

While the SEM micrograph of the 40 nm Bi(111) film on Si(111) does not show any triangular or hexagonal terraces, we can find them on the AFM micrograph of 10 nm Bi(111) on Si(111). Figures 3.3(a-b) present the SEM and AFM micrographs of such a film. Compared to Figure 3.2(b) of 40 nm Bi(111) on Si(111), we observe that the thinner 10 nm Bi(111) on Si(111) has fewer and smaller defects and has higher uniformity. Moreover, the AFM micrograph (Figure 3.3 (b)) of the 10 nm Bi(111) on Si(111) shows the triangular growth patterns, which clearly indicate a layered step surface. We performed a step analysis on these triangular terraces, which gives an average step height 0.39 ± 0.02 nm, corresponding to 1.0 BL_{111}, the Bi(111) bilayer height, as shown in Figure 2.1(b). Over the 1 μm $\times$ 1 μm area, AFM measurements reveal Ra = 0.911 nm and Rq = 1.60 nm. Compared to the film thickness of 10 nm, the roughness measurements imply that 10 nm Bi(111) on Si(111) features a flat high-quality surface. In comparison, returning to 40 nm Bi(111) on Si(111) (Figure 3.2(b)), the AFM micrograph of 40 nm Bi(111) on Si(111) shown in Figure 3.3(d)) does not reveal a layered surface. The roughness analysis of 40 nm Bi(111) on Si(111), shows over the 1 μm $\times$ 1 μm area values Ra = 7.43 nm and Rq = 9.34 nm, substantially larger than Ra and Rq for 10 nm Bi(111) on Si(111).

Different from Si(111), the Bi(111) films on mica show the triangular terraces for all growth thicknesses attempted. Figure 3.4(a) depicts the AFM micrograph of the 40 nm Bi film on mica, which clearly indicates a layered step surface with triangular terraces. The layered surface also appears on 10 nm Bi films on mica (Figure 3.4(c)). In Figure 3.4 (b), step analysis in the red rectangular area of Figure 3.4(a) reveals that the step height between adjacent terraces 0.391 ± 0.015 nm, corresponding to 1.0 BL_{111}. Over the 1 μm $\times$ 1 μm representative area, AFM measurements on the 40 nm Bi on mica reveal that Ra = 1.25 nm and Rq = 1.53 nm. Compared to the larger Ra and Rq for 40 nm Bi on Si(111), the roughness measurement implies that the Bi film features a flatter and higher-quality surface on mica than on Si(111). The AFM micrograph of the 10 nm Bi on mica (Figure 3.4(c)) was obtained on a 2 μm $\times$ 2 μm region. In Figure 3.4(d), step analysis in the red rectangular area of Figure 3.4(c) reveals an average step height 0.382 ± 0.031 nm, very close to 1.0 BL_{111}. Over the 2 μm $\times$ 2 μm representative area, AFM measurements on the 10 nm Bi on mica reveal that Ra = 1.84 nm and Rq = 2.35 nm. The roughness Ra = 0.911 nm and Rq = 1.60 nm of the 10 nm Bi on Si(111) is apparently smaller. But for 10 nm Bi on Si(111) Ra and Rq were extracted over a 1 μm $\times$ 1 μm area, compared to 2 μm $\times$ 2 μm for 10 nm Bi on mica, we therefore conclude that there is no apparent difference between the roughness of the 10 nm Bi on Si(111) and on 10 nm Bi on mica. However, by comparing Figure 3.4 (c) with Figure 3.3 (b), one can find that the triangular terrace (grain size) on the 10 nm Bi on mica is much larger than on Si(111).

We conclude that morphologically high-quality Bi film growth can hence be realized on mica over the full range of thicknesses attempted, but can only be achieved on Si(111) if the thickness does not exceed $\sim$ 10 nm.

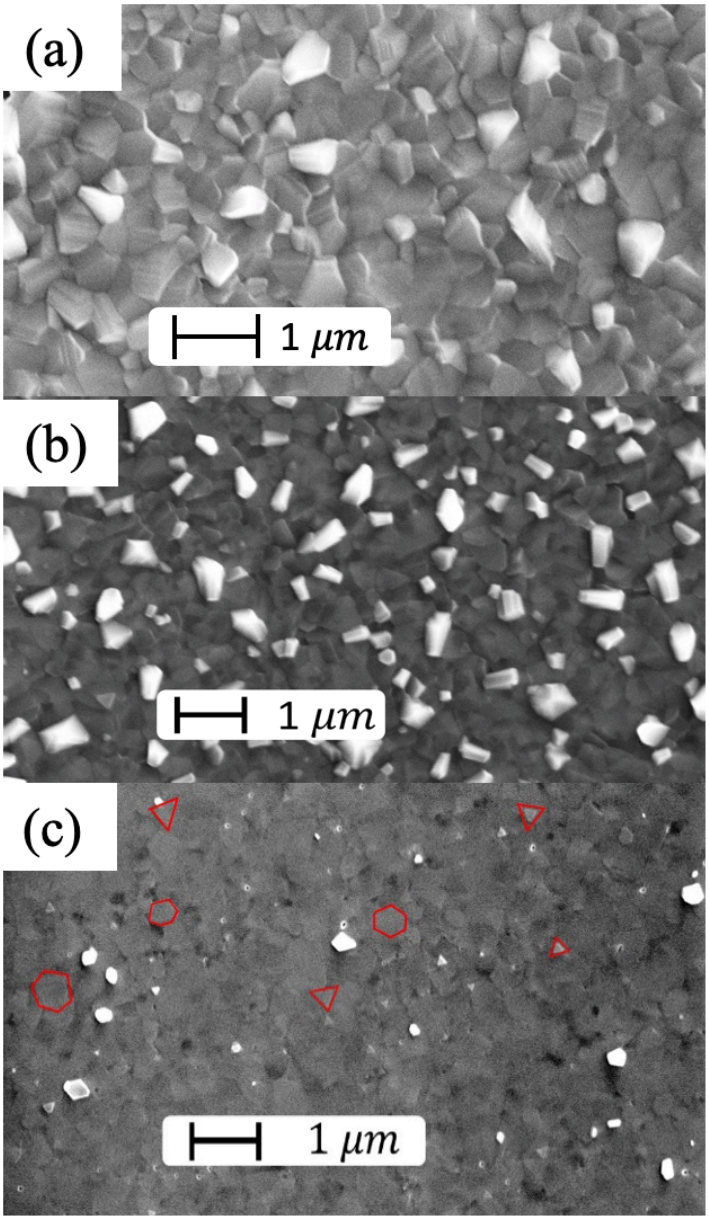

Figure 3.2: The SEM micrographs of Bi(111) films on the three substrates.

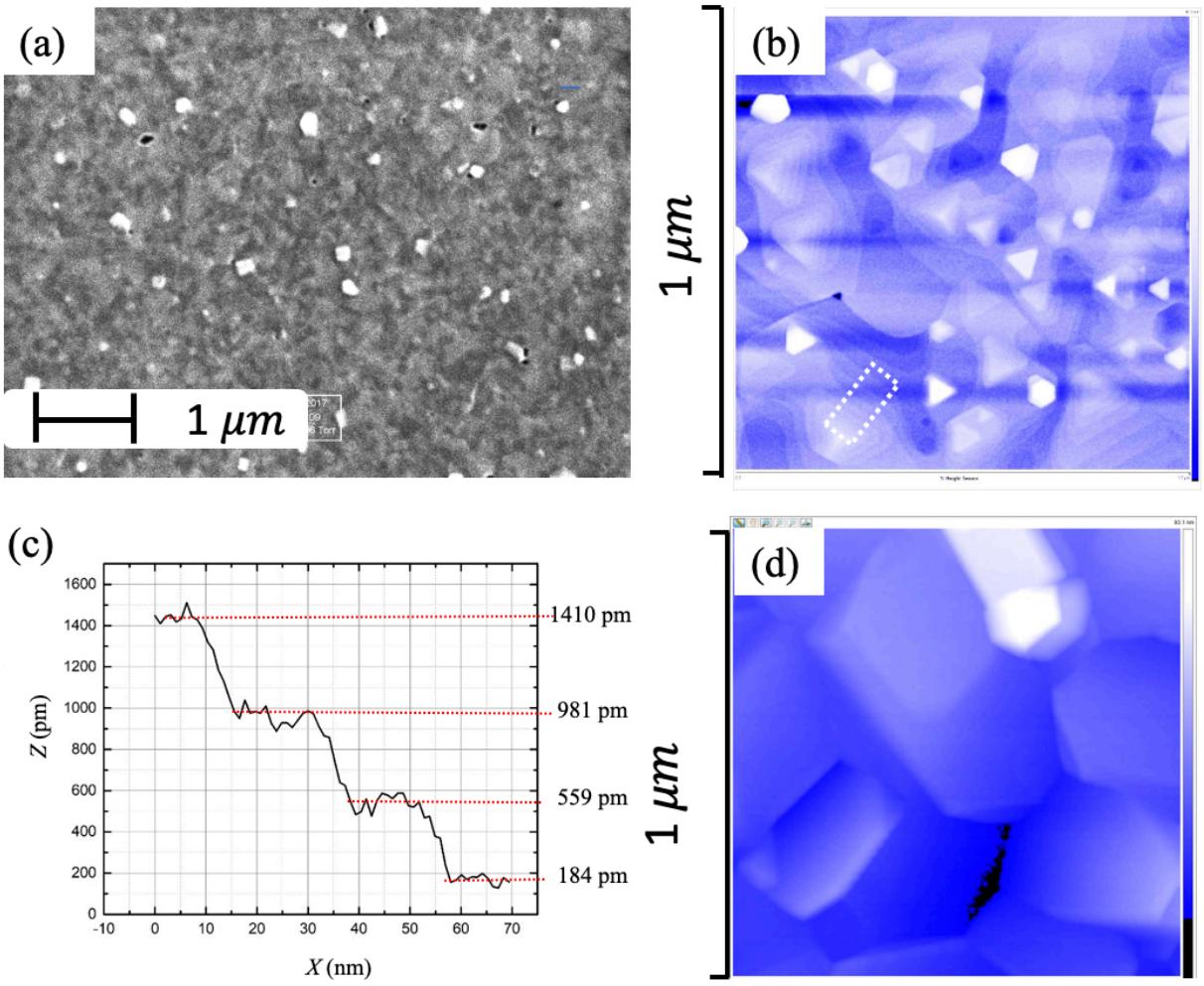

Figure 3.3: (a) SEM micrograph of a 10 nm Bi(111) film on Si(111). (b) AFM micrograph of the same Bi(111) film. (c) Height profile (Z) vs horizontal distance (X) obtained from the AFM micrograph in (b) along the length direction of the white rectangular box in (b). (d) AFM micrograph of a 40 nm Bi(111) film on Si(111); no layered surface is found.

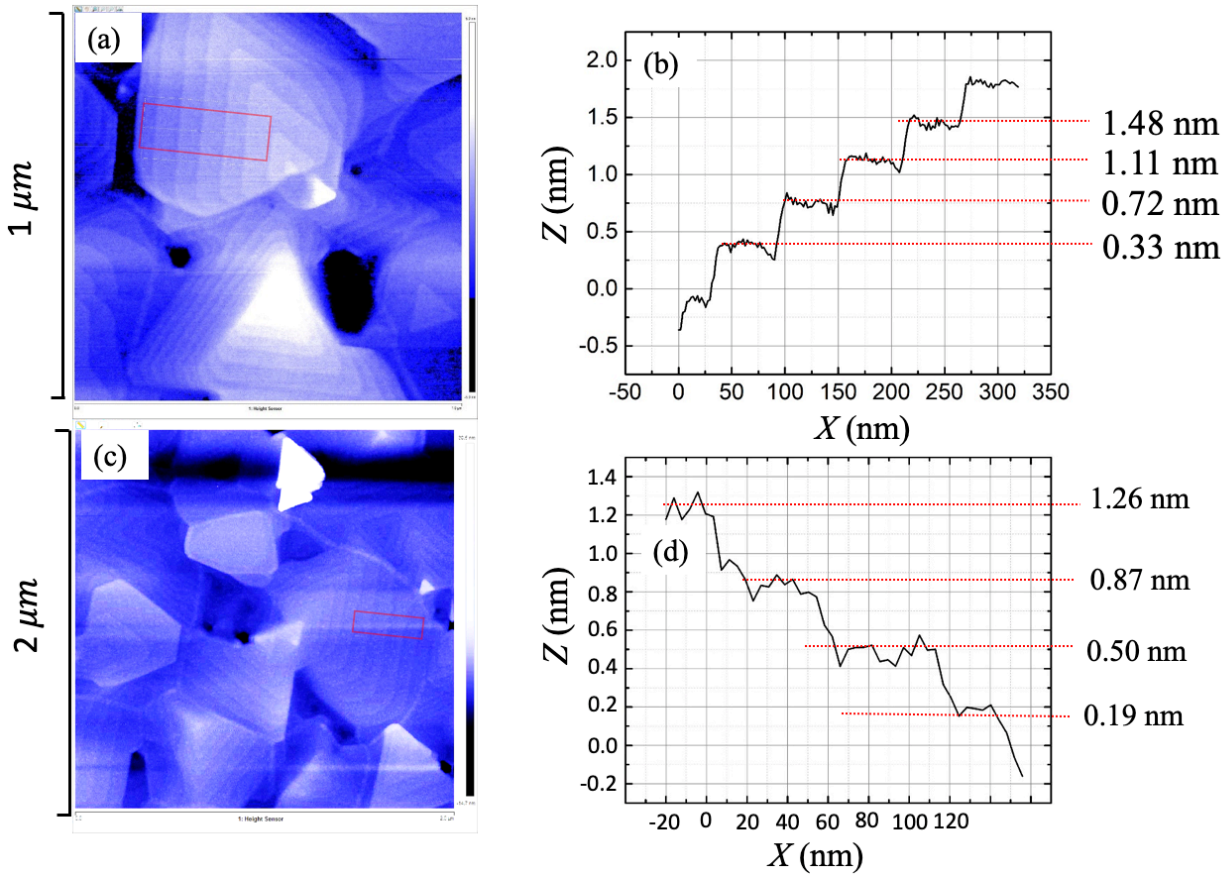

Figure 3.4: (a) AFM micrograph of a 1 μm $\times$ 1 μm area of a 40 nm Bi(111) film on mica, illustrating layered growth and triangular growth patterns. (b) Height profile (Z) vs horizontal distance (X) obtained from the AFM micrograph in (a) along the length direction of the red rectangular box in (a). (c) AFM micrograph of a 2 μm $\times$ 2 μm area of a 10 nm Bi(111) film on mica. (d) Height profile (Z) vs horizontal distance (X) obtained from the AFM micrograph in (b) along the length direction of the red rectangular box in (b).

3.2 Effect of Annealing on Bi(111) Film Surface Morphology

To reduce the roughness of the Bi(111) film surfaces and increase their grain size, annealing processes have been carried out as described in several papers. Nagao [8] et al. not only provided the growth details of Bi(111) film on Si(111) 7×7 reconstructed surface, but also investigated the thermodynamic stability of the films by annealing them to temperatures up to 150 °C. The mentioned annealing processes kept below 150 °C smoothed the film and enlarged the grain size to μm scales. Yaginuma [94] et al. also pointed out that annealing at about 410 K (137 °C) of Bi(111) films grown on Si(111) increases the average terrace width from 18.5 nm to 60 nm, which otherwise under 350 K remained at 18.5 nm. Pang Fei [96] et al. moderately annealed their Bi films grown on Si(111) at around 400 K to achieve flat single crystal surface. Yao [115] et al. grew Bi(111) bilayers at the temperature of 420 K in a two-step growth method on Si(111). F. Y. Yang [116] electrodeposited Bi films of thicknesses of 1-10 μm on thin Au underlayers on Si(100) and annealed the initially polycrystalline films at 268 °C for 6 hours in Ar to achieve single-crystal films.

In short, post-growth annealing processes can improve the Bi(111) surface quality by reducing film roughness as well as enlarging the grain size. Based on the findings, we also carried out annealing processes after the growth of Bi(111) films on the three different substrates, by using two annealing methods. The first method consists of annealing the film under UHV in the growth chamber after the growth procedure, and this method was used predominantly (e.g. for all Bi on mica films). The second method consists of using a laboratory annealing system (as shown in Figure 3.5, as used for Ohmic contact annealing) featuring a glass chamber flushed with forming gas, H_2 / N_2, after taking the sample out of the growth chamber. The first method is preferred, but precludes observing the surface changes under optical microscopy between the unannealed and annealed surfaces, which can be achieved by the second method. The second method also allows annealing the Ohmic contacts to decrease contact resistance and improve Ohmic characteristics. We detail the first method in Appendix A, while annealing by the second method is described below.

1. We gently lift the glass chamber, load the Bi(111) sample in the center of the white heater stage, reposition the glass chamber, and secure the bolts providing the gasket seal.

2. We displace and flush the air out of the chamber by opening the gas valve to the forming gas, using a pressure of about 4 psi. We flush for about 5 minutes.

3. We activate the heater, setting the temperature to a target value. Once the target temperature is reached, we keep at target temperature for 5 minutes.

4. The heater is then turned off. We wait for the temperature to reach below 80 °C prior to removing the sample, to prevent excessive oxidation.

We optimized the annealing processes as shown in Table 2.1, resulting in processes whereby

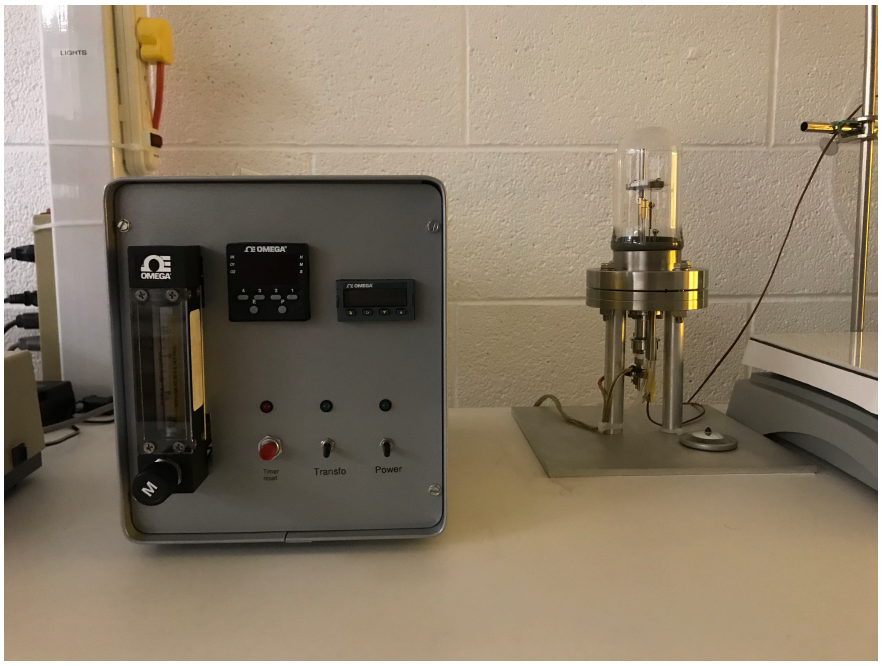

Figure 3.5: Laboratory Ohmic contact annealing system, featuring a glass annealing chamber allowing observation.

we anneal the Bi films on InSb(111)B at 250 °C for 2 hours, we anneal the Bi films on Si(111) at 80 - 100 °C for 1 hour, and we anneal the Bi film on mica at 90 - 100 °C for 1 hour. Some Bi films on InSb(111)B and some Bi films on Si(111) were annealed in the laboratory annealing system (second method), while all Bi on mica films were annealed in the UHV growth chamber (first method). All results in Figure 3.6 were obtained by annealing in the UHV growth chamber (first method).

Figure 3.6 shows how over-annealing and under-annealing affect the surface morphology. Figure 3.6(a) presents the SEM micrograph of a 75 nm Bi(111) film on InSb(111)B, which was over-annealed at 260 °C for 2 hours. The high temperature led to over-annealing and broke the surface into irregular clusters. Figure 3.6(b) shows the SEM micrograph of a 10 nm Bi(111) film on Si(111), over-annealed at 135 °C for about 1 hour. Here the Bi(111) film was broken and congregated as circular islands with diameter about 0.5 - 1.0 μm, which were hexagonally arranged. Figure 3.6(c) depicts the AFM micrograph of a 10 nm Bi(111) film on mica, which was over-annealed at 110 °C for 1 hour, whose surface still shows triangular terraces but without apparent layered structure. The surface morphology separated into many discontinuous islands. Figure 3.6(d) presents the AFM micrograph of a 10 nm Bi(111) film on Si(111), under-annealed at 80 °C for only 30 minutes. Figure 3.6 can be compared to Figure 3.3(b) representing annealing at about 100 °C for 1 hour. The under-annealed sample represented in Figure 3.6(d) has larger roughness and does not exhibit a regular stepped surface with triangular terraces.

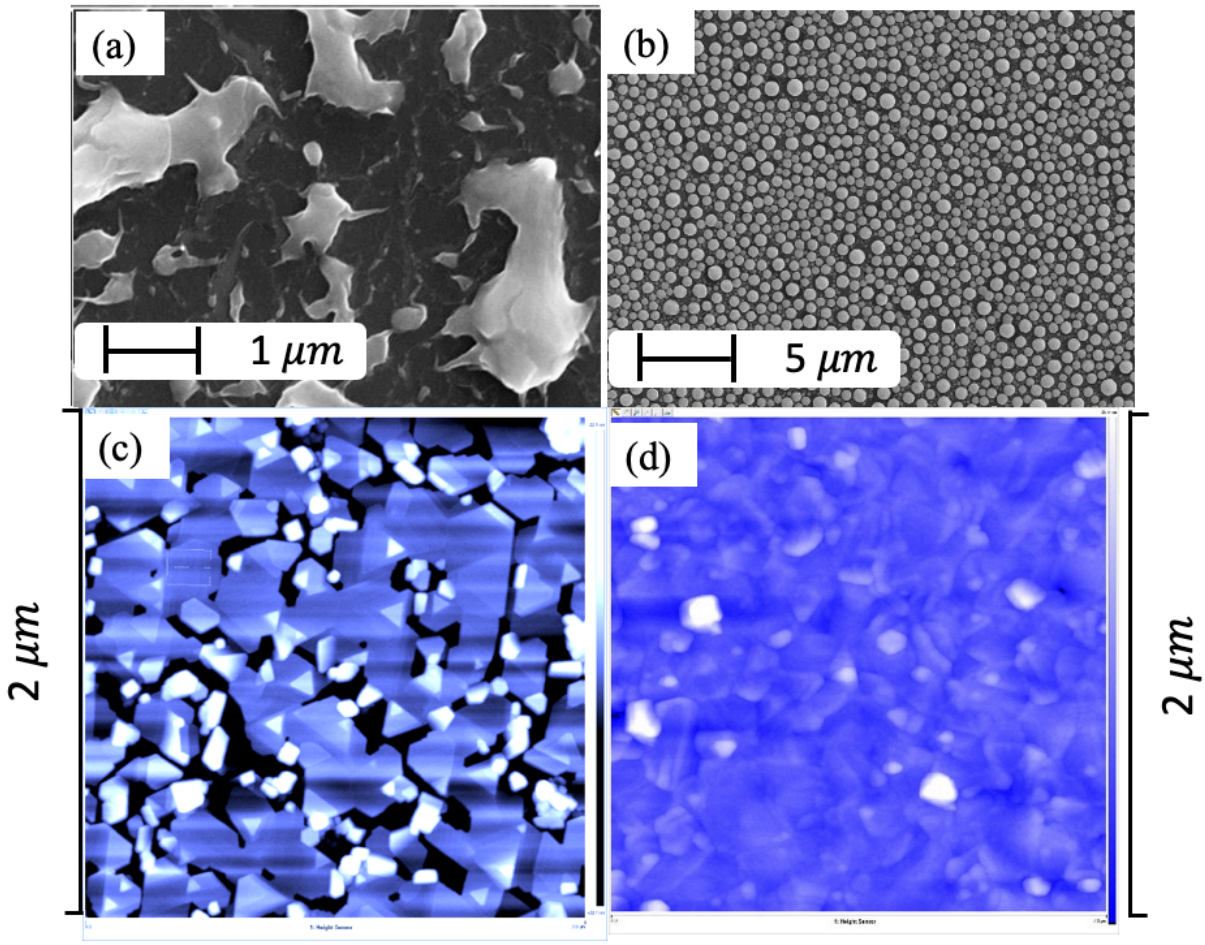

Figure 3.6: (a) SEM micrograph of a 75 nm Bi(111) film on InSb(111)B, annealed at 260 °C for 2 hours, under UHV in the growth chamber after growth (first method). (b) SEM micrograph of a 10 nm Bi(111) film on Si(111), annealed at 135 °C for 1 hour, under UHV in the growth chamber after growth (first method). (c) AFM micrograph of a 2 μm $\times$ 2 μm area of a 10 nm Bi(111) film on mica, annealed at 110 °C for 1 hour, under UHV in the growth chamber after growth (first method). (d) AFM micrograph of a 2 μm $\times$ 2 μm area of a 10 nm Bi(111) film on Si(111), annealed at 80 °C for 30 minutes, under UHV in the growth chamber after growth (first method).

3.3 Bi(111) films Transport Characterization

In addition to exploring optimal methods to obtain high quality Bi(111) films, researchers also carried out quantum transport and magnetotransport measurements to extract the electrical properties, and quantum phase coherence and spin coherence properties of Bi(111) films. A few examples from an incomplete list are mentioned here. M. Rudolph and J. J. Heremans [43] presented a two-step growth of Bi(111) film on SiO_2 and calculated the carrier densities and mobilities on the film at room temperature and 4.2 K through transport measurements by applying a varying magnetic field perpendicular to the sample surface, and further extracted the phase coherence length and spin orbit coherence length by fitting the weak antilocalization (WAL) curves. Similar research was also executed on lithographically defined Bi wires [5]. Pang Fei [96] et al. measured the sheet resistance of Bi(111) films from 5 nm to 30 nm thickness grown on Si(111) over the temperature range 300 K to 2 K, experimentally clarifying the origin of the predicted semimetal-to-semiconductor transition vs temperature in Bi(111) films (also observed by us and about which more below). They also analyzed the magnetotransport properties of the Bi(111) films by applying either a perpendicular magnetic field or an in-plane one [117], however without much quantification analysis. Xiao [97] et al. also studied and quantified the semimetal-to-semiconductor transition of Bi(111) films where the film thickness is comparable to the bulk Bi Fermi wavelength. They measured the temperature dependence of Bi(111) film conductivity on Bi(111) films ranging from 4 nm to 540 nm thickness MBE-grown on BaF_2 substrate. Zhu [98] et al. obtained quantum transport measurements on Bi(111) films grown on Si(111) under varying temperatures and film thicknesses, and emphasized the difference in the conductivity of Bi(111) films grown on different substrates (Si(111) or BaF_2). F. Y. Yang [116] studied the magnetoresistance in electrodeposited Bi films of thicknesses of 1-10 μm.

Growth of Bi(111) on mica is novel, and high-quality Bi(111) films on mica show superior surface morphology to Bi(111) on Si(111), at least when the thickness of the latter exceeds 10 nm. Hence, here we compare the electronic properties and coherence properties between Bi films with varying thicknesses (10, 20, 40, and 60 nm) on mica and Si(111) at room temperature (about 296 K) and 4.1 K. Beforehand, we will first discuss the transport properties of Bi(111) films on InSb(111)B, to explain why InSb(111)B was not preferred.

3.3.1 Electronic Properties of Bi(111) on InSb(111)B

The growth method of Bi(111) films on InSb(111)B has been discussed in Chapter 2. A 75 nm Bi(111) film was grown on InSb(111)B 2 × 2 reconstructed surface and annealed at 250 °C for 2 hours. Four Ohmic contacts were applied to the Bi film surface and we obtained magnetotransport properties in a van der Pauw configuration (cfr Figure 1.5 (a)) over room temperature to 4.1 K. As comparison, the same measurement was carried out on a pure reconstructed InSb(111)B substrate surface without Bi. We depict the results in Figure 3.7,

where Figure 3.7(a) presents the sheet resistance $R_\square$ vs temperature for the InSb(111)B surface, while (b) presents the Bi(111) film on InSb(111)B. $R_\square$ is calculated from the van der Paur results R_a and R_b. We first extract $R_\square$ from R_a and R_b either at $T = 4.1$ K or $T = 296$ K, since we can only measure only one of R_a or R_b when cooling down. We then calculate $R_\square = \frac{\pi(R_a+R_b)}{ln2}$ (with a prefactor ~ 1 if $R_a \approx R_b$). Supposing the trace over variable T was obtained as $R_a(T)$, we then calculate the ratio $\frac{R_\square}{R_a}$ at either $T = 4.1$ K or $T = 296$ K, a ratio which we assume stays substantially constant when $T \neq 4.1$ K or $T \neq 296$ K. We then multiply $R_a(T)$ by the ratio to obtain $R_\square(T)$ in $\Omega/\square$.

Bulk Bi in pure crystalline form is a semimetal, with low and equal electron and hole densities, namely both $\sim 3 \times 10^{23}$ m^{-3} for $T \lesssim 30$ K while higher but still equal electron and hole densities are observed at higher T, namely both up to $\sim 24.5 \times 10^{23}$ m^{-3} at $T = 300$ K [45]. Yet we mentioned that over variable T the transport in Bi(111) *thin films* can be expected to exhibit a semimetal-to-semiconductor transition at a transition temperature T_C. Semiconducting behavior is then observed for $T > T_C$ ($R_\square(T)$ increasing as T decreases) while semimetal (i.e. metallic) behavior is observed for $T < T_C$ ($R_\square(T)$ decreasing as T decreases).

However, Figure 3.7(b) depicting $R_\square(T)$ vs T for 75 nm Bi(111) on InSb(111)B shows a more complex behavior: semiconducting behavior reappears again for $T < 50$ K. We attribute this behavior to dominant contributions to transport from the InSb(111)B substrate, as a comparison to transport in a InSb(111)B substrate will justify. As shown in Figure 3.7 (a), there is no significant difference between the traces of $R_\square$ vs T for InSb(111)B and Bi(111) on InSb(111)B. We conclude that for Bi(111) on InSb(111)B substrate, the InSb(111)B substrate contributes dominantly to the transport results down to low T, presumably due to the considerable substrate thickness ($\gg 75$ nm). Extracting transport properties of solely Bi(111) by treating the InSb(111)B and Bi(111) as parallel conducting channels could not be achieved due to the high similarity between the two traces. Henceforth we therefore focus on Bi(111) on Si(111) and mica.

3.3.2 The Semimetal-to-Semiconductor Transition in Bi Films

As described in the preceding section, bulk Bi in pure crystalline form is a semimetal, with low and equal electron and hole densities. We add that the electron and hole densities both $\sim 3 \times 10^{23}$ m^{-3} at $T \lesssim 30$ K [45] will yield a Fermi wavevector $k_F \approx 2.1 \times 10^8$ m^{-1} and a Fermi wavelength $\lambda_F \approx 30$ nm. The unusually long λ_F due to the low carrier density gives rise to quantum confinement effects in thin films of thickness comparable to λ_F. Given the semimetallic character of bulk Bi, the electronic transport properties should show a metallic behavior, with $R_\square(T)$ decreasing as T decreases, and such behavior is indeed observed in pure bulk Bi [45, 118, 119]. Yet transport in Bi(111) *thin films* exhibits a semimetal-to-semiconductor transition at a transition temperature T_C, with semiconducting behavior for $T > T_C$ ($R_\square(T)$ increasing as T decreases) and metallic behavior for $T < T_C$

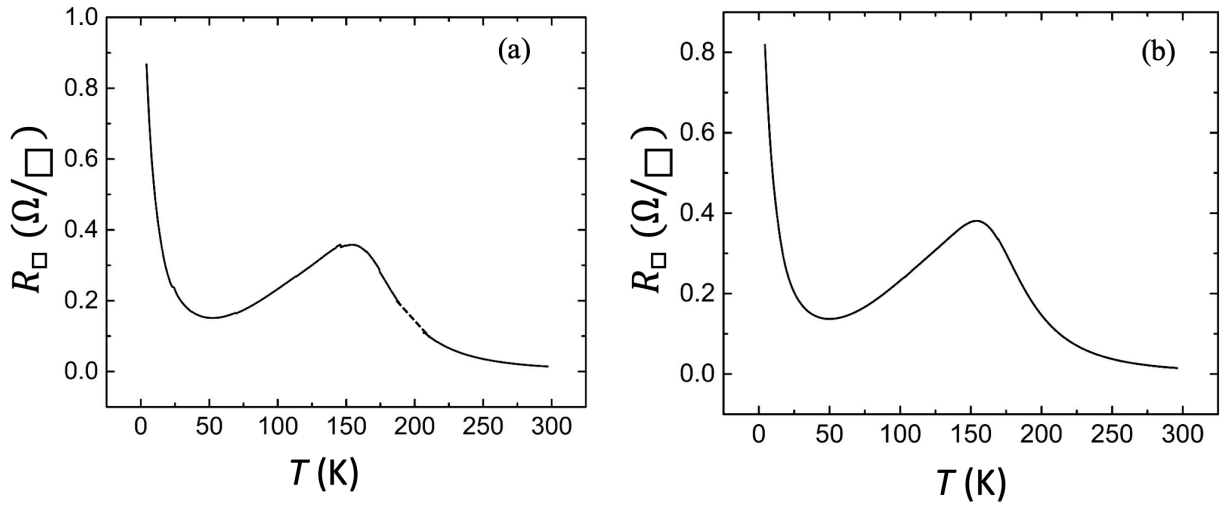

Figure 3.7: The sheet resistance $R_\square$ vs temperature T for InSb(111)B substrate (a), and for a 75 nm Bi(111) film on InSb(111)B (b), from 4.1 K to 296 K.

($R_\square(T)$ decreasing as T decreases). The semiconducting behavior was predicted and ascribed to the quantum confinement effects originating from the long λ_F in thin films of thickness comparable to λ_F (Refs. [1, 46, 47, 97, 98, 117] are among several references describing the transition and its history). Quantum confinement is predicted to open an energy gap $\Delta E \approx 15$ meV to 50 meV, depending on d, T and λ_F, in the interior of a Bi film. In the interior of the film carrier density is then governed by thermal activation across ΔE, yielding the semiconducting behavior of $R_\square(T)$ and resistivity $\rho(T)$ observed for $T > T_C$. We note here that $\rho(T) = dR_\square(T)$. By using the quantum confinement model, Chu [120] et al. theoretically calculated the upper limit of the Bi thickness at which the density of the conduction electrons reduces to zero for $T \to 0$ K. This calculated thickness they find to be 32 nm, and hence according to their calculation the semimetal-to-semiconductor transition can occur for films with $d < 32$ nm. Others predicted and observed that the upper limit of thickness for the transition would lie around $d \approx 23$ nm [47, 121]. Hoffman et al. [47] pointed out that the transition takes place in quite thin bismuth films ($d < 28$ nm), and explained that in such thin Bi films the minority electrons are not observable at low temperature until $T \gtrsim 200$ K, and the electron density would remain low even at higher temperatures. Xiao [97] et al. on the other hand find experimentally that the semimetal-to-semiconductor transition can occur for films with $d < 90$ nm. Thus, while it is clear that a semimetal-to-semiconductor transition is expected in thin Bi films, the exact critical thickness may depend on precise film properties. Xiao [97] et al. express ΔE as $\Delta E = \frac{2b}{d^2}$, where b is a constant and the $\propto 1/d^2$ behavior expresses the quantum confinement effect. The experimental search for the semimetal-to-semiconductor transition has been complicated by the existence of metallic surface states of high conductivity at the surfaces and interfaces of Bi(111) (cfr Chapter 4 and Refs. [1, 97, 98, 117]), the existence of which was not realized early on. Electronic

conduction through Bi(111) thin films hence occurs both through a contribution from the interior of the film and through surface (or interface) states. The competing dependences of the conductivity on d and T orginating from the two contributions leads to a typically complicated behavior of measured conductivity as function of d and T. Xiao [97] et al. expresses the measured longitudinal 3D conductivity $\sigma_{xx} = \frac{1}{dR_\square}$ as a sum of surface (first) and interior (second) terms:

$$\sigma_{xx} = \frac{\sigma_{2D}}{d} + \alpha e^{-\frac{\Delta E}{2kT}} = \frac{1}{d(\rho_0 + sT)} + \alpha e^{-b/d^2 kT} \tag{3.2}$$

where σ_{2D} denotes the metallic surface state 2D conductivity (inverse sheet resistance of the surface states), and α a parameter. Here it is assumed that $\frac{1}{\sigma_{2D}} = \rho_0 + sT$, expressing that the sheet resistance of the surface states originates in a T-independent surface residual sheet resistance ρ_0 and an electron-phonon scattering induced sheet resistance sT, as appropriate for a 2D metal. The surface (first) term in equation 3.2 increases with decreasing d and T, while the interior (second) term decreases with decreasing d and T, leading to complicated behavior of measured σ_{xx} as function of d and T. For lower d (larger ΔE), equation 3.2 can lead to $R_\square(T)$ showing the semimetal-to-semiconductor transition with $R_\square(T)$ increasing as T decreases if $T > T_C$ and $R_\square(T)$ decreasing as T decreases if $T < T_C$, hence showing a maximum in $R_\square(T)$ vs T. Yet for higher d (smaller ΔE), equation 3.2 can lead to $R_\square(T)$ showing an inverse transition with $R_\square(T)$ decreasing as T decreases if $T > T_C$ and $R_\square(T)$ increasing as T decreases if $T < T_C$, hence showing a minimum in $R_\square(T)$ vs T. In the **lemma** appended to this paragraph (below) we show analytically that equation 3.2 can lead to a minimum in $R_\square(T)$ vs T, or equivalently a maximum in $\sigma_{xx}(T)$, because Xiao [97] et al. do not discuss the possibility even though they present data to that effect. As shown in later paragraphs, we have experimentally observed both maxima and minima in $R_\square(T)$ vs T in Bi(111) on Si(111) and/or Bi(111) on mica depending on d, in accordance with equation 3.2. In addition to the evidence provided in Chapter 4, the transport properties presented in this chapter hence corroborate the importance of the Bi(111) surface states.

Lemma, showing analytically that $\sigma_{xx}(T)$ vs T can show a maximum at sufficiently large d: The first derivative $d\sigma_{xx}(T)/dT = \sigma'_{xx}(T) = \frac{\alpha b e^{-b/d^2 kT}}{d^2 kT^2} - \frac{s}{d(\rho_0 + sT)^2}$. Setting the first derivative to 0, we have $e^{-b/d^2 kT} = \frac{sdkT^2}{\alpha b(\rho_0 + sT)^2}$. Inserting this into the second derivative σ''_{xx}, if we obtain $\sigma''_{xx} < 0$ then we find a maximum vs T instead of a minimum. After simplification, we obtain as condition $\frac{b}{d^2 kT^2} + \frac{2}{\frac{\rho_0}{s} + T} - \frac{2}{T} < 0$. If $kT \sim \Delta E = \frac{2b}{d^2}$, then the film will show substantial conductivity [97], while of course at very low T we still obtain $kT \ll \Delta E$. Xiao [97] et al. express $b = \frac{\hbar^2 \pi^2}{2m^*}$, where $m*$ denotes an effective mass, and for $d \approx 10$ nm, they deduce $\Delta E \approx 24$ meV, comparable to kT at 300 K. However, for large d, $\Delta E = \frac{2b}{d^2}$ will be small. Typically $T_C \sim 150$ K, and at $T = 150$ K and for sufficiently large d we readily have $kT > \Delta E = \frac{2b}{d^2}$. Since for $d \approx 10$ nm we have $\Delta E \approx 24$ meV, then for $d = 1$ μm we readily have $kT \gg \Delta E$, which leads to $\frac{b}{d^2} < \frac{kT}{2}$. Returning to $\frac{b}{d^2 kT^2} + \frac{2}{\frac{\rho_0}{s} + T} - \frac{2}{T} < 0$, the first term $\frac{b}{d^2 kT^2} < \frac{1}{2T}$, and

after inserting we obtain the condition $-\frac{2}{4T/3}+\frac{2}{\frac{\rho_0}{s}+T}<0$. Xiao [97] et al. reasonably claim that $\rho_0 > sT$, and hence $\frac{\rho_0}{s} > T$. Then $\frac{\rho_0}{s}+T > 2T > 4T/3$, leading to a validation of the condition $-\frac{2}{4T/3}+\frac{2}{\frac{\rho_0}{s}+T}<0$. In conclusion, when d is sufficiently large and $T \approx T_C$ (in fact in a wide range), we simultaneously can have $\sigma_{xx}^{'}=0$ and $\sigma_{xx}^{''}<0$, denoting a maximum in $\sigma_{xx}(T)$ vs T.

3.3.3 Electronic Properties of Bi(111) on Si(111)

Temperature Dependence

Bi(111) films with thickness ranging from 10 nm to 60 nm were grown on Si(111). The dependence on T of electronic transport properties is measured in the van der Pauw configuration (Figure 1.5 (a)). The measured film sheet resistance $R_{\square}(T)$ and resistivity $\rho(T) = dR_{\square}(T)$ reflect both contributions from the film interior as well as surface states. $R_{\square}$ is calculated as indicated in Section 3.3.1. As shown in Figure 3.8, a transition temperature T_C exists in the 10 nm and 20 nm films, above which the resistivity increases as T decreases and below which the relation is reversed, showing metallic and semiconducting behaviors below and above T_C. The behavior illustrates the expected semimetal-to-semiconductor transition. In our Bi(111) on Si(111), for the 40 nm and 60 nm Bi films the transition is not observed, as shown in Figure 3.8(c-d). A critical thickness 20 nm $< d <$ 40 nm below which the transition can be observed is compatible with the range of critical thicknesses occurring in the literature, which were previously mentioned [1, 46, 47, 97, 98, 117, 120, 121]. We also observe that lower d yields higher T_C. The 20 nm Bi film shows $T_C \approx 25$ K, whereas the 10 nm Bi film shows $T_C \approx 150$ K. The rise in T_C with decreasing d is also observed in the literature [97, 117]. The trend is due to the fact that at lower d the interior of the film contributes less to conduction and the metallic character of the surface states asserts itself more.

Electronic Properties at Room Temperature

We determine the carrier densities and mobilities of Bi(111) films on Si(111) through van der Pauw measurements and Hall measurements. Through van der Pauw measurements, the longitudinal magnetoresistance component $Rxx(B)$ and the Hall resistance component $Rxy(B)$ of the 2x2 magnetoresistance matrix are obtained vs perpendicular magnetic field B. The magnetoresistance $Rxx(B)$ is via $R_{\square}(B)$ normalized to $\rho(B)-\rho(0)$, where $\rho(0)$ represents $\rho(B=0)$. The relative magnetoresistivities $\rho(B)-\rho(0)$ obtained at $T = 296$ K are shown in Figure 3.9(a-b). The use of $\rho(B)-\rho(0)$ allows comparisons at different d, since $\rho(B=0)$ differs substantially. Figure 3.9(a) shows that $\rho(B)$ vs B has a quasi-quadratic dependence on B, which can be explained by multiple carriers conduction, or can be attributed to a geometrical magnetoresistance especially in high-mobility carrier systems [116, 122]. Given the square sample shape, the geometrical influence can here be

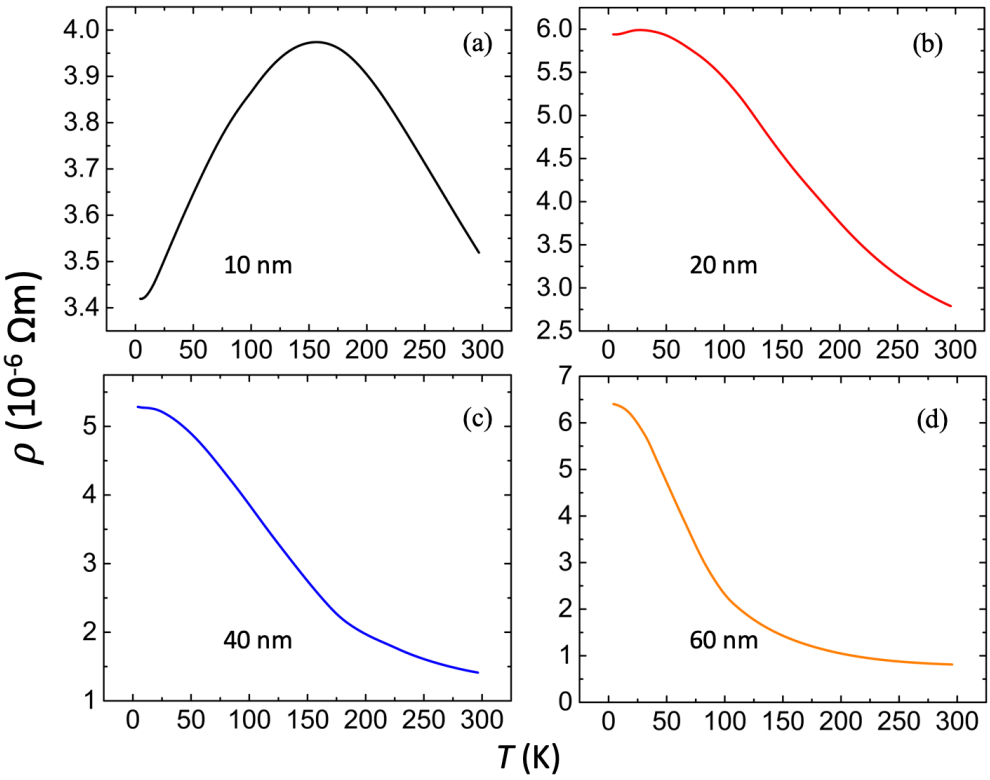

Figure 3.8: The dependence on T of the resistivity of Bi(111) films on Si(111), with Bi thickness 10 nm (a), 20 nm (b), 40 nm (c), and 60 nm (d).

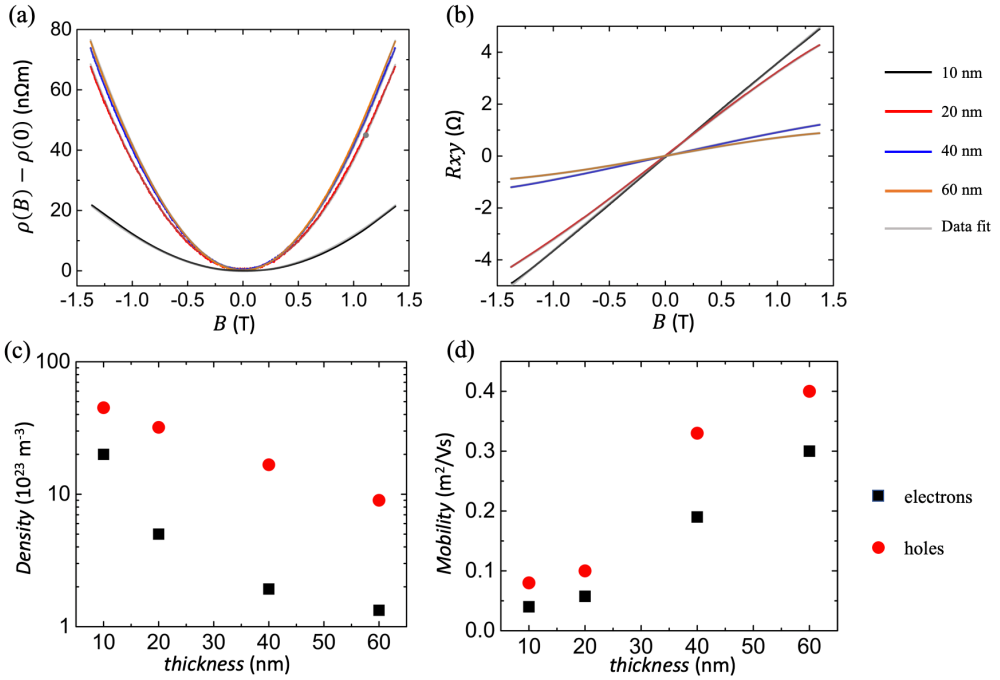

Figure 3.9: The relative magnetoresistivities $\rho(B) - \rho(0)$ (a) and the Hall resistances (b) at $T = 296$ K of Bi(111) on Si(111) for $d = 10$ nm, 20 nm, 40 nm and 60 nm. The transparent gray lines denote fits to the multicarrier transport model. (c) The extracted carrier densities. (d) The extracted carrier mobilities.

neglected. Hence the quadratic dependence is here consistent with multicarrier conduction due to semimetallic Bi harboring both electrons and holes [47, 52]. Figure 3.9(b) shows that $Rxy(B)$ vs B is not linear in B, again an indication of multicarrier conduction. The electron and hole densities and mobilities are determined by fitting the magnetoresistance traces to equation 1.2 and the Hall resistance traces to equation 1.3, with the fits displayed by transparent gray lines in Figure 3.9(a-b). The fits have 4 free parameters, where n is the electron density, p is the hole density, μ is the electron mobility, and ν is the hole mobility. The densities will be expressed as 3D volume densities, but we note they are initially obtained as 2D areal densities which consist of the sum of the areal densities in the surface states and the areal density in the film interior. Hence e.g. $n = \frac{n_{2D}}{d} = \frac{n_{2Dfilm}}{d} + \frac{N_S}{d}$, where n_{2D} denotes the measured total areal density of electrons, n_{2Dfilm} denotes the areal density of electrons in the film interior and $n_{3Dfilm} = \frac{n_{2Dfilm}}{d}$ would denote the 3D bulk density of electrons in the film interior, and N_S denotes the areal density of electrons in the surface states.

Figure 3.9(c-d) presents the extracted carrier densities and mobilities. As d increases, both n and p decrease and both μ and ν increase. We observe that at the measured d, $p > n$, and at $d > 10$ nm, we have $p \approx 10n$. We also observe $\nu > \mu$, with a relation $\nu \approx 2\mu$ for all measured d. We conclude that at room temperature, our Bi(111) on Si(111) exhibits an overall p-type semiconductor character.

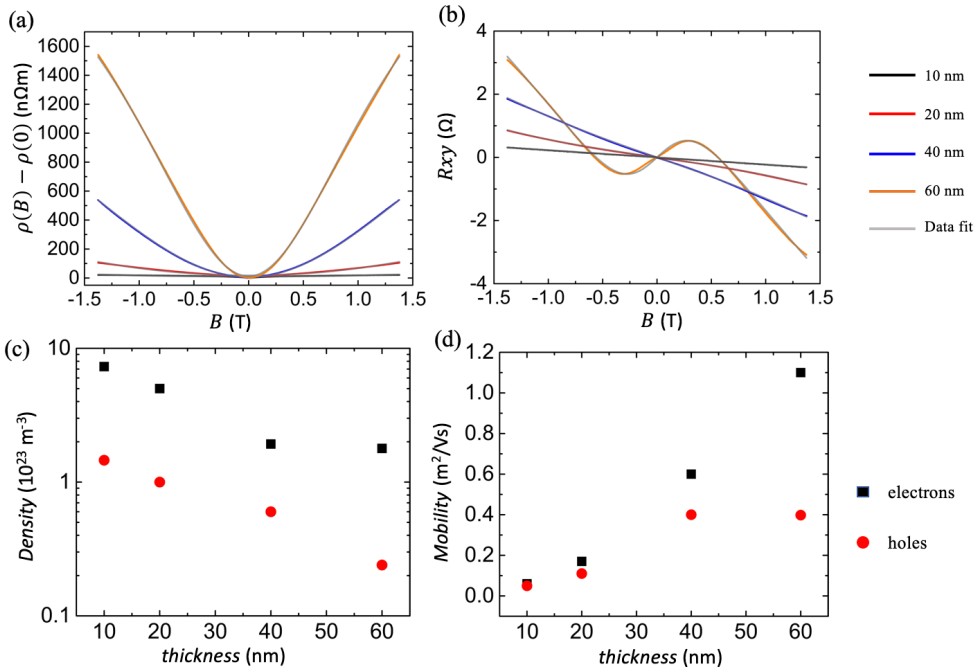

Figure 3.10: The relative magnetoresistivities $\rho(B) - \rho(0)$ (a) and the Hall resistances (b) at $T = 4.1$ K of Bi(111) on Si(111) for $d = 10$ nm, 20 nm, 40 nm and 60 nm. The transparent gray lines denote fits to the multicarrier transport model. (c) The extracted carrier densities. (d) The extracted carrier mobilities.

Electronic Properties at 4.1 K

Figure 3.10(a-b) displays the relative magnetoresistivities $\rho(B)-\rho(0)$ and the Hall resistances at $T = 4.1$ K of Bi(111) on Si(111) for $d = 10$ nm, 20 nm, 40 nm and 60 nm. The transparent gray lines represent fits to the multicarrier transport model using equation 1.2 and 1.3. The extracted carrier densities and mobilities are shown in Figure 3.10(c-d). The two-carrier model is suitable for the Bi(111) with $d \lesssim 60$ nm. M. Rudolph and J. J. Heremans [43] showed that the Bi(111) films with $d \gtrsim 76$ nm apparently harbor more than two carrier types at low T and our fitting results agree with this. As at $T = 296$ K, we observe that both n and p decrease with the increasing d, and μ and ν increase with increasing d. However, at $T = 4.1$ K we observe that consistently $n \approx 5...10p$ at given d, and that $\mu > \nu$ at given d, indicating an overall n-type character. The observation is consistent with the expectation that at $T = 4.1$ K the electron-populated surface states dominate in transport, given their expected higher μ and given that carriers in the film interior will have reduced densities due to the existence of ΔE.

3.3.4 Electrical Properties of Bi(111) Films on Mica

Temperature Dependence

Bi(111) films with thicknesses from 10 nm to 60 nm were also grown on mica, and as for Bi(111) on Si(111), the dependence on T of electronic transport properties is measured in the van der Pauw configuration (Figure 1.5 (a)). Again, the measured film sheet resistance $R_{\square}(T)$ and resistivity $\rho(T)$ contain contributions from the film interior as well as surface states. $R_{\square}$ is calculated as indicated in Section 3.3.1. Figure 3.11 shows that a transition temperature T_C exists in the 10 nm, 20 nm, and 40 nm films, above which the $\rho(T)$ increases as T decreases (semiconducting behavior) and below which the trend is reversed (metallic behavior). As for Bi on Si(111), the behavior illustrates the expected semimetal-to-semiconductor transition. While for Bi(111) on Si(111) the transition is not observed for the 40 nm and 60 nm films, for the Bi(111) on mica, only the thicker 60 nm does not show the transition, as shown in Figure 3.11(d). The critical thickness below which the transition can be observed [1, 46, 47, 97, 98, 117, 120, 121], can hence for Bi(111) on mica be estimated as 40 nm $< d <$ 60 nm, somewhat higher than for Bi(111) on Si(111). We again observe that lower d yields higher T_C, as found for Bi(111) on Si(111) and in the literature [97, 117]. The 40 nm Bi film shows $T_C \approx 20$ K, whereas the 10 nm Bi film shows $T_C \approx 150$ K. The trend is again ascribed to the fact that at lower d the interior of the film contributes less to conduction and the metallic character of the surface states asserts itself more.

Electronic Properties at Room Temperature

We determine the carrier densities and mobilities of Bi(111) films on mica by the same method as on Si(111) (Section 3.3.3). The magnetoresistance $Rxx(B)$ is again normalized to $\rho(B) - \rho(0)$. The relative magnetoresistivities $\rho(B) - \rho(0)$ obtained at $T = 296$ K are shown in Figure 3.12(a-b). Figure 3.12(a) shows that $\rho(B)$ vs B has a quasi-quadratic dependence on B, which as for Bi(111) on Si(111) is attributed to multicarrier conduction. Figure 3.12(b) shows that $Rxy(B)$ vs B is not linear in B, again an indication of multicarrier conduction. The electron and hole densities and mobilities are determined by fitting the magnetoresistance traces to equation 1.2 and the Hall resistance traces to equation 1.3, with the fits displayed by transparent gray lines in Figure 3.9(a-b). The fits again have 4 free parameters (n as the electron density, p as the hole density, μ as the electron mobility, and ν as the hole mobility). The densities are again expressed as 3D volume densities (while initially obtained as 2D areal densities).

Figure 3.12(c-d) presents the extracted carrier densities and mobilities. As d increases, both n and p decrease and both μ and ν increase. We observe that at the measured d, $n > p$, and $n \approx 20p$ for all measured d. We also observe $\mu > \nu$, with a relation $\mu \approx 5\nu$ for all measured d. We conclude that at room temperature, the Bi(111) on mica exhibits an overall n-type semiconductor character.

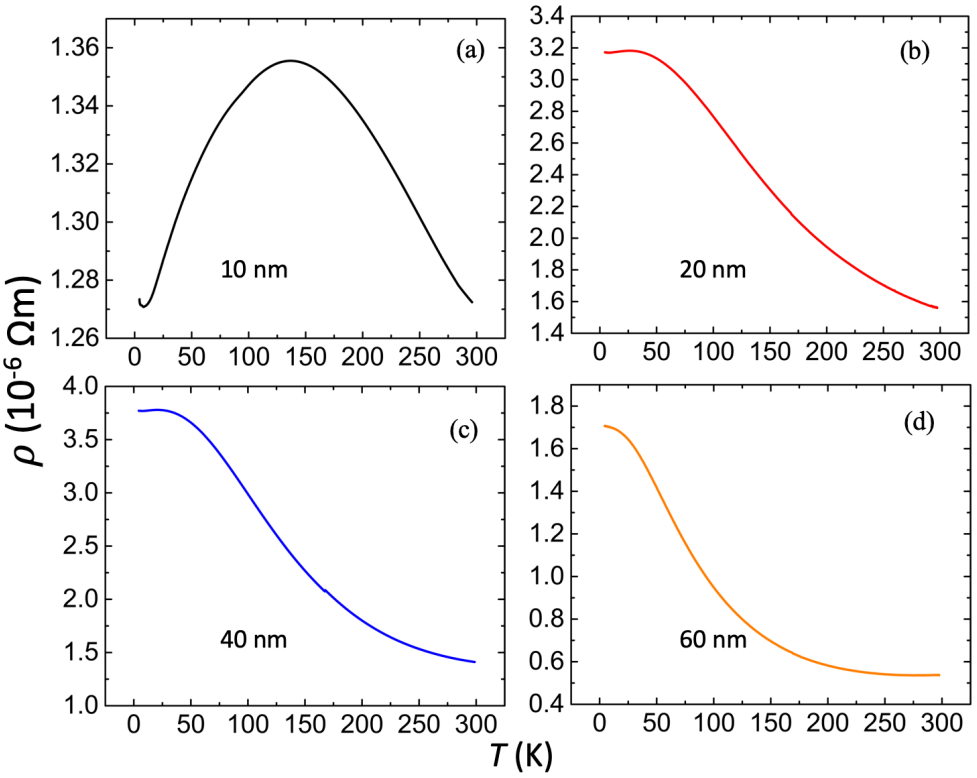

Figure 3.11: The dependence on T of the resistivity of Bi(111) films on mica, with Bi thickness 10 nm (a), 20 nm (b), 40 nm (c), and 60 nm (d).

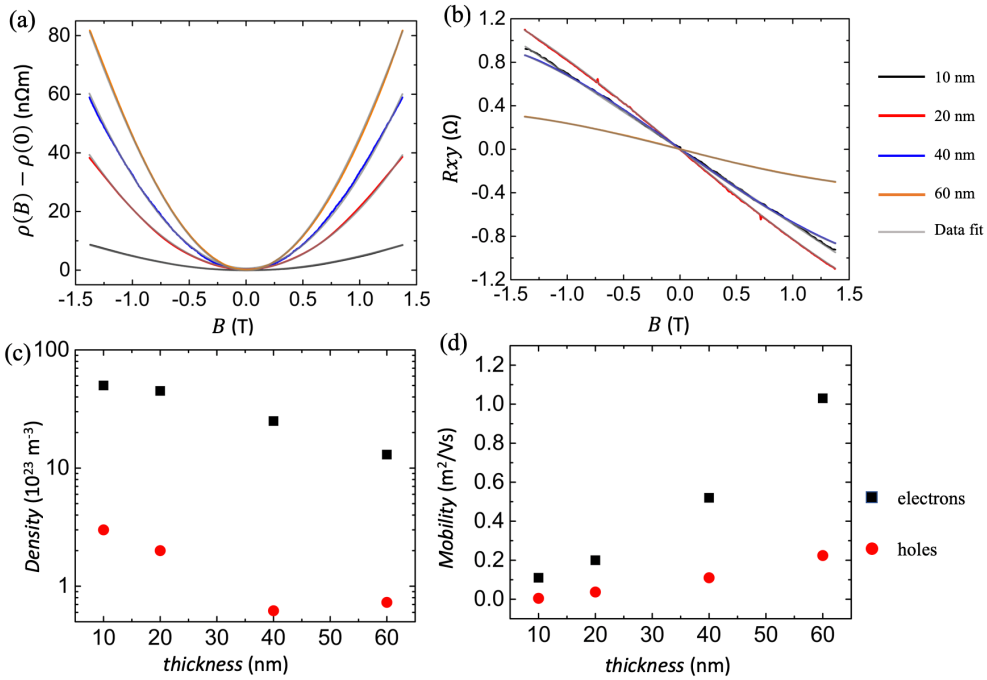

Figure 3.12: The relative magnetoresistivities $\rho(B) - \rho(0)$ (a) and the Hall resistances (b) at $T = 296$ K of Bi(111) on mica for $d = 10$ nm, 20 nm, 40 nm and 60 nm. The transparent gray lines denote fits to the multicarrier transport model. (c) The extracted carrier densities. (d) The extracted carrier mobilities.

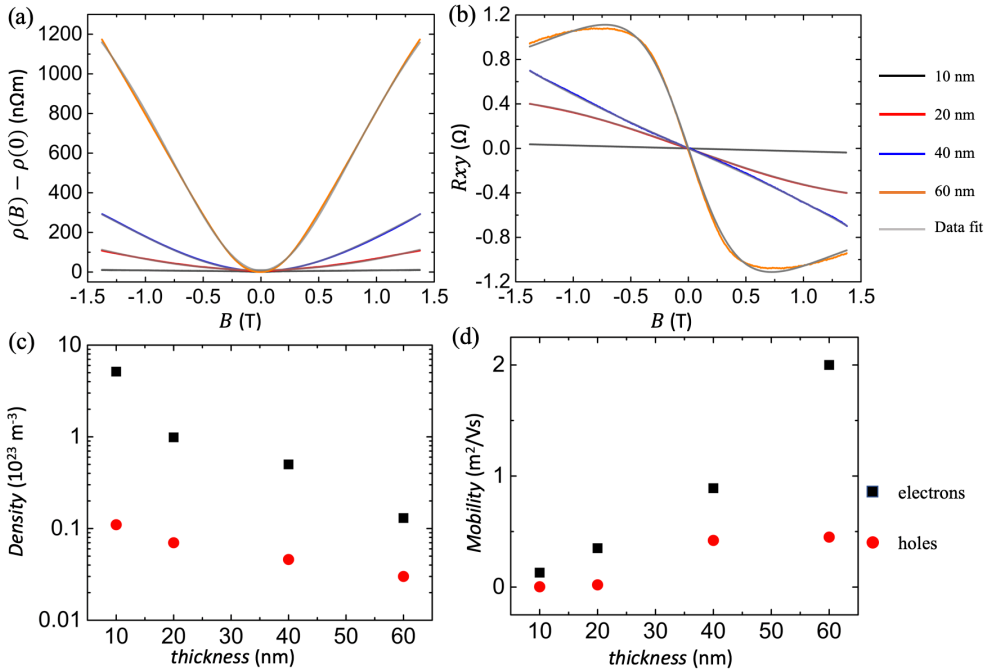

Figure 3.13: The relative magnetoresistivities $\rho(B) - \rho(0)$ (a) and the Hall resistances (b) at $T = 4.1$ K of Bi(111) on mica for $d = 10$ nm, 20 nm, 40 nm and 60 nm. The transparent gray lines denote fits to the multicarrier transport model. (c) The extracted carrier densities. (d) The extracted carrier mobilities.

Electronic Properties at 4.1 K

Figure 3.13(a-b) shows the relative magnetoresistivities $\rho(B) - \rho(0)$ and the Hall resistances at $T = 4.1$ K of Bi(111) on mica for $d = 10$ nm, 20 nm, 40 nm and 60 nm. The transparent gray lines represent fits to the multicarrier transport model using equation 1.2 and 1.3. The extracted carrier densities and mobilities are presented in Figure 3.13(c-d). The two-carrier model is again suitable for the Bi(111) with $d \lesssim 60$ nm. As at $T = 296$ K, we observed that both n and p decrease with the increasing d, and μ and ν increased with increasing d. Yet at $T = 4.1$ K we observe that $n \approx 10...15p$ (higher than for Bi(111) on Si(111)) at given d, and that $\mu > \nu$ at given d, indicating an overall n-type character, more pronounced than for Bi(111) on Si(111). The observation is again consistent with the expectation that at $T = 4.1$ K the electron-populated surface states dominate in transport, given their expected higher μ and given that carriers in the film interior will have reduced densities due to the existence of ΔE.

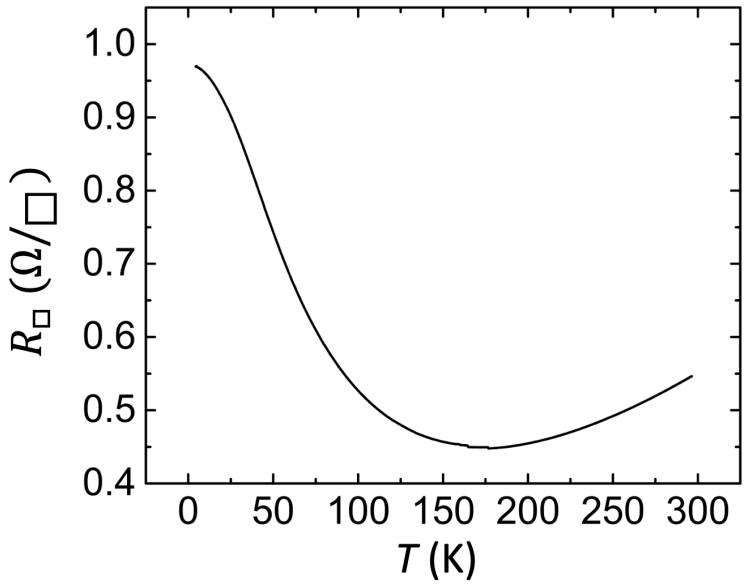

Figure 3.14: The dependence on T of $R_\square(T)$ of the 1 μm thick Bi(111) film on mica.

3.4 Electronic Properties of Thick Bi(111) on Mica

For comparison with the electronic properties of thinner Bi(111) films, we deposited Bi(111) with $d = 1.0$ μm on mica, following the standard deposition protocol but using a higher growth rate. The dependence on T of electronic transport properties is measured in the van der Pauw configuration (Figure 1.5 (a)). The measured $R_\square(T)$ vs T is shown in Figure 3.14. Contrary to the usual semimetal-to-semiconductor transition with $R_\square(T)$ increasing as T decreases if $T > T_C$ and $R_\square(T)$ decreasing as T decreases if $T < T_C$ (showing a maximum in $R_\square(T)$ vs T), in Figure 3.14 the behavior is inverted and $R_\square(T)$ vs T shows a minimum in T. As discussed in Section 3.3.2, equation 3.2 can predict a minimum in $R_\square(T)$ vs T, or equivalently a maximum in $\sigma_{xx}(T)$, for large d. As mentioned in Section 3.3.2, since for $d \approx 10$ nm we have $\Delta E \approx 24$ meV, then for $d = 1$ μm we readily have $kT \gg \Delta E$ for 150 K $< T <$ 300 K, and the conditions for observation of a minimum in $R_\square(T)$ vs T are fulfilled. Figure 3.14 illustrates the complex dependence on T that can result from equation 3.2.

For Bi(111) with $d = 1.0$ μm on mica, using a two-carrier analysis, the electron and hole densities and mobilities are determined by fitting the magnetoresistance traces to equation 1.2 and the Hall resistance traces to equation 1.3. The fits use 4 free parameters, with n the electron density, p the hole density, μ the electron mobility, and ν the hole mobility. The densities are expressed as 3D volume densities. We find at $T = 4.1$ K that $n = 2.82 \times 10^{23}$ m^{-3}, $p = 4.79 \times 10^{23}$ m^{-3}, $\mu = 22.1$ m^2/Vs, $\nu = 10.7$ m^2/Vs. We find at $T = 296$ K that $n = 3.75 \times 10^{24}$ m^{-3}, $p = 4.38 \times 10^{24}$ m^{-3}, $\mu = 0.89$ m^2/Vs, $\nu = 0.60$ m^2/Vs.

These values for the 1.0 μm Bi(111) on mica can be compared to literature values obtained

on high-quality Bi bulk single crystals. The values for n and p we find for 1.0 μm Bi(111) on mica at $T = 4.1$ K are close to compensated ($n \approx p$), and approach the single-crystal literature value $n = p \approx 3 \times 10^{23}$ m^{-3} found at $T \lesssim 30$ K [45, 118, 119]. The values for μ and ν we find for 1.0 μm Bi(111) on mica at $T = 4.1$ K are however about two orders of magnitude lower than bulk single-crystal values ($\mu \approx 800$ ... 2800 m^2/Vs, $\nu \approx 300$ ... 900 m^2/Vs [45, 118, 119]; to account for the very elongated ellipsoidal Fermi surfaces, the literature mobilities we quote are geometrical averages of mobilities along the ellipsoid axes).

The values for n and p we find for 1.0 μm Bi(111) on mica at $T = 296$ K are again close to compensated ($n \approx p$), and approach the room-temperature single-crystal literature value, which averages $n = p \approx 3.1 \times 10^{24}$ m^{-3} [45, 123]. The values for μ and ν we find for 1.0 μm Bi(111) on mica at $T = 296$ K are very similar to bulk single-crystal values ($\mu \approx 0.75$ m^2/Vs, $\nu \approx 0.6$ m^2/Vs [45, 123]; geometrical averages of mobilities along the ellipsoid axes).

3.5 Quantum Coherence Properties of Bi(111) Films

The quantum coherence properties of Bi(111) films can be extracted from the quantum correction to the sheet (2D) conductivity (σ_{2D}) due to weak antilocalization (WAL). As we discussed in Section 1.2, WAL originates from the destructive carrier spin quantum interference due to strong SOI, resulting in a positive MR at low B. In our experiments, the positive MR characteristic of WAL is observed in transport measurements of the 10 nm, 20 nm, and 40 nm thick Bi(111) films at 4.1 K, both on Si(111) and mica. The WAL signal is not resolved in Figure 3.10(a) and Figure 3.13(a) because of the large ranges of B and $\rho(B)$. Therefore, we present the WAL MR traces in Figure 3.15, which shows the negative of $\Delta\sigma_{2D}(B)$ (proportional to MR) at low B in the range of -0.05 T to 0.05 T. We calculated $\Delta\sigma_{2D}(B)$ by using a derived equation $-\Delta\sigma_{2D}(B) \approx \frac{\Delta R_\square(B)}{R_\square(0)^2}$, which is discussed in Section 4.4 in detail. Here $R_\square(0)$ denotes $R_\square(B = 0)$. The comparison between $d = 10$ nm, 20 nm, and 40 nm for Bi(111) films on mica is presented in Figure 3.15(a). The traces for $-\Delta\sigma_{2D}(B)$ shows a widening vs B as ds increases. Figure 3.15(b) compares $-\Delta\sigma_{2D}(B)$ between $d =$ 10 nm for Bi(111) on mica and on Si(111), indicating that the WAL trace is narrower for Bi(111) on Si(111) than Bi(111) on mica at the same d.

The quantitative analysis of the WAL data was performed by using the theory of Iordanskii, Lyanda-Geller, and Pikus (**ILP**) [14]. The ILP approach and its suitability for our measurements are thoroughly discussed in Section 4.5. In ILP fits, the quantum correction to the 2D conductivity is described by Equation (4.2). From this equation we see that WAL is sensitive to τ_ϕ and τ_{SO}, where τ_ϕ denotes the quantum phase decoherence time, and τ_{SO} is the spin-orbit decoherence time. These form the only two free fitting parameters since we can obtain the elastic scattering time τ_0 through calculations from the values of carrier densities and mobilities (procedure to calculate τ_0 is shown in Section 4.4). In Figure 3.15, the transparent grey traces indicate ILP fits to WAL theory. Figure 3.16 depicts the depen-

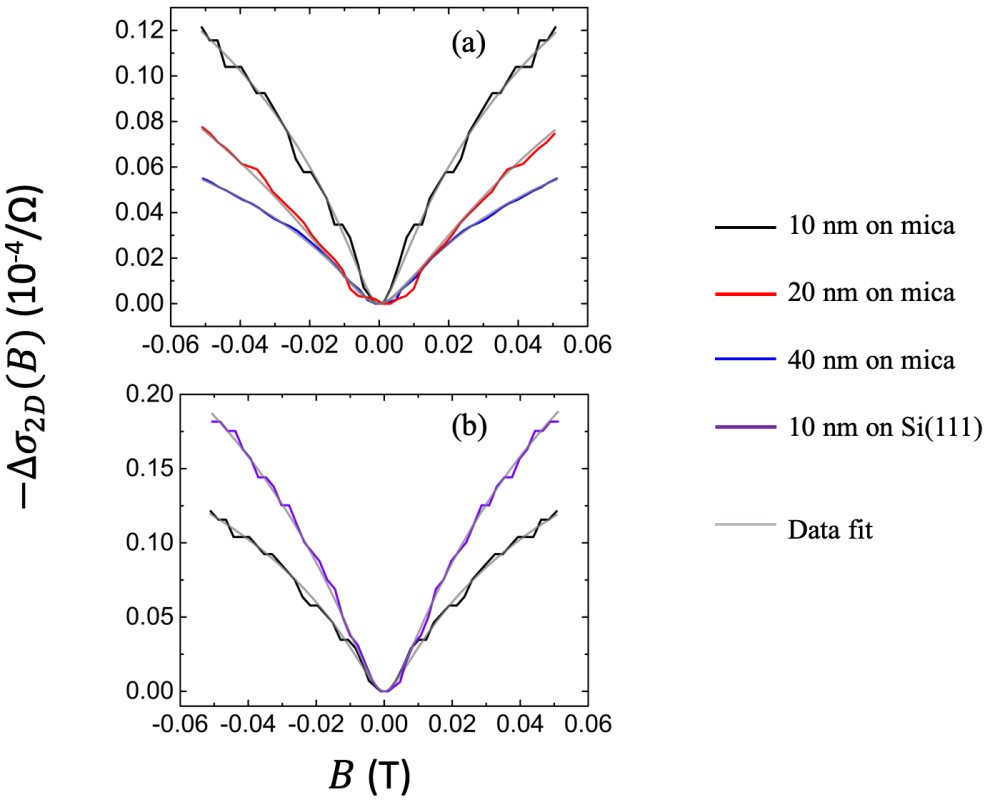

Figure 3.15: 2D conductivity corrections vs B due to WAL. (a) Comparison between Bi(111) films with varying thicknesses on mica. (b) Comparison between 10 nm Bi(111) film on mica and on Si(111). The transparent grey traces indicate fits to WAL ILP theory.

dences of τ_{SO} and τ_ϕ on thickness at $T = 4.1$ K, where black points stand for Bi(111) on mica and red points for Bi(111) on Si(111). With increasing d, τ_{SO} increases, indicating that for thicker Bi(111) films, the overall observed SOI is less strong. This observation is consistent with the fact that at higher d the contribution to the overall conductivity by the interior of the film increases relative to the contribution from the surface states, yet it is the surface states that possess SOI, while SOI is absent in bulk Bi due to inversion symmetry (discussed in Section 1.2). For thinner films the bulk contributes less, so the effectively observed SOI appears stronger. At $d = 10$ nm, the SOI in Bi(111) on mica is stronger (lower τ_{SO}) than the SOI in Bi(111) on Si(111), possibly correlated to the higher surface quality of Bi(111) on mica. We also notice that τ_ϕ decreases with increasing d, possibly indicative of the interplay of the effective Zeeman energy and SOI [124, 125].

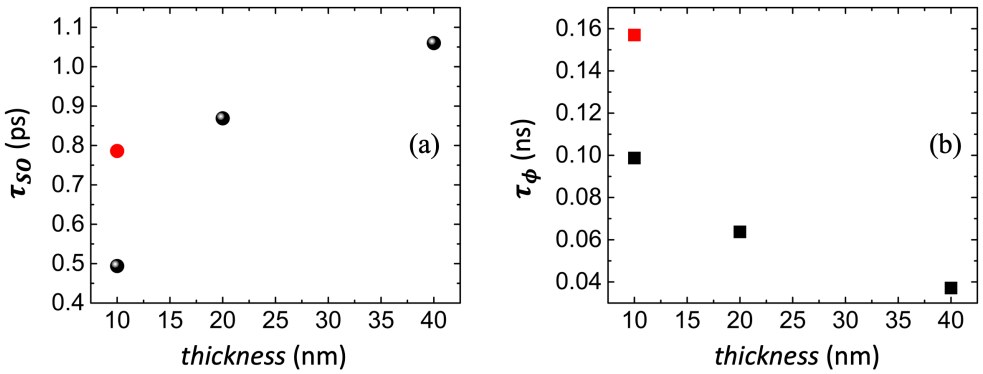

Figure 3.16: (a) Spin-orbit decoherence times τ_{SO} and (b) quantum phase decoherence times τ_{ϕ} extracted from WAL ($T = 4.1$ K), plotted vs Bi(111) thickness. Black points stand for films on mica, red points for films on Si(111).

Chapter 4

Dynamic Nuclear Spin Polarization at Bi(111) Surfaces

The scientific work in this chapter was published as Zijian Jiang, V. Soghomonian, and J. J. Heremans, "Dynamic Nuclear Spin Polarization Induced by the Edelstein Effect at Bi(111) Surfaces", Physical Review Letters **125**, 106802 (2020) (Editors' Suggestion) [91]. Parts of this publication were reused in more or less literal form in this chapter.

In previous work the spin coherence length limited by SOI was studied using WAL experiments in Bi thin films and wires [5, 43]. Prominent among other mechanisms limiting spin coherence lengths is hyperfine interaction (HI) [126, 127, 128, 129, 130], namely the coupling of carrier spins to the nuclear spins. In general and particularly in Bi, HI is less studied, a lack we aim to address by understanding the role of HI in spin decoherence in Bi thin films and mesoscopic structures, and by developing quantum transport-based methods for its study. The approach will consist of establishing a net local carrier spin polarization (CP) mainly through Edelstein effect, creating a net local nuclear spin polarization (NP) by dynamic nuclear polarization (DNP), and studying the effect of the NP on the carriers using quantum transport approaches sensitive to carrier spin coherence and the effective Zeeman fields induced by HI.

The effect that we will here call for short the Edelstein effect (although several researchers contributed to it discovery) generates a non-equilibrium carrier spin polarization (CP) in materials with SOI in response to an applied electric field or a current density $\mathbf{j}$, with the spin polarization direction normal to $\mathbf{j}$ and the surface normal [131, 132, 133, 134, 135]. Since several researchers contributed to its discovery, the effect can be variously named in the literature (e.g. Aronov-Lyanda-Geller-Edelstein effect, ALGE effect), while we adopt a frequently used simplified identifier for it. The Edelstein effect has its origin in spin-momentum locking due to SOI. The effect can be pronounced at surfaces and interfaces with strong SOI, such as the Ag/Bi(111) [65] and Cu/Bi(111) [31] interfaces. Given the strong SOI at the Bi(111) surface, an in-plane $\mathbf{j}$ in a Bi thin film is expected to generate a non-equilibrium in-plane CP. In the present work the Edelstein effect appears as the most plausible dominant origin of the CP under application of $\mathbf{j}$, rather than e.g. lateral or top-and-bottom spin Hall effects, as explained in Section 4.3. Hyperfine interaction (HI) can by dynamic nuclear polarization (DNP) transfer the CP to a non-equilibrium in-plane nuclear spin polarization (NP). The work in this chapter shows such Edelstein-induced DNP, an

example of the interplay between strong SOI, HI, and the Edelstein effect. This chapter also demonstrates that the effect of NP on quantum-coherent transport allows for a quantification of the polarization. The work is reminiscent of recent experiments where CP from the Edelstein effect generates a spin-transfer torque on magnetic moments [136], compared to this work where HI effectively mediates a spin-transfer torque on the nuclear spins. We note that the concept was foreshadowed by theoretical work [137]. DNP from CP resulting from spin injection was previously predicted [138] and the interplay between NP and CP from spin injection, mediated by HI, was studied in Fe/GaAs [139]. Another study used Faraday rotation to study DNP from current-induced NP in InGaAs [140]. The present experiments however differ from the latter [140] by using quantum magnetotransport measurements to quantify the DNP in an all-electrical setup, and by showing that the relatively higher carrier density in the Bi(111) surface states compared to semiconductors [139, 140, 141, 142] allows DNP without application of an external magnetic field, relying only on the effective electronic field created by CP.

This chapter first explains the HI in bismuth, and then describes how HI leads to DNP, and then introduces Edelstein-assisted DNP. The Bi(111) film used in this work is a 40 nm thick Bi film grown on mica, and the growth method has been discussed in Chapter 2. The quantum phase decoherence time and the SOI spin decoherence time are extracted through the fitting of the weak-antilocalization (WAL) data. We show our experimental results in Section 4.6, where the dependences of the Overhauser field on the polarization durations, polarization currents and delay times are discussed. We also demonstrate in this section why an external magnetic field is not needed to overcome the dipole-dipole interaction for the generation of NP in our Bi films.

4.1 Hyperfine Interaction in Bismuth

Hyperfine interaction can be expressed as an energy term $A\mathbf{I}\cdot\mathbf{J}$ where A is the hyperfine coupling constant or energy scale [130, 143, 144, 145, 146, 147, 148], I is the nuclear spin and $\mathbf{J}=\mathbf{S}+\mathbf{L}$ is the carrier angular momentum ($\mathbf{I}$, $\mathbf{J}$ in units of $\hbar$; Refs. [149, 150] contain a more detailed Hamiltonian). Dominantly two mechanisms contribute to HI [143, 149, 150]. As shown in Figure 4.1(a), the Fermi contact interaction requires overlap of the carrier wavefunction with the nuclear site and hence exists for s-band carriers but will be negligible for purely p-band carriers with a wavefunction node at the nucleus. Fermi derived the contact interaction by using Dirac's quantum mechanics of the spinning electron [151], and the energy term is given by $U=-\frac{8}{3}\pi\langle\mu_{\mathbf{n}}\cdot\mu_{\mathbf{e}}\rangle|\Psi(0)|^2$, where $\mu_{\mathbf{n}}$ is the nuclear magnetic moment, $\mu_{\mathbf{e}}$ is the electron magnetic dipole moment (of value the the spin multiplied by the Bohr magneton), and $\Psi(0)$ is the value of the spatial wavefunction of the s-orbital electron at the nucleus. Indeed only the s character band portion to an electron's wavefunction will contribute a non-zero probability density $|\Psi(0)|^2$ at the nucleus. The dipolar interaction [143, 149, 150, 152] results from dipolar magnetic coupling between the nuclear and carrier magnetic moments

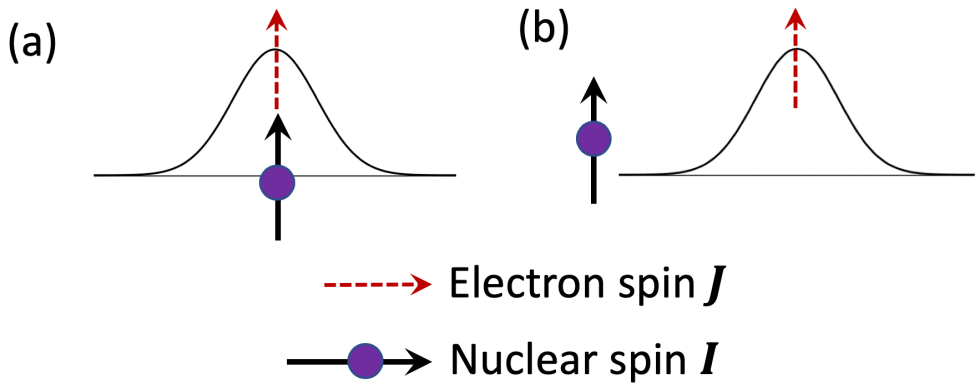

Figure 4.1: A simplified depiction of two mechanisms contributing to hyperfine interaction: (a) Fermi contact interaction, and (b) dipolar interaction.

away from the nuclear site, and dominates for bands with p character, as depicted in Figure 4.1(b). As felt by the carrier, the contact interaction can be cast as an effective B acting on the carrier magnetic moment, whereas the dipolar term results from the actual B of the nucleus [143]. HI can show anisotropy due to crystalline effects. HI can be more pronounced for heavy atoms featuring atomic parameters with higher energy scales [130, 144, 150], and for nuclei with large I. In Bi, with a large $I = 9/2$, both effects play a role, leading to strong HI.

The NMR frequency shift due to HI is referred to as the Knight shift, and quantifies the strength of the HI. A study of the Knight shift in Bi [153] observes a strong coupling between nuclei and carriers, while other NMR studies ascribe a reduced spin-lattice relaxation time (T1) partially to HI [154]. NMR on Bi_2Se_3 [130, 149] again shows a large Knight shift, attributed to a strong HI with specifically ^{209}Bi, of magnitude comparable to that in InSb, PbTe or HgTe [129]. The observed strong HI between carriers and ^{209}Bi nuclei [153] is ascribed to (1) a substantial s-orbital component (rather than pure p character) of $\sim 10\%$, of the electronic wavefunctions at E_F increasing the contact term, and (2) enhancement effects from strong SOI. Both effects are expected to exist in elemental crystalline semimetallic Bi as well. Indeed, the electronic structure in Bi and its surface states [48] shows substantial admixture of s-bands to the p-bands at E_F. Preliminary DFT calculations on 6 bilayer Bi thin films show a 7% s-orbital component of electronic states at the surface, dropping to about 5% in the bulk, and increasing with increasing k-vector away from the band minimum (K. Park, Virginia Tech, private communication; the 7% s admixture is in qualitative agreement with the 10% gauged from NMR). Tight-binding models of (111) surfaces of the heavier elements likewise indicate a generally s-p mixed character [155]. The strong SOI in Bi may also play a role to increase HI [149, 156, 157]. Values for A in semimetallic Bi appear to be lacking. Yet, due to the expected strong HI, several experiments have studied the interaction between Bi donors in Si and the Si s-like conduction band carriers, recently towards using the large HI splitting to construct long-lived qubits [145, 146, 147, 150, 158]. These studies conclude

$A = 6.1\ \mu eV$ ($hA = 1.4754$ GHz), leading to a hyperfine splitting $A(I + 1/2) = 30.5\ \mu$eV in the hydrogenic system consisting of the Bi donor and its s-electron. The Knight shift in Bi_2Se_3 indicates $A = 27\ \mu$eV [130].

Both quoted values of A are substantial (6.1 μeV, 27 μeV), and it is thus reasonable to conclude that consequential HI is expected in semimetallic Bi as well as in Bi compounds, and further also that quantitative information on the strength of the HI is lacking. Also lacking are experiments studying the impact of the HI on spin coherence in electronic transport experiments. Particularly in Bi the role of dimensionality of the surface states and the mutual influences of SOI and HI [149, 152, 156, 157, 159, 160, 161] have not been elucidated. Both effects are important not only in Bi but in Bi-based topological insulators as well. For instance in mesoscopic and nanoscale systems such as quantum wells and surface states [143, 144], quantum wires [152, 161], edge states[129, 162], and quantum dots [127, 128, 148, 159], the reduced dimensionality changes the proximity between electronic and nuclear systems, and hence HI is modified and often enhanced. Other work finds that in high-mobility quantum wells, non-uniformity in NP can impose a limit on carrier mobility [144].

4.2 Hyperfine Interaction and Dynamic Nuclear Polarization

HI can lead to DNP, whereby band carriers undergo a "spin-flip" and nuclei undergo a reverse "spin flop" and a spin polarization is thereby transferred from the carriers to the nuclei [128, 129, 143, 152, 159, 163, 164, 165, 166, 167], as depicted by Figure 4.2. A nonequilibrium spin population in the carrier system then generates a nonequilibrium spin population in the nuclear system (and vice versa). DNP has been used for many years to increase NMR sensitivity by increasing NP above the equilibrium NP achievable at a given T from the Zeeman interaction of the nuclei with an external B [168]. Once NP is established, the band carriers experience the HI as an effective B having the same effect as an external Zeeman field [129, 143, 152], the **Overhauser field $\mathbf{B_{OH}}$**.

In electronic transport, DNP has been observed in InSb under application of a DC current [167] and under transport conditions in narrow constrictions and quantum point contacts where carrier spin-flips were closely matched in energy to nuclear spin-flops [163, 164, 165, 166]. Other techniques using **carrier spin polarization** (**CP**), such as optical pumping and ESR, can also induce DNP.

Due to its ready applicability to mesoscopic structures, we *induce DNP in Bi thin films and mesoscopic structures by application of DC currents*. Two mechanisms are likely active in this avenue to DNP (although not clearly differentiated in the literature). Under high current density without explicitly strong SOI, a setup can be created (e.g. under high B) where carrier spin-flips match the low energy associated with nuclear spin-flops, leading to local DNP at the constriction or point contact [163, 164, 165, 166]. Or, under high

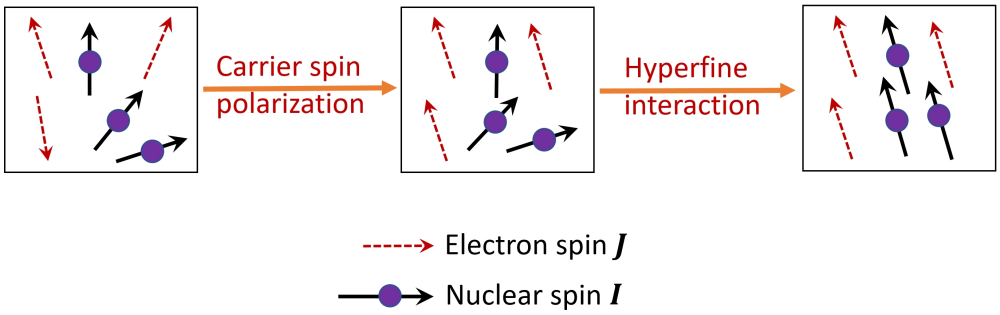

Figure 4.2: A simplified depiction of dynamic nuclear polarization. Once the carrier spin polarization is established, the nonequilibrium spin population in the carrier system generates a nonequilibrium spin population in the nuclear system.

current density but with explicitly strong SOI, DNP also results under a wider range of conditions [167]. Given the substantial SOI in Bi, in this work the second avenue to create DNP is used although the first avenue remains open and useful given the unexplored nature of the properties investigated.

4.3 Edelstein-Assisted Dynamic Nuclear Polarization

The creation of DNP under DC current in materials with substantial SOI (like InSb [167]), can be the result of what we now recognize as the Edelstein effect [131, 169] (also named Rashba-Edelstein effect, spin-galvanic effect or ALGE effect [13]). Due to strong Rashba SOI, the energy parabola of a two-dimensional free electron system is split into two branches, as shown in Figure 4.3(a), and electrons located in the two energy branches have different spin contour directions, as depicted in Figure 4.3(b). The Edelstein effect describes the generation of a nonequilibrium CP in response to an applied $\mathbf{E}$ or current density $\mathbf{j}$, with the spin polarization direction normal to $\mathbf{E}$ or $\mathbf{j}$ [13, 65, 132, 133, 134, 136, 170, 171, 172, 173, 174, 175]. The Onsager-reciprocal, the inverse Edelstein effect, refers to the generation of an electric $\mathbf{j}$ in response to an injected spin current (phenomenologically similar to the inverse spin Hall effect [22, 176], but not necessarily of the same sign) [31, 65, 132, 133, 170, 171, 177]. The Edelstein effect has its origin in spin-momentum locking, characteristic of SOI and topological insulator physics. In essence, $\mathbf{j}$ is associated with excess nonequilibrium $\mathbf{k}$ along its direction, and hence, due to spin-momentum locking, with a net nonequilibrium CP normal to $\mathbf{j}$ [13, 133]. The effect of the external electric field $\mathbf{E}$ or current density $\mathbf{j}$ can be explained by using the semiclassical Boltzmann transport theory [178]. After the application of $\mathbf{E}$, the two Fermi contours shift to the opposite direction of $\mathbf{E}$, causing the creation of CP, as shown in Figure 4.3(c).

In topological insulators, the Edelstein effect can be pronounced [13, 171, 179, 180, 181], and it is strong at surfaces and interfaces with strong SOI, such as the Ag/Bi(111) [65, 177, 182,

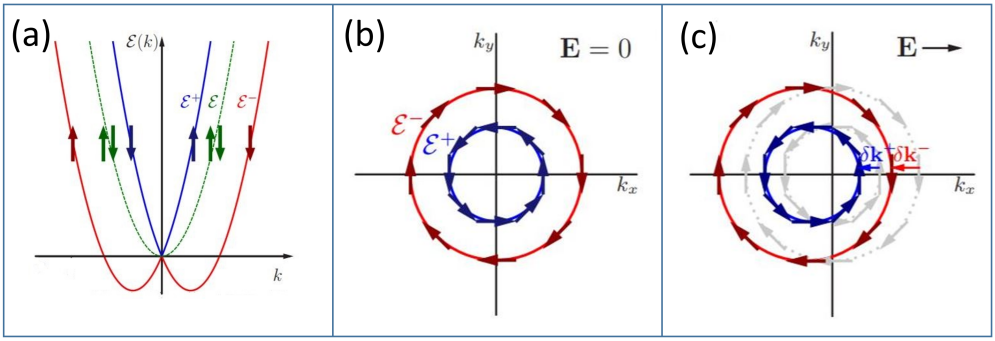

Figure 4.3: A simple explanation of the Edelstein effect. (a) Energy parabola of 2D carrier system split into two branches due to strong Rashba SOI. (b) Without an external electric field **E**, the total carrier spin polarization vanishes. (c) The Fermi contours shift after the application of **E**, resulting in the non-vanishing CP due to the spin-momentum locking. Sourced from [13] with permission.

183, 184] and the Cu/Bi(111) interface [31]. Given the strong SOI at the Bi(111) surface, an in-plane **j** in a Bi thin film generates a nonequilibrium CP and hence by DNP a NP (as happens in InSb [167]). We can call this process Edelstein-assisted DNP (EA-DNP). We can expect a substantial increase over the equilibrium NP available from the Zeeman interaction [168], which at $B = 9$ T and $T = 0.4$ K is 1.4% (using the Brillouin function for $I = 9/2$).

In the present work the Edelstein effect appears as the most plausible dominant origin of the CP under application of **j**, rather than e.g. lateral or top-and-bottom spin Hall effects. Because ferromagnetic materials are absent in the experiments, and because Bi interfaces are known to show strong Rashba-like spin-orbit interaction [1, 58] and the Edelstein effect [30, 31, 177], the latter effect stands out as the origin of the carrier spin polarization. Yet the spin Hall effect in the bulk of the Bi film can also contribute to the carrier spin polarization [30, 177]. The following points reinforce that view.

SOI is absent in bulk Bi due to the existence of inversion symmetry in the bulk. Yet in bulk Bi the spin Hall effect can lead to a bulk carrier spin polarization similar in its effects to the interfacial carrier spin polarization induced by the Edelstein effect [30, 177], and both the spin Hall effect and the Edelstein effect likely contribute to generating the carrier spin polarization. We note however that in this work the Bi is not interfaced with a magnetic material, of which the exchange interaction competes with the interfacial SOI, suppressing or disturbing the interfacial Rashba-like SOI and leading to a reduced Edelstein effect [30]. In the absence of such suppression, and given the known strong Rashba-like SOI at Bi surfaces and interfaces, it is likely that the Edelstein effect is a main contributor to the carrier spin polarization, supplemented however by contributions from the Bi spin Hall effect.

A lateral spin Hall polarization at the edges of the device due to spin-orbit interaction at the

Bi top and bottom interfaces is in principle possible. But, the geometry does not have well-defined edges as it is not a lithographically prepared Bi mesa but a Bi flake with contacts on top. And, the antilocalization measurements sample not only the carrier population at the device edges but average the signal over the entire plane within which the current spreads. Hence in case of lateral spin Hall polarization the antilocalization signal would only return a diluted signal.

The Edelstein effect hence emerges as the main contributor to the dynamic nuclear polarization signature. Both top and bottom Bi interfaces are expected to show an Edelstein effect. While our experiments cannot differentiate between dynamic nuclear polarization signatures from top and bottom interfaces, the top interface of the Bi film is expected to be less disordered, and hence contribute more to transport signatures such as the present dynamic nuclear polarization signature.

4.4 Experimental Approach

We used a 40 nm thick Bi(111) film on mica substrate realized through an optimized van der Waals epitaxy (vdWE) growth. As discussed in Section 2.3, the 40 nm thick Bi(111) was deposited through a shadowmask, yielding samples of diameter about 350 µm, as indicated in Figure 4.4. Au contacts were photolithographically patterned after film deposition. We have shown the morphology of the Bi(111) surface in Section 3.1, where AFM measurements indicated a layered step surface with triangular terraces (Figure 3.4(a)) and indicated a step height between adjacent terraces of 0.391 ± 0.015 nm, corresponding to one Bi(111) bilayer height ($BL_{111} = 0.39$ nm).

The WAL and transport coefficient characterization were carried out by magnetotransport in the ^{3}He immersion cryostat down to $T = 0.39$ K, using standard 4-contact AC lock-in techniques with current of 2 μA rms under applied magnetic field perpendicular to the film plane, $B_\perp$. To develop DNP a high DC polarization current, $I_p = 0.5$ mA to 1.5 mA, $\mathbf{j} \sim 6.25 \times 10^7$ A/m^2 to 1.9×10^8 A/m^2, was applied at $T = 0.39$ K between a pair of contacts for variable polarization durations t_p from 10 to 120 min. I_p was removed after the DNP step, letting the NP and B_{OH} decay slowly with a spin-lattice relaxation time T1 characteristic of the nuclear decoherence [164, 166]. The slow decay allowed time for the subsequent observation of DNP from WAL measurements. For WAL measurements the voltage was measured over the same contacts to which I_p was applied and hence over the path of which B_{OH} develops, as depicted in Fig. 4.5. For the WAL data it is sufficient to sweep $B_\perp$ over ~ 0.2 T, achievable in as little as ~ 15 min, of the order of the expected T1 [185, 186]. Experiments were also performed with different delay times t_{delay}, from 15 to 40 min, inserted between removing I_p and performing the WAL measurement, to characterize the decay in B_{OH} and estimate T1.

N_S and μ were determined from magnetotransport at 0.39 K, indicating predominantly n-

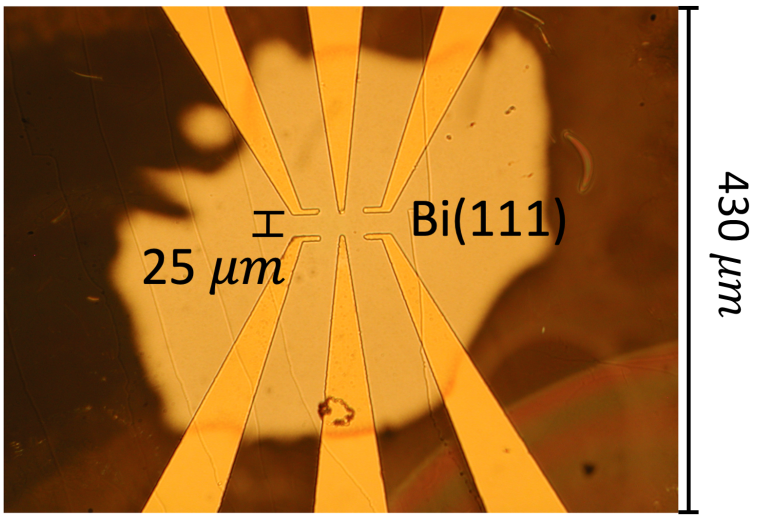

Figure 4.4: Optical micrograph of the 40 nm thick Bi film sample grown on mica by van der Waals epitaxy, with lithographic Au contacts. The diameter of the sample is ~ 350 μm; distance between contacts ~ 25 μm.

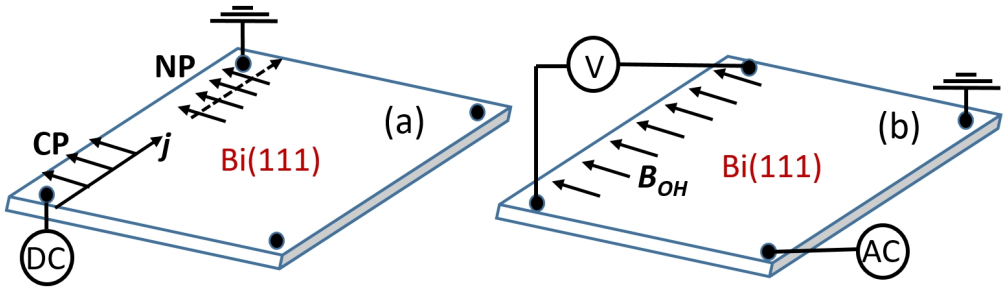

Figure 4.5: Schematic of the Edelstein-induced DNP and WAL setup for Bi(111) surface states. (a) A high DC current density **j** in the Bi film sample induces a surface-state non-equilibrium carrier spin polarization by the Edelstein effect. The surface-state carrier spins are oriented perpendicular to **j**, and induce an in-plane surface nuclear spin polarization via DNP, resulting in in-plane Overhauser field B_{OH}. (b) After **j** is removed and while B_{OH} slowly decays, WAL measurements are carried out.

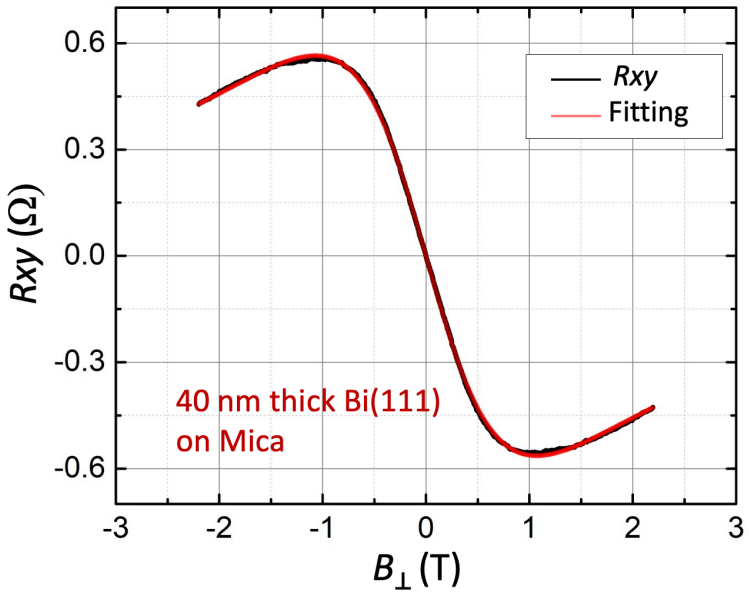

Figure 4.6: Hall resistance vs **B** at 0.4 K and two carrier (electron n and hole p) fitting for a 40 nm thick Bi(111) film on Mica.

type surface carrier contribution. The two-carrier Hall effect fitting is shown in Figure 4.6, from which we determine $N_S = 1.95 \times 10^{15}$ m^{-2}, $\mu = 1.00$ m^2/Vs, $\tau_0 = 0.0856$ ps and mean free path $l_0 = v_f\tau_0 = 20.4$ nm, where v_f is the Fermi velocity derived from N_s. As appropriate for surface states we use the 2D diffusion constant D calculated as $D = \frac{1}{2}v_f^2\tau_0$, at $T = 0.39$ K yielding $D = 0.00243$ m^2/s. WAL results in a characteristic positive quantum correction in $R(B_\perp)$ at $B_\perp \lesssim 0.4$ T, expressed as a small correction to the 2D conductivity $\sigma_2(B)$. We define $\Delta\sigma_2(B_\perp) = \sigma_2(B_\perp) - \sigma_2(B_\perp = 0)$ and $\Delta R(B_\perp) = R(B_\perp) - R_0$ where $R_0 = R(B_\perp = 0)$. Since $\Delta R(B_\perp) \ll R_0$, we have

$$\frac{\Delta\sigma_2(B_\perp)}{\sigma_2(B_\perp = 0)} \approx -\frac{\Delta R(B_\perp)}{R_0} \tag{4.1}$$

allowing fits to $\Delta\sigma_2(B_\perp)$ from the experimental MR.

To calculate $\Delta\sigma_2(B_\perp)$, we first extract $R_\square$ from R_a and R_b at $B_\perp = 0$ T from the van der Pauw data at 0.39 K, calculated as $R_\square = \frac{\pi(R_a+R_b)}{ln2}$. Supposing the MR traces were taken as R_a, we then calculate the ratio factor $\frac{R_\square}{R_a}$ at $B_\perp = 0$ T, which we assume stays the same even when $B \neq 0$. Then we multiply $R_a(B_\perp)$ by this factor to obtain $R_\square(B_\perp)$ in $\Omega/\square$. We know that $\sigma_2 = \frac{1}{R_\square}$, and $\Delta\sigma_2 = \sigma_2(B_\perp) - \sigma_2(B_\perp = 0)$. We call $R_\square(B_\perp = 0) = R_\square(0)$ and $\Delta R_\square(B_\perp) = R_\square(B_\perp) - R_\square(B_\perp = 0) = R_\square(B_\perp) - R_\square(0)$. From these we derived $\Delta\sigma_2(B_\perp) = -\frac{\Delta R_\square(B_\perp)}{R_\square(0)^2}$, which is exactly equation (4.1).

4.5 ILP Fitting of WAL

We performed quantitative analysis of the WAL data using the theory of Iordanskii, Lyanda-Geller, and Pikus (**ILP**) [14], Eq. (13) in the reference. This theory was used because it takes into account Rashba-like spin-orbit interaction (SOI) due to spatial symmetry breaking normal to the surface containing the two-dimensional surface states [70] (SOI is absent in bulk Bi due to inversion symmetry). A theory by Hikami, Larkin and Nagaoka (HLN [4]) is often used to quantify SOI in materials but HLN only accounts for SOI terms cubic in the wavevector, which are either applicable for SOI in hole systems with spin 3/2 (cubic Rashba) or for SOI in material 3D bulk (cubic Dresselhaus). In contrast, ILP accounts for terms both linear in the wavevector (linear Rashba and linear Dresselhaus, the latter an approximation of cubic Dresselhaus) as well as cubic in the wavevector. At Bi(111) surfaces, we expect the linear Rashba term to dominate, and hence the choice of ILP theory, where we set the cubic terms to zero. In Ref [14], Eq. (13), we set $\Omega_3 = 0$ (no cubic Rashba and Dresselhaus terms), and obtain the quantum correction to the 2D conductivity:

$$\begin{aligned}\sigma_2(B_\perp) = &-\frac{e^2}{4\pi^2\hbar}\{\frac{1}{a_0} + \frac{2a_0 + 1 + \frac{H_{SO}}{B_\perp}}{a_1(a_0 + \frac{H_{SO}}{B_\perp}) - \frac{2H_{SO}}{B_\perp}} \\ &- \Sigma_{n=0}^{\infty}(\frac{3}{n} - \frac{3a_n^2 + \frac{2a_n HSO}{B_\perp} - 1 - \frac{2(2n+1)H_{SO}}{B_\perp}}{(a_n + \frac{H_{SO}}{B_\perp})a_{n-1}a_{n+1} - \frac{2H_{SO}}{B_\perp}[(2n+1)a_n - 1]}) \\ &+ 2ln\frac{H_0}{B_\perp} + \Psi(\frac{1}{2} + \frac{H_\phi}{B_\perp}) + 3C\},\end{aligned} \tag{4.2}$$

where

$$a_n = n + \frac{1}{2} + \frac{H_\phi}{B_\perp} + \frac{H_{SO}}{B_\perp}, \tag{4.3}$$

and

$$H_\alpha = \frac{\hbar}{4eD\tau_\alpha}, \tag{4.4}$$

with $\alpha = 0, \phi, SO$.

Here τ_0 denotes the elastic scattering time, τ_ϕ the quantum phase decoherence time, τ_{SO} the SOI spin decoherence time, and the α denote characteristic magnetic fields, while Ψ is the digamma function. The 2D diffusion constant $D = 0.00243\ m^2/\text{s}$ and $\tau_0 = 0.0856$ ps are obtained from conventional longitudinal and Hall resistance measurements. Therefore τ_ϕ and τ_{SO} are the only two remaining free fitting parameters.

To approximate the sum $\Sigma_{n=0}^{\infty}(\frac{3}{n} - \frac{3a_n^2+\frac{2a_nH_{SO}}{B_\perp}-1-\frac{2(2n+1)H_{SO}}{B_\perp}}{(a_n+\frac{H_{SO}}{B_\perp})a_{n-1}a_{n+1}-\frac{2H_{SO}}{B_\perp}[(2n+1)a_n-1]})$, we set the upper limit of n to 30000, which is sufficient as tests showed.

The ILP approach is suitable for the regime where $\Omega\tau_0 < 1$, with Ω representing the spin precession frequency due to spin-orbit interaction. The SOI energy splitting at the Fermi wavevector is expressed as $\Delta_{SO} = \hbar\Omega$ (note that in Ref. [14], $\Omega_1 = \frac{1}{2}\Omega$). An approach by Golub *et al.* [187] is in theory more appropriate than the ILP approach if $\Omega\tau_0 > 1$. The Golub approach was developed as a refinement of ILP for cases where spin-orbit interaction is strong (high Ω) or mobility is high (long τ_0, *e.g.* for ballistic transport or as appropriate for III-V semiconductors). We obtain values for Ω from the expression $\frac{1}{\tau_{SO}} = \frac{1}{2}\Omega^2\tau_0$ [70] using τ_{SO} from the results shown later in Figure 4.9. With $\tau_0 = 0.0856$ ps, taking a worst case $\tau_{SO} \approx 1$ ps (Figure 4.9(a)), we find $\Omega\tau_0 = (\frac{2\tau_0}{\tau_{SO}})^{1/2} \approx 0.4 < 1$. Hence the use of the ILP approach is justified. While SOI in the present Bi surface states is strong (high Ω), the carrier mobility is fairly low compared to e.g. III-V semiconductors (shorter τ_0), rendering ILP a satisfactory formalism.

The ILP analysis should be restricted to magnetic fields $B_\perp$ below the characteristic field $H_0 = \frac{\hbar}{4eD\tau_0} = \frac{\hbar}{2el_0^2}$, where $l_0 = v_f\tau_0$ denotes the mean free path. With $_0 = 20.4$ nm, we find $H_0 = 0.79$ T, well above the range -0.04 T $< B_\perp <$ 0.04 T we use for the analysis. The magnetoresistance data was obtained in each case with $B_\perp$ ranging over $\pm$ 0.2 T, while the ILP fitting was performed only over the subrange $\pm$ 0.04 T. The wider experimental range $\pm$ 0.2 T was used out of caution, to ascertain that the sample's behavior had not changed in unaccountable ways that would indicate a lack of continuity in the data series, even though this did slow down the measurements. The fitting range was restricted to $\pm$ 0.04 T to make sure no other magnetoresistance phenomena, such as the almost inevitable geometrical magnetoresistance, would contaminate the analysis. Yet for the ILP fitting it is important to capture the characteristic sharp dip in $R(B_\perp)$ at $B_\perp \approx 0$, as well as the gradual lessening of $dR/dB_\perp$ at higher $B_\perp$. The range $\pm$ 0.04 T proved optimal to avoid other magnetoresistance phenomena as well as to capture WAL features necessary for the ILP fit, and amply satisfies the criterion $B_\perp < H_0$.

4.6 Experimental Results

The ILP fits are performed for WAL obtained after different t_p and t_{delay} under different I_p. From the fits, we find the dependences on t_p, t_{delay} and I_p of τ_{SO} and τ_ϕ. From the latter the dependences of B_{OH} are determined.

Figure 4.7 depicts representative MR of the Bi film sample at $T = 0.39$ K before and after DNP using variable I_p ranging from 0.5 mA to 1.5 mA and t_p ranging from 0 (before DNP) to 120 min (at $t_{delay} = 0$). The positive MR characteristic of WAL is observed both before and after DNP. The traces for $R(B_\perp)$ (Fig. 4.7) shows a widening vs $B_\perp$ for $B_\perp \neq 0$ after

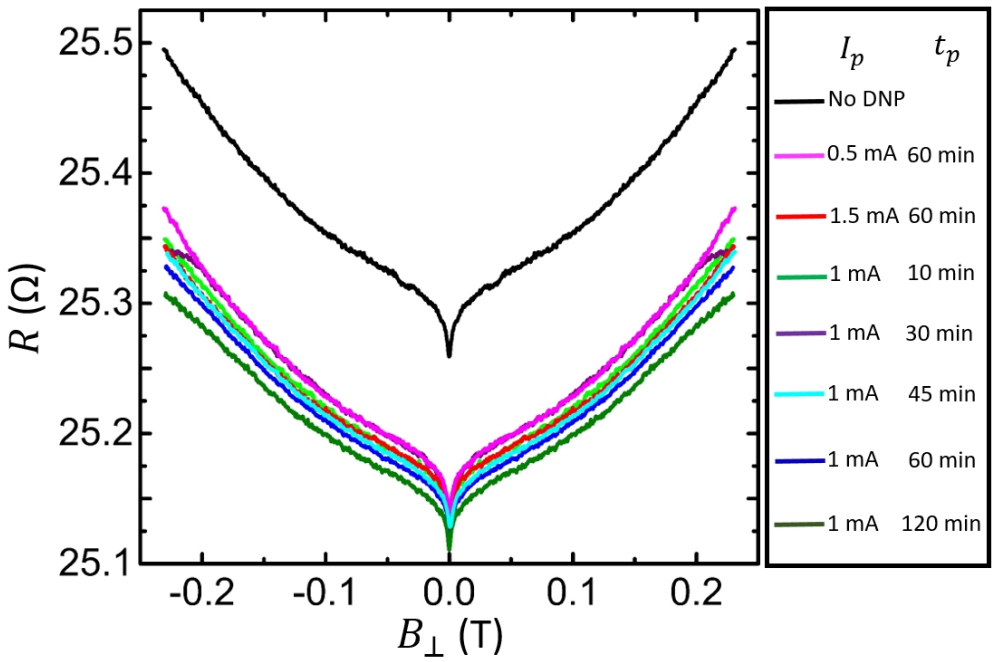

Figure 4.7: AL magnetoresistance at $T = 0.39$ K before (indicated as No DNP) and after DNP with variable I_p and variable t_p ($t_{delay} = 0$; traces not offset). After DNP a widening of $R(B_\perp)$ vs $B_\perp$ for $B_\perp \neq 0$ is evident.

DNP, characteristic of an increase in τ_{SO} (decreasing effect of SOI) and a decrease in τ_ϕ as confirmed below. The widening shows a dependence on I_p and t_p, with long $t_p = 120$ min at $I_p = 1$ mA resulting in the largest effect. The dependence on t_p and I_p suggests DNP and hence B_{OH} play a role in changing τ_{SO} and τ_ϕ. Before we present quantitative data on τ_{SO} and τ_ϕ, we note that the WAL results after DNP are qualitatively consistent with the existence of in-plane B_{OH}. Phenomenologically, after removing I_p, B_{OH} persists and generates an effective Zeeman energy $g^*_\parallel \mu_B B_{OH}$, where $g^*_\parallel$ denotes the in-plane g-factor (for Bi(111) surface states, $g^*_\parallel \approx 33$ [188]) and μ_B denotes the Bohr magneton. B_{OH} partially aligns the carrier spins and suppresses the spin phase shift due to SOI and thereby weakens WAL [125, 189, 190]. The effect leads to a widening of the characteristic sharp minimum in $\Delta R(B_\perp)$ vs $B_\perp$ and is quantified by a lengthening of τ_{SO}. Further, B_{OH} results in a spin-induced TRS breaking [124, 125, 190], leading to a decrease in τ_ϕ. While it is not in the scope of this experimental study to modify the ILP theory to include HI, future theoretical studies specific to the influence of HI and NP on WAL may help refine quantitative aspects of the experiments, as was performed for ferromagnetic order [189] and for Zeeman interaction [124].

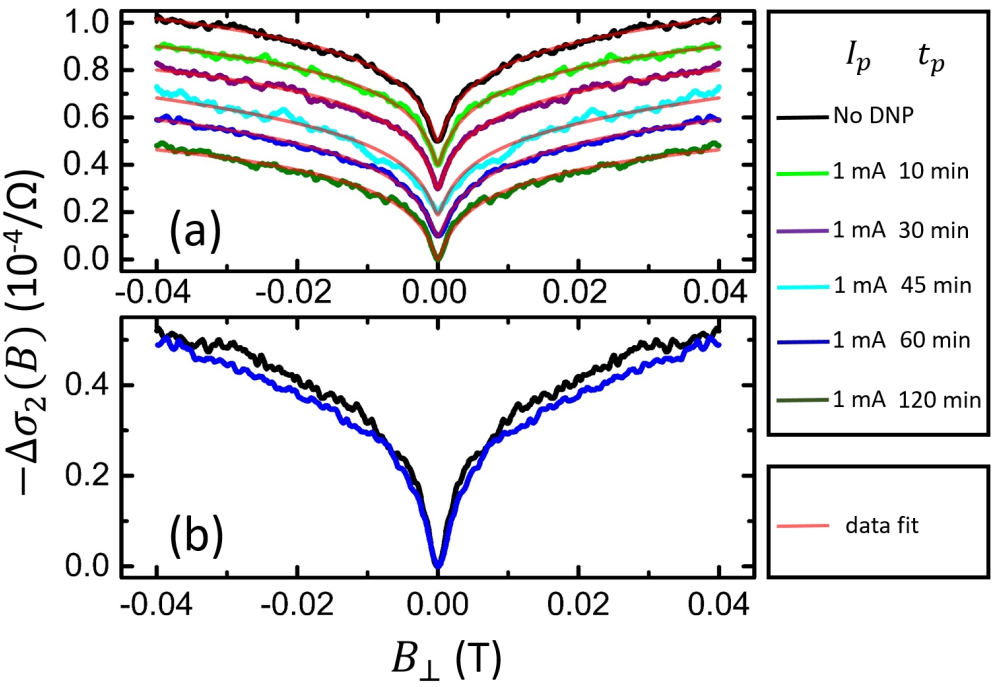

Figure 4.8: 2D conductivity corrections due to WAL at $T = 0.39$ K and at low $B_\perp$ ($t_{delay} = 0$): (a) under variable t_p with $I_p = 1$ mA. The red traces indicate fits to the WAL theory [14]. Data are offset for clarity; (b) before DNP (black trace) and after DNP (blue trace) with t_p = 60 min and $I_p = 1$ mA (traces not offset). The widening of the trace after DNP indicates a partial suppression of WAL by B_{OH}.

4.6.1 Dependence on t_p

We first investigated the 2D conductivity corrections due to WAL under variable t_p with a fixed I_p, which is shown in Figure 4.8 with the ILP fits. The negative of $\Delta\sigma_2(B_\perp)$ (reproducing $\Delta R(B_\perp)$) at low $B_\perp$ is displayed in Fig. 4.8(a) for variable t_p when $I_p = 1$ mA (at $t_{delay} = 0$). Best fits to the ILP theory [14] overlay the data in Fig. 4.8(a) in red and indicate that the theory excellently captures the WAL in the Bi(111) surface states and will allow reliable extraction of values for τ_{SO} and τ_ϕ. The widening of the minimum in $-\Delta\sigma_2(B_\perp)$ is illustrated in Fig. 4.8(b) where the black trace represents $-\Delta\sigma_2(B_\perp)$ before DNP and the blue trace after DNP with $t_p = 60$ min and $I_p = 1$ mA (at $t_{delay} = 0$).

The dependences of τ_{SO} and τ_ϕ on t_p at fixed $I_p = 1$ mA with $t_{delay} = 0$ are presented in Fig. 4.9(a)-(b). The value of τ_{SO} increases with increasing t_p (Fig. 4.9(a)), indicative of the influence of the in-plane B_{OH}. A phenomenological understanding was presented above. Theoretical studies of the combined influence of SOI and $B_\parallel$ on an inhomogeneous interfacial spin distribution [191] show that even a weak $B_\parallel$ results in a decrease of the spin density proportional to $1/(2\pi D\tau_{SO})$, relating an increase in τ_{SO} to the influence of $B_\parallel = B_{OH}$. Figure 4.9(b) shows a decrease of τ_ϕ with increasing t_p, and similar to Fig. 4.9(a) manifests a

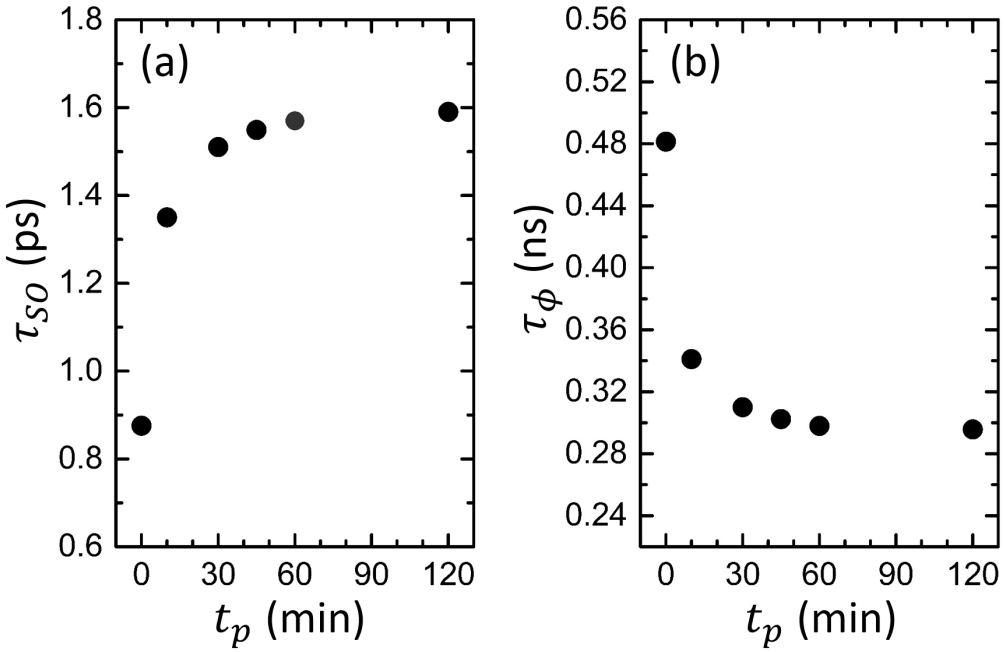

Figure 4.9: (a) Spin-orbit decoherence times τ_{SO} and (b) quantum phase decoherence times τ_ϕ at $T = 0.39$ K and $I_p = 1$ mA, vs DNP duration t_p ($t_{delay} = 0$). Data without DNP stand in for $t_p = 0$.

saturation at higher t_p. The decrease of τ_ϕ with increasing t_p is indicative of the interplay of the effective Zeeman energy and SOI [124, 125], predicted to result in a quadratic dependence of τ_ϕ on $B_\parallel$ [125]:

$$\frac{\tau_\phi(B_\parallel)}{\tau_\phi(B_\parallel = 0)} = \frac{1}{1 + cB_\parallel^2}, \tag{4.5}$$

where $c = \tau_\phi(B_\parallel = 0)\tau_{SO}(B_\parallel = 0)(g_\parallel^* \mu_B/\hbar)^2$. The estimated average value of $B_{OH} = B_\parallel$ can be calculated from the data using Eq. (4.5). Figure 4.10 shows the average B_{OH} calculated from τ_ϕ in Figure 4.9(b). Since the WAL measurement (sweeping over $B_\perp \sim 0.2$ T after removing I_p and waiting t_{delay}) spans ~ 15 min, by estimated average B_{OH} is meant the value after averaging over these ~ 15 min. Current spreading between the current contacts over the sample geometry during DNP will likely lead to non-uniform DNP, and B_{OH} hence encompasses spatial averaging as well. To minimize handling of the data, the averaging effects are not accounted for in Figure 4.10 but should be kept in mind. In Figure 4.10 the average B_{OH} increases with increasing t_p, and saturates at about 13 mT. An exponential fit showed that the increase towards saturation occurs with a characteristic time T1e = 6 ... 11 min, with T1e characterizing the expected nuclear spin alignment by DNP [142].

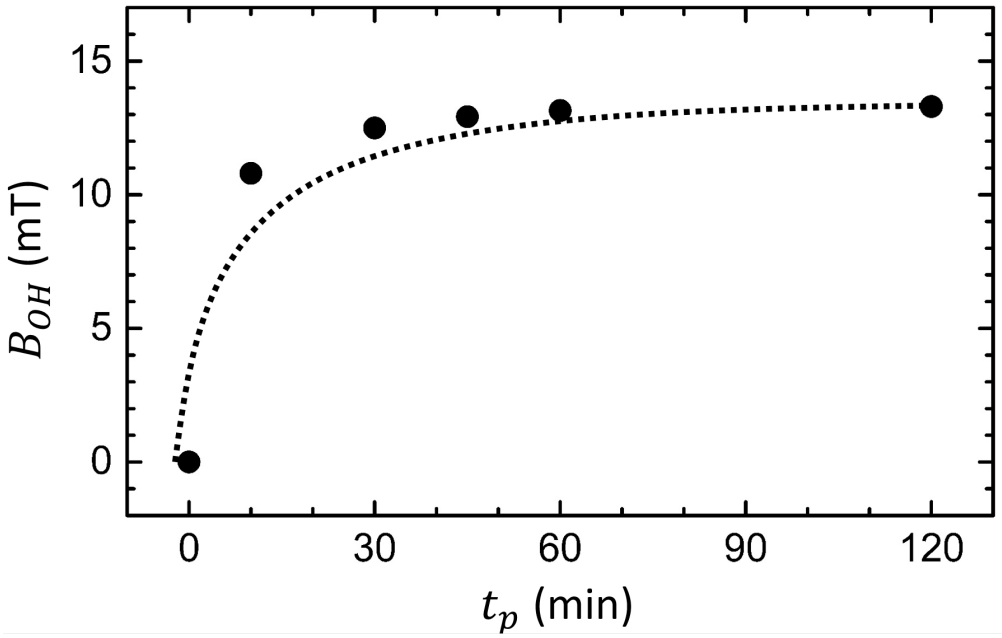

Figure 4.10: Overhauser field B_{OH} at $T = 0.39$ K and $I_p = 1$ mA, vs DNP duration t_p ($t_{delay} = 0$). Data without DNP stand in for $t_p = 0$. The black dotted line is a guide to the eye.

4.6.2 Effective Hyperfine Fields

The nonequilibrium nuclear spin polarization (NP) in this work, and hence the effective nuclear Overhauser magnetic field B_{OH} experienced by the electrons, result from the generation of a nonequilibrium electron spin polarization. Yet for dynamic nuclear spin polarization (DNP) to occur, the dipole-dipole interaction field B_L between neighboring nuclei needs to be overcome (B_L is typically a fraction of mT). Unless overcome by a nuclear Zeeman energy, this interaction will lead to a rapid relaxation of the nonequilibrium nuclear spin, with a relaxation time T2 $\sim$ 0.1 ms [139, 141, 142]. The characteristic time for development of the NP by hyperfine interaction with electrons is denoted T1e. Since T1e $\gg$ T2, the NP can be ignored unless B_L responsible for the T2 relaxation is overcome by an actual or effective magnetic field B_{eff} experienced by the nuclei, requiring $B_{eff} \gg B_L$ [139, 141, 142]. Further, given B_{eff}, the nuclear spin system is effectively isolated from the lattice because the nuclear spin-lattice relaxation is characterized by a time T1 $\gg$ T2 (the isolation of the nuclear spin system from the lattice allows the definition of a nuclear spin temperature, as distinct from lattice temperature or electron temperature) [142]. The average nuclear spin after polarization is given by I_{av}:

$$
\begin{aligned}
I_{av} &= IB_I(x), \\
x &= Iln[(\frac{1+2S_{av}}{1-2S_{av}})(\frac{1+2S_{th}}{1-2S_{th}})], \\
S_{th} &= \frac{1}{2}tanh(\frac{\mu_B g_\parallel B}{2k_B T}),
\end{aligned}
\tag{4.6}
$$

where $I = 9/2$ is the Bi nuclear spin, and $B_I(x)$ is the Brillouin function for I [142]. S_{av} is the average electron spin after electron spin polarization, S_{th} is the equilibrium value of the average electron spin at $B = B_{OH}$ and temperature T, μ_B is the Bohr magneton and $g_\parallel$ the in-plane g-factor ($g_\parallel \approx 33$ for Bi(111) surface states [188]). S_{av} is limited by $S_{th} < S_{av} < \frac{1}{2}$. At the value $B_{OH} = 13$ mT obtained from the experiments and at T = 0.39 K, we find S_{th} = 0.177. $\mathbf{I_{av}}$ is colinear with $\mathbf{S_{av}}$. We note that for the limits $S_{av} \to S_{th}$ we have $I_{av} \to 0$, and for $S_{av} \to \frac{1}{2}$ we have $I_{av} \to I = 9/2$.

An estimate of B_L can be obtained [142] from the dipole expression $B_L = \frac{\mu_0 \mu_I}{4\pi a^3}$, where μ_I denotes the nuclear magnetic moment with $\mu_I = I\mu_N$ (with μ_N the nuclear magneton and I = 9/2), a denotes the interatomic distance in Bi and μ_0 the permeability of vacuum. Using $a \approx a_{Bi} = 454$ pm, the bulk lattice constant of Bi in a plane normal to the trigonal axis, we find $B_L \approx 0.024$ mT.

The hyperfine interaction is experienced by the electrons as an in-plane B_{OH} yielding an effective Zeeman energy, described by $g_\parallel \mu_B B_{OH} = AI_{av}$, where A denotes the hyperfine coupling constant [130, 143]. The field $\mathbf{B_{OH}}$ is colinear with $\mathbf{I_{av}}$. In case of Fermi contact interaction, A can be expressed as [142]:

$$
A = \frac{4}{3}\mu_N \mu_B \mu_0 \eta N, \tag{4.7}
$$

where η denotes the squared Bloch wave function amplitude at the site of the nucleus and N the volume density of nuclei in the material. In Bi, experiments have concluded $A \approx 6.1$ μeV ... 27 μeV [130, 145, 146, 150]. We note that η can be large ($\eta \approx 10^3$ ... 2×10^4) because the electron density has a sharp maximum at the nucleus. In Bi, $N = 2.82 \times 10^{27}$ nuclei/m^3. For $A \approx 6.1$ μeV ... 27 μeV we find $\eta \approx 4.41 \times 10^3$ ... 1.95×10^4, within the range of expectations. We rewrite:

$$
B_{OH} = \frac{AI_{av}}{g_\parallel \mu_B} = \frac{4\mu_N \mu_0 \eta N I_{av}}{3g_\parallel}. \tag{4.8}
$$

Similarly, spin-polarized electrons result, via hyperfine interaction, in an in-plane magnetic field Be experienced by the nuclei expressed as [142]:

$$
B_e = -\frac{4}{3}\mu_B \mu_0 \eta n_e S_{av}, \tag{4.9}
$$

where n_e denotes the electron density (here estimated for the Bi(111) surface states). We hence have:

$$B_e = \frac{AS_{av}n_e}{\mu_N N}, \tag{4.10}$$

which can be compared to Eq. (4.8). The field $\mathbf{B_e}$ is colinear with $\mathbf{S_{av}}$. Hence, $\mathbf{S_{av}}$, $\mathbf{I_{av}}$, $\mathbf{B_{OH}}$ and $\mathbf{B_e}$ are all colinear. It was found experimentally that if the field B_e generated by spin-polarized electrons is sufficiently large, then B_e functions as a B_{eff} surmounting dephasing by B_L, and allows for DNP [142]. In experiments on semiconductors, where the carrier density is low, typically we have $n_e/N \ll 1$, and the effect of B_e is negligible ($B_e < B_L$). In semiconductors, application of a small external magnetic field is hence necessary to obtain NP [139, 140, 141, 142]. However, in semimetals such as Bi, carrier densities are substantially higher and n_e/N is larger. As we will see, this results in $B_e \gg B_L$, allowing DNP to occur. The areal electron surface state density $N_S = 1.95 \times 10^{15}$ m^{-2}, as determined from magnetotransport at temperature $T = 0.39$ K. Assuming the surface states are localized in the top Bi bilayer (an approximation) of thickness 0.39 nm, we obtain $n_e \approx 5.00 \times 10^{24}$ m^{-3}. This yields $n_e/N \approx 1.8 \times 10^{-3}$.

Values for I_{av}, B_{OH} and B_e depend on values for A and/or S_{av}. A is only known within a range from the literature, while S_{av} is in the experiment not independently determined. The interaction between the spin-polarized electron current and the nuclei is also subject to nonuniformity due to current spreading. Yet, we show below that the ranges 6.1 μeV $< A <$ 27 μeV and $S_{th} < S_{av} < \frac{1}{2}$ yield B_{OH} values compatible with $B_{OH} \approx 13$ mT obtained in the experiments, and that $B_e \gg B_L \approx 0.024$ mT in all cases. Figure 4.11(a) shows B_{OH} plotted vs S_{av} ($S_{th} = 0.177 < S_{av} < 0.40$) for $A = 6.1$ μeV and $A = 27$ μeV, with $S_{th} = 0.177$, where the level $B_{OH} = 13$ mT is indicated. Figure 4.11(b) shows B_e plotted vs S_{av} ($S_{th} = 0.177 < S_{av} < 0.4$) for $A = 6.1$ μeV and $A = 27$ μeV.

Figures 4.11(a) and (b) show that at $A = 6.1$ μeV, we have $B_{OH} = 13$ mT for $S_{av} = 0.37$, yielding $B_e = 0.129$ T. At $A = 27$ μeV, we have $B_{OH} = 13$ mT for $S_{av} = 0.20$, yielding $B_e = 0.305$ T. Both values for S_{av} are realistic, and in both cases $B_e \gg B_L \approx 0.024$ mT. In Figure 4.12(a) we have plotted B_e vs A assuming $S_{th} = 0.177$ and $B_{OH} = 13$ mT, showing that all values of A result in $B_e \gg B_L$.

The calculations hence show that in the experiments the field B_e generated by spin-polarized electrons is amply sufficiently large to surmount dephasing by B_L, and to allow for DNP. The observed $B_{OH} = 13$ mT is also consistent with the present knowledge of A in Bi.

As a test, we performed DNP measurements with an external in-plane magnetic field $B_\parallel$ applied during the nuclear polarization, with $B_\parallel = 0.1$ T and 1.0 T ($B_\parallel \approx B_e$ while $B_\parallel \gg B_L$). $B_\parallel$ was applied in-plane and normal to the average current density direction of I_p, hence colinear with the expected $\mathbf{S_{av}}$, $\mathbf{I_{av}}$, $\mathbf{B_{OH}}$ and $\mathbf{B_e}$. The in-plane field measurements were performed at $T = 1.30$ K, the lowest T in the system allowing in-plane fields, and are depicted in Figure 4.12(b). The figure contains the antilocalization (AL) magnetoresistance (MR, negative of conductivity correction $\Delta\sigma_2$) plotted as $-\Delta\sigma_2(B_\perp)$ vs $B_\perp$, where $B_\perp$ denotes the

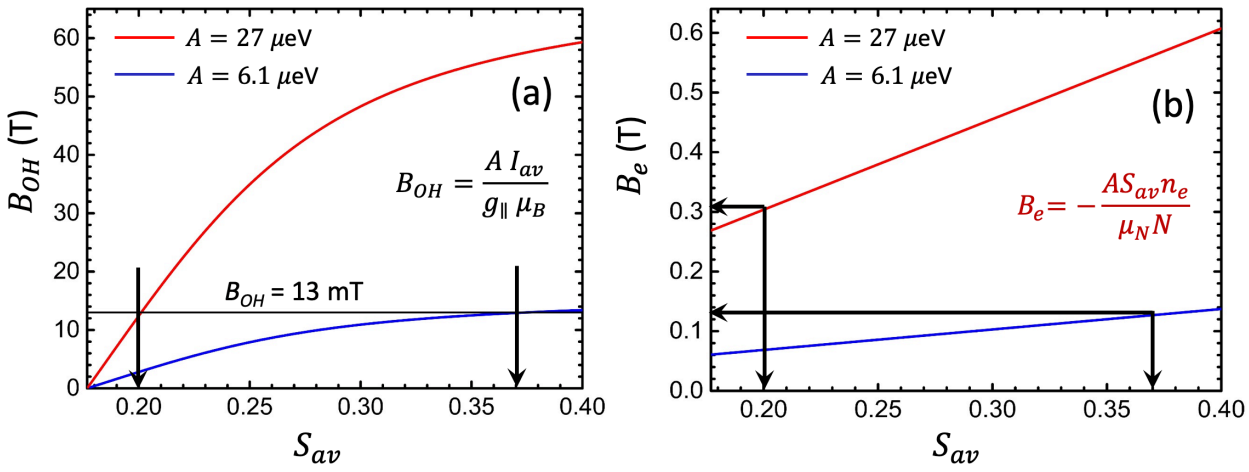

Figure 4.11: (a) Calculated B_{OH} vs S_{av} for $A = 6.1$ μeV (blue) and $A = 27$ μeV (red), with $B_{OH} = 13$ mT indicated as a black line. At $A = 6.1$ μeV, BOH = 13 mT is reached at $S_{av} = 0.37$. At $A = 27$ μeV, $B_{OH} = 13$ mT is reached at $S_{av} = 0.20$, as indicated by the black arrows. (b) Calculated B_e vs S_{av} for $A = 6.1$ μeV (blue) and $A = 27$ μeV (red). At $A = 6.1$ μeV, $S_{av} = 0.37$ yields $B_e = 0.129$ T. At $A = 27$ μeV, $S_{av} = 0.20$ yields $B_e = 0.305$ T. In both cases, $B_e \gg B_L$.

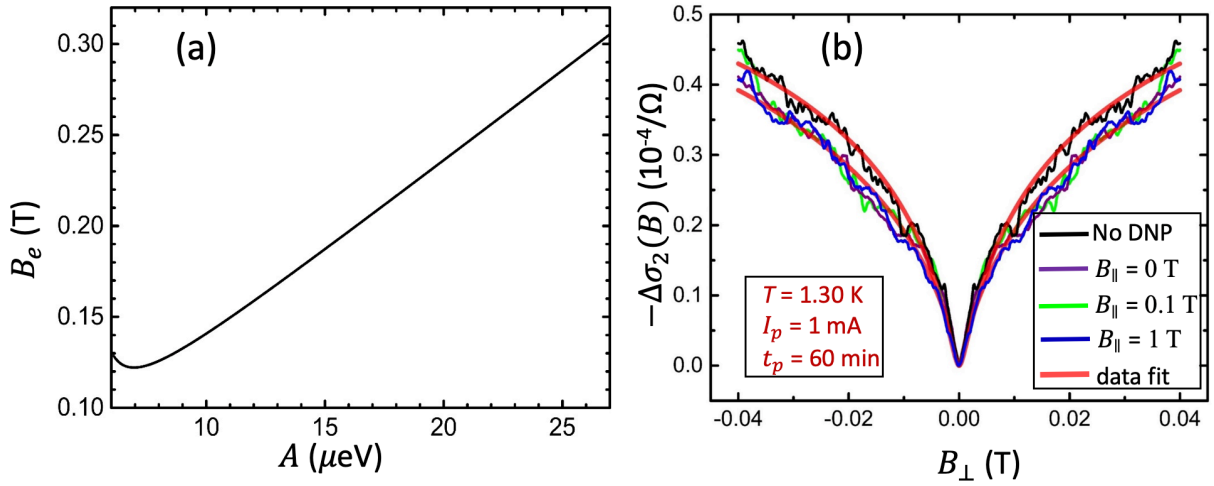

Figure 4.12: (a) Calculated B_e vs A for $A = 6.1$ μeV to 27 μeV assuming $B_{OH} = 13$ mT. All values of A in this range result in $B_e \gg B_L$. (b) 2D conductivity corrections due to WAL at $T = 1.30$ K and at low $B_{\perp}$, under $B_{\parallel} = 0$, 0.1 T and 1.0 T. The black trace was obtained before DNP, the other traces after DNP with $t_p = 60$ min and $I_p = 1$ mA. Traces are offset for zero conductivity correction at $B_{\perp} = 0$ for ease of comparison. The red traces indicate fits to WAL theory.

magnetic applied normally to the surface. Figure 4.12(b) contains a comparison MR trace where no DNP was performed, three MR traces with DNP under $I_p = 1$ mA applied for $t_p =$ 60 min, and two data fits. The salient point is that no viable difference was detected between the MR traces with DNP for $B_{\|}$ =0, $B_{\|} = 0.1$ T and $B_{\|} = 1.0$ T. The identical data fitting to these three traces bears this out. The MR traces with DNP however differ from the MR trace (and data fits) without DNP, in the expected manner. Hence, application of $B_{\|}$ does not change the DNP process. The reason lies in the fact that the nuclear spin relaxation due to B_L is already amply suppressed by $B_e \gg B_L$ and hence application of $B_{\|}$ does not measurably add additional suppression.

Although the data in Figure 4.12(b) was obtained at $T = 1.30$ K, for completeness we mention the results of the WAL data fit under DNP: $\tau_\phi = 0.118$ ns, $\tau_{SO} = 1.35$ ps, B_{OH} = 12.65 mT. We note that the lower value of B_{OH} at $T = 1.30$ K is influenced by the thermal broadening of the WAL MR at higher T, expressed in a lowering of τ_ϕ for rising T as expected, and hence should not be interpreted as a drop in B_{OH} with rising T. The characterization of DNP by the WAL method requires low T so that the thermal lowering of τ_ϕ does not obscure the lowering of τ_ϕ due to B_{OH}.

4.6.3 Dependence on I_p and Conversion Efficiency

The in-plane Overhauser field B_{OH} shows a dependence on the DC polarization current I_p, as we show in this section. DNP experiments were performed with $I_p = 0.5$ mA, 1 mA, and 1.5 mA at fixed polarization duration $t_p = 60$ min, at $T = 0.39$ K. $I_p \geq 2$ mA was not used, because with $I_p = 2$ mA a momentary small rise of T by about 10 mK was observed for about 20 s after applying I_p, and hence it could not be fully ascertained that sample heating was negligible. Figure 4.13 depicts WAL MR (negative of conductivity correction $\Delta\sigma_2$) plotted as $-\Delta\sigma_2(B_\perp)$ vs $B_\perp$, where $B_\perp$ denotes the magnetic applied normally to the surface, parametrized in $I_p = 0$ mA, 0.5 mA, 1 mA, and 1.5 mA ($t_p = 60$ min and $T =$ 0.39 K). The data at $I_p = 0$ mA denotes a measurement without DNP. Best fits to the ILP theory [14] are indicated as red lines and allow reliable extraction of values for τ_{SO} and τ_ϕ.

The dependences of τ_{SO} and τ_ϕ on I_p at $T = 0.39$ K are presented in Fig. 4.14. The value of τ_{SO} increases sublinearly with increasing I_p, while the value of τ_ϕ decreases with increasing I_p. Both are due to increased influence of B_{OH} after using higher I_p. The decrease in τ_ϕ is directly linked to higher B_{OH} with higher I_p.

The estimated average value of B_{OH} was calculated from τ_ϕ using Eq. (4.5), and plotted vs I_p in Fig. 4.15. B_{OH} increases sublinearly with I_p but does not saturate for $I_p \leq 1.5$ mA. The results in Fig. 4.15 are consistent with increasing I_p leading to increasing nuclear polarization, as expected. Figure 4.15 shows that B_{OH} vs I_p strongly resembles a Brillouin function shape, which can be understood from the discussion in section 4.6.2.

We denoted S_{av} the average electron spin polarization due to the Edelstein effect (sec-

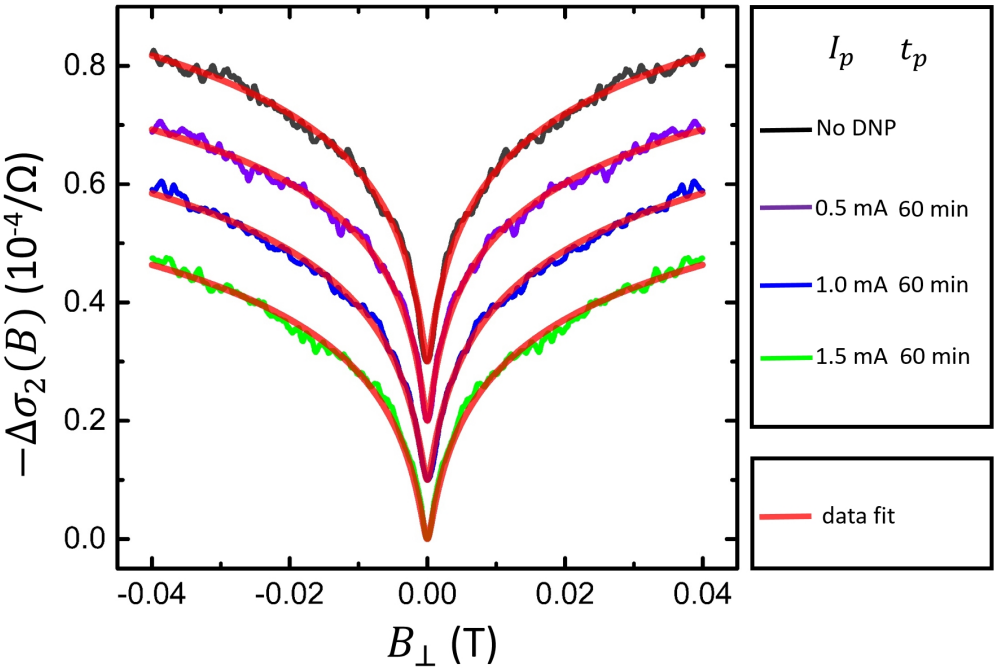

Figure 4.13: 2D conductivity corrections vs $B_\perp$ due to WAL, parameterized in $I_p = 0$ mA, 0.5 mA, 1 mA, and 1.5 mA ($t_p = 60$ min and $T = 0.39$ K). The black trace at $I_p = 0$ mA denotes a measurement without DNP. The red traces indicate fits to WAL theory.

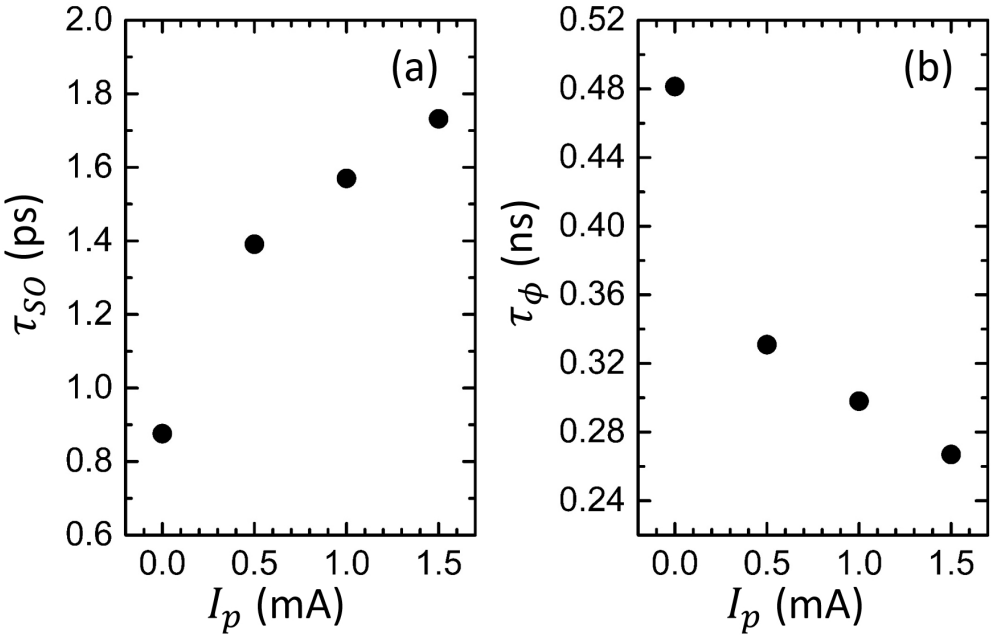

Figure 4.14: (a) Spin-orbit decoherence times τ_{SO} and (b) quantum phase decoherence times τ_ϕ extracted from WAL ($t_p = 60$ min and $T = 0.39$ K), plotted vs different polarization currents I_p. The data without DNP is indicated as $I_p = 0$.

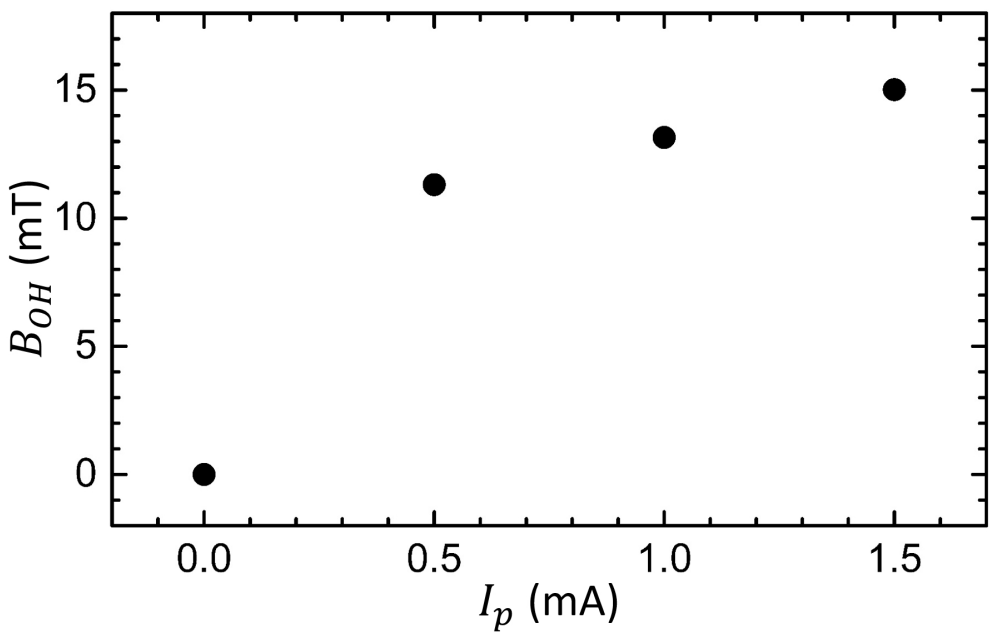

Figure 4.15: Overhauser field B_{OH} plotted vs different polarization currents I_p ($t_p = 60$ min and $T = 0.39$ K). The data without DNP is indicated as $I_p = 0$.

tion 4.6.2). S_{av} is due to charge-current to spin conversion via the Edelstein effect and S_{av} is expected to depend linearly on I_p with a proportionality constant describing the charge-current to spin conversion efficiency, $S_{av} = \alpha I_p$. Then, since B_{OH} vs S_{av} follows a Brillouin function, it is expected that B_{OH} vs I_p also follows a Brillouin function. However, a qualitative predictive model linking B_{OH} and I_p depends on either knowledge of a specific value for the hyperfine constant A or of the proportionality constant α. The latter will in our samples not only depend on the intrinsic charge-current to spin conversion efficiency of the Edelstein effect, but will also depend on sample geometry due to current spreading. As explained, the calculated B_{OH} reflects a spatial averaging due to current spreading over the sample geometry between the two current contacts, which likely results in non-uniform DNP. The hyperfine constant A is from the literature only known within a range, $A \approx 6.1$ μeV ... 27 μeV [130, 145, 146, 150]. For every given B_{OH} (given I_p) we can calculate a range of S_{av} depending on A. From this range of S_{av} we can then also only obtain a range of α and not a specific value. Given the uncertainty in A and the spatially non-uniform DNP, a precise analysis of charge-current to spin conversion efficiency and of α would be conjectural. Yet, the resemblance to the expected Brillouin function shows a strong consistency between the theoretical expectations and our results.

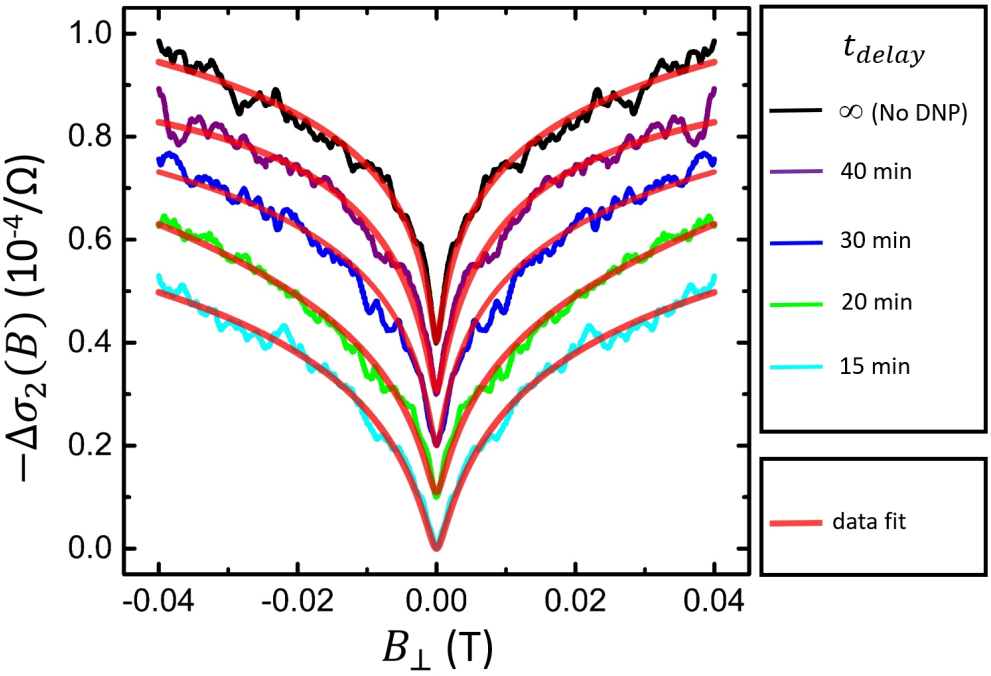

Figure 4.16: 2D conductivity corrections vs $B_\perp$ due to WAL, parametrized in the delay time t_{delay} = 15 min, 20 min, 30 min and 40 min (I_p = 1 mA, t_p = 60 min and T = 0.39 K). The black trace labeled $t_{delay} \to \infty$ denotes a measurement without DNP. The red traces indicate fits to WAL theory.

4.6.4 Dependence on t_{delay}

Experiments were also performed with different delay times t_{delay}, from 15 to 40 min, inserted between removing I_p and performing the WAL measurement, to characterize the decay in B_{OH} and estimate T1. Figure 4.16 contains the antilocalization magnetoresistance as the negative of the 2D conductivity correction $\Delta\sigma_2$ plotted as $-\Delta\sigma_2(B_\perp)$ vs $B_\perp$, with $B_\perp$ the magnetic applied normally to the surface, parameterized in the delay time t_{delay} = 15 min, 20 min, 30 min and 40 min. The data labeled $t_{delay} \to \infty$ denotes a measurement without DNP (returning to a state where nuclear polarization has decayed). The data was obtained at I_p = 1 mA, t_p = 60 min and T = 0.39 K. Best fits to the ILP theory [14] are indicated as red lines and allow for determination of values for τ_{SO} and τ_ϕ.

Figure 4.17(a)-(b) depicts the dependences of τ_{SO} and τ_ϕ on t_{delay} at I_p = 1 mA and t_p = 60 min. With increasing t_{delay}, τ_{SO} decreases and τ_ϕ increases to their values without DNP, consistent with a decay in B_{OH}. In Fig. 4.18, the average B_{OH} decays exponentially with increasing t_{delay}, with spin-lattice relaxation time T1 = 11.4 min. The value T1 = 11.4 min is of the order of expected values [185, 186].

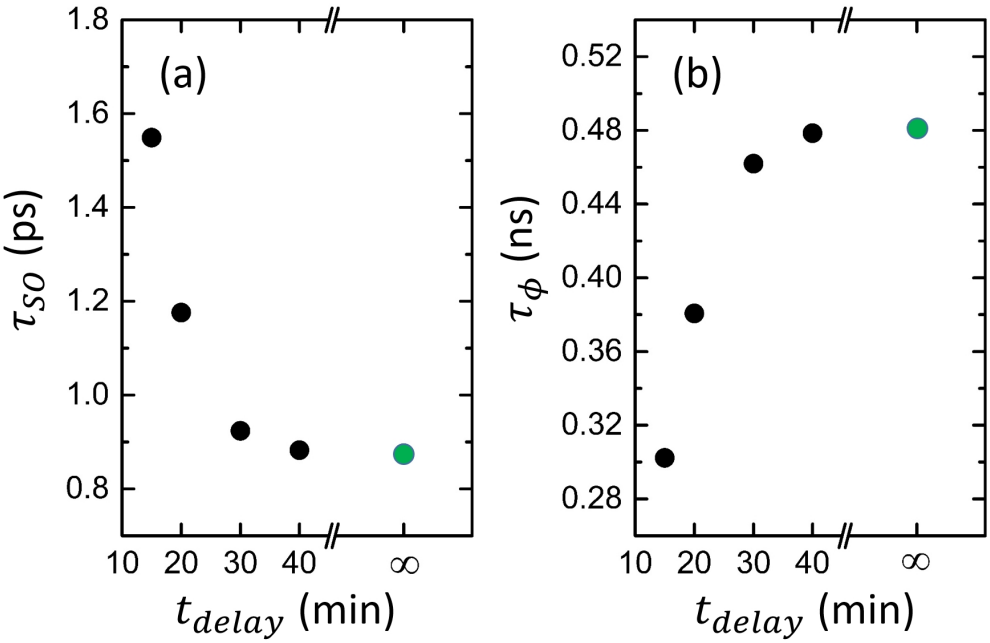

Figure 4.17: (a) Spin-orbit decoherence times τ_{SO} and (b) quantum phase decoherence times τ_{ϕ} at $T = 0.39$ K, $t_p = 60$ min and $I_p = 1$ mA, vs t_{delay}. Data without DNP stand in for $t_{delay} \to \infty$ (green circles).

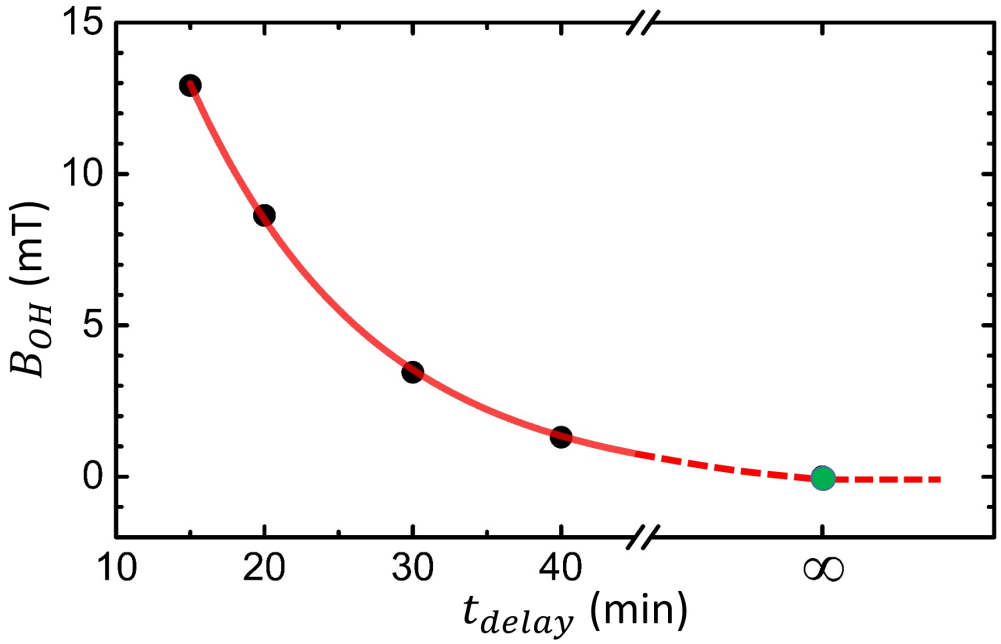

Figure 4.18: Overhauser field B_{OH} at $T = 0.39$ K, $t_p = 60$ min and $I_p = 1$ mA, vs t_{delay}. Data without DNP stand in for $t_{delay} \to \infty$ (green circle). The red line is an exponential fit yielding T1 = 11.4 min.

4.7 Conclusion

In conclusion, Bi(111) thin films were deposited by van der Waals epitaxy on mica substrates. Using antilocalization quantum-coherent transport measurements on the Bi(111) surface states to detect in-plane magnetic fields, quantitative evidence was obtained for a transfer of carrier spin polarization to Bi nuclear spin polarization by hyperfine interaction. The carrier spin polarization was obtained via the Edelstein effect in the Bi(111) surface states.

Through the experiments and theoretical calculations, we concluded that the in-plane magnetic field B_{OH} depends on the average nuclear spin I_{av} after NP, as $B_{OH} = AI_{av}/(g^*_{\parallel}\mu_B)$ [142, 192], and I_{av} follows a Brillouin function in the average carrier spin S_{av} after CP [142]. Using values of $A = 6.1$ μeV to 27 μeV [130, 145, 146, 150] we find that $B_{OH} = 13$ mT is reached for $S_{av} = 0.37$ if $A = 6.1$ μeV and for $S_{av} = 0.20$ if $A = 27$ μeV . Since we do not expect full NP ($S_{av} = \frac{1}{2}$) and B_{OH} involves averages described above, the saturation value of 13 mT is consistent with the knowledge of A in Bi and with plausible values of S_{av}. For $B_{OH} = 13$ mT and in this range of A it is calculated that $B_e \gg B_L$, consistent with the observation of DNP without external magnetic field. Also, the dependence of B_{OH} on I_p strongly resembles the expected Brillouin function, strengthening the consistency between expectations and data. The saturation value $B_{OH} = 13$ mT and the dependences on t_p, t_{delay} and I_p firmly suggest that the CP due to the Edelstein effect was transferred by HI to the Bi nuclei, demonstrating Edelstein-induced DNP and its measurement by quantum transport.

The experiments verify the existence of Edelstein-induced dynamic nuclear polarization, in an example of interaction between spin-orbit interaction and hyperfine interaction via the nuclear spin bath, with possible applications in nuclear spintronics and to polarize nuclei to mitigate spin decoherence via HI in quantum devices. The experiments also show that antilocalization forms a sensitive probe for hyperfine interaction and nuclear polarization.

Chapter 5

Other Published Work

This chapter lists other published work.

5.1 Current-induced Spin–orbit Field in Permalloy Interfaced with Ultrathin Ti and Cu

Abstract [193]: How spin–orbit torques emerge from materials with weak spin–orbit coupling (e.g., light metals) is an open question in spintronics. Here, we report on a field-like spin–orbit torque (i.e., in-plane spin–orbit field transverse to the current axis) in SiO_2-sandwiched Permalloy (Py), with the top Py-SiO_2 interface incorporating ultrathin Ti or Cu. In both SiO_2/Py/Ti/SiO_2 and SiO_2/Py/Cu/SiO_2, this spin–orbit field opposes the classical Oersted field. While the magnitude of the spin–orbit field is at least a factor of 3 greater than the Oersted field, we do not observe evidence for a significant damping-like torque in SiO_2/Py/Ti/SiO_2 or SiO_2/Py/Cu/SiO_2. Our findings point to contributions from a Rashba-Edelstein effect or spin–orbit precession at the (Ti, Cu)-inserted interface.

Our contribution: In this paper we performed a two-layer photolithography process to pattern the samples. The first layer photolithography was carried out by us on a Si(001) wafer, the pattern being depicted in Figure 5.1 in purple. Then after the deposition of SiO_2/Py/Ti/SiO_2 or SiO_2/Py/Cu/SiO_2, a lift-off procedure was performed. We then carried out the second layer photolithography, with a pattern shown in Figure 5.1 in green. The purpose of the second layer is to pattern the contact pads. We deposited Cr/Au on the second layer as contacts, with the Au thickness $\sim$ 100 nm.

5.2 Conductivitylike Gilbert Damping due to Intraband Scattering in Epitaxial Iron

Abstract [194]: Confirming the origin of Gilbert damping by experiment has remained a challenge for many decades, even for simple ferromagnetic metals. Here, we experimentally identify Gilbert damping that increases with decreasing electronic scattering in epitaxial thin films of pure Fe. This observation of conductivitylike damping, which cannot be accounted

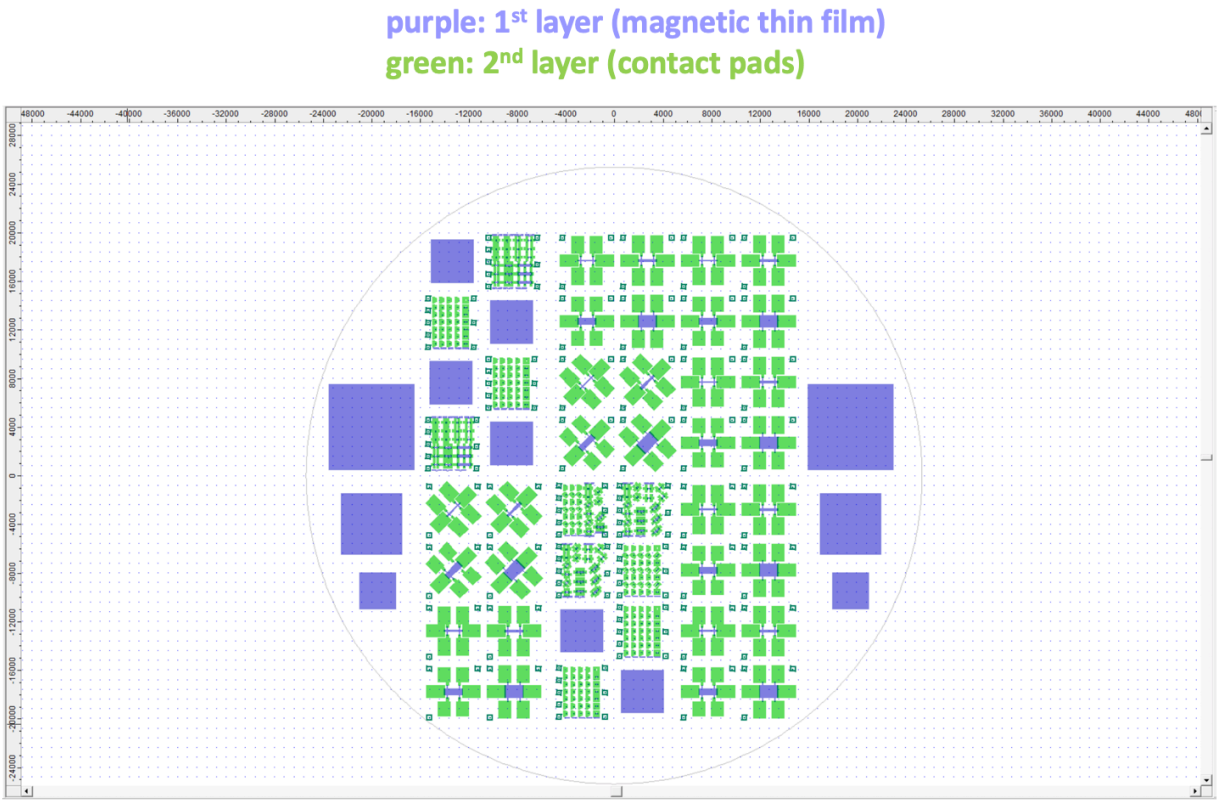

Figure 5.1: Two-layer photolithography pattern. The purple layer is the magnetic thin film layer, the green layer is the contact pads layer.

for by classical eddy-current loss, is in excellent quantitative agreement with theoretical predictions of Gilbert damping due to intraband scattering. Our results resolve the long-standing question about a fundamental damping mechanism and offer hints for engineering lowloss magnetic metals for cryogenic spintronics and quantum devices.

Our contribution: In this paper we performed four-point measurements in a van der Pauw configuration on MAO/Fe and MgO/Fe samples while cooling down from room temperature to about 4 K, from which the electrical resistivity was measured and calculated.

5.3 Magnetic Damping in Epitaxial Iron Alloyed with Vanadium and Aluminum

Abstract [195]: To develop low-moment, low-damping metallic ferromagnets for power-efficient spintronic devices, it is crucial to understand how magnetic relaxation is impacted by the addition of nonmagnetic elements. Here, we compare magnetic relaxation in epitaxial Fe films alloyed with light, nonmagnetic elements of V and Al. Fe-V alloys exhibit lower intrinsic damping compared with that of pure Fe, reduced by nearly a factor of 2, whereas damping in Fe-Al alloys increases with Al content. Our experimental and computational results indicate that reducing the density of states at the Fermi level, rather than the average atomic number, has a more significant impact on lowering damping in Fe alloyed with light elements. Moreover, Fe-V is confirmed to exhibit an intrinsic Gilbert damping parameter of about 0.001, which is among the lowest ever reported for ferromagnetic metals.

Our contribution: In this paper we performed four-point measurements in a van der Pauw configuration on Fe-V and Fe-Al alloys while cooling them down from room temperature to about 4 K, from which the electrical resistivity was measured and calculated.

5.4 Element-Specific Detection of Sub-Nanosecond Spin-Transfer Torque in a Nanomagnet Ensemble

Abstract [196]: Spin currents can exert spin-transfer torques on magnetic systems even in the limit of vanishingly small net magnetization, as recently shown for antiferromagnets. Here, we experimentally show that a spin-transfer torque is operative in a macroscopic ensemble of weakly interacting, randomly magnetized Co nanomagnets. We employ element- and time-resolved X-ray ferromagnetic resonance (XFMR) spectroscopy to directly detect subnanosecond dynamics of the Co nanomagnets, excited into precession with cone angle 0.003° by an oscillating spin current. XFMR measurements reveal that as the net moment of the ensemble decreases, the strength of the spin-transfer torque increases relative to those of magnetic field torques. Our findings point to spin-transfer torque as an effective way to

manipulate the state of nanomagnet ensembles at subnanosecond time scales.

Our contribution: In this paper we performed four-point measurements in a van der Pauw configuration on CoCu and NiFe/Cu/CoCu samples while cooling down from room temperature to about 4 K, from which the electrical resistivity was measured and calculated.

Bibliography

[1] P. Hofmann, "The surfaces of bismuth: Structural and electronic properties," *Progress in Surface Science*, vol. 81, no. 5, pp. 191 – 245, 2006.

[2] A. S. Fedotov, V. G. Shepelevich, I. A. Svito, and V. A. Sivakov, "Temperature dynamics of the electronic structure in dilute bi-sn alloys," *Phys. Rev. B*, vol. 97, p. 075204, Feb 2018.

[3] Y. Ohtsubo, J. Mauchain, J. Faure, E. Papalazarou, M. Marsi, P. Le Fèvre, F. Bertran, A. Taleb-Ibrahimi, and L. Perfetti, "Giant anisotropy of spin-orbit splitting at the bismuth surface," *Phys. Rev. Lett.*, vol. 109, p. 226404, Nov 2012.

[4] S. Hikami, A. I. Larkin, and Y. Nagaoka, "Spin-Orbit Interaction and Magnetoresistance in the Two Dimensional Random System," *Progress of Theoretical Physics*, vol. 63, pp. 707–710, 02 1980.

[5] M. Rudolph and J. J. Heremans, "Spin-orbit interaction and phase coherence in lithographically defined bismuth wires," *Phys. Rev. B*, vol. 83, p. 205410, May 2011.

[6] S.-P. Cho, J. Nakamura, N. Tanaka, and T. Osaka, "Direct observation of au deposition processes on InSb{111}a,b-(2 × 2) surfaces," *Nanotechnology*, vol. 15, pp. S393–S397, apr 2004.

[7] M. Gomoyunova and I. Pronin, "Photoelectron spectroscopy of atomic core levels on the silicon surface: A review," *Technical Physics*, vol. 49, pp. 1249–1279, 10 2004.

[8] T. Nagao, J. T. Sadowski, M. Saito, S. Yaginuma, Y. Fujikawa, T. Kogure, T. Ohno, Y. Hasegawa, S. Hasegawa, and T. Sakurai, "Nanofilm allotrope and phase transformation of ultrathin bi film on Si(111)-7×7," *Phys. Rev. Lett.*, vol. 93, p. 105501, Aug 2004.

[9] A. Koma, "Van der waals epitaxy for highly lattice-mismatched systems," *Journal of Crystal Growth*, vol. 201-202, pp. 236 – 241, 1999.

[10] F. Ostendorf, C. Schmitz, S. Hirth, A. Kühnle, J. Kołodziej, and M. Reichling, "How flat is an air-cleaved mica surface?," *Nanotechnology*, vol. 19 30, p. 305705, 2008.

[11] D. Ma, J. Shi, Q. Ji, K. Chen, J. Yin, Y. Lin, Y. Zhang, M. Liu, Q. Feng, X. Song, X. Guo, J. Zhang, Y. Zhang, and Z. Liu, "A universal etching-free transfer of mos2 films for applications in photodetectors," *Nano Research*, vol. 8, no. 11, pp. 3662–3672, 2015.

[12] X. Ma, Q. Liu, D. Xu, Y. Zhu, S. Kim, Y. Cui, L. Zhong, and M. Liu, "Capillary-force-assisted clean-stamp transfer of two-dimensional materials.," *Nano letters*, vol. 17 11, pp. 6961–6967, 2017.

[13] A. Johansson, J. Henk, and I. Mertig, "Theoretical aspects of the edelstein effect for anisotropic two-dimensional electron gas and topological insulators," *Phys. Rev. B*, vol. 93, p. 195440, May 2016.

[14] S. V. Iordanskii, Y. B. Lyanda-Geller, and G. E. Pikus, "Weak localization in quantum wells with spin-orbit interaction," *ZhETF Pisma Redaktsiiu*, vol. 60, p. 199, Aug. 1994.

[15] V. K. Joshi, "Spintronics: A contemporary review of emerging electronics devices," *Engineering Science and Technology, an International Journal*, vol. 19, no. 3, pp. 1503 – 1513, 2016.

[16] D. Awschalom and M. Flatté, "Challenges for semiconductor spintronics," *Nature Physics*, vol. 3, pp. 153–159, 03 2007.

[17] I. Žutić, J. Fabian, and S. Das Sarma, "Spintronics: Fundamentals and applications," *Rev. Mod. Phys.*, vol. 76, pp. 323–410, Apr 2004.

[18] T. Jungwirth, J. Wunderlich, and K. Olejnik, "Spin hall effect devices," *Nature materials*, vol. 11, pp. 382–90, 04 2012.

[19] Y. Ando, "Topological insulator materials," *Journal of the Physical Society of Japan*, vol. 82, no. 10, p. 102001, 2013.

[20] M. Z. Hasan and C. L. Kane, "Colloquium: Topological insulators," *Rev. Mod. Phys.*, vol. 82, pp. 3045–3067, Nov 2010.

[21] X.-L. Qi and S.-C. Zhang, "Topological insulators and superconductors," *Rev. Mod. Phys.*, vol. 83, pp. 1057–1110, Oct 2011.

[22] J. Sinova, S. O. Valenzuela, J. Wunderlich, C. H. Back, and T. Jungwirth, "Spin hall effects," *Rev. Mod. Phys.*, vol. 87, pp. 1213–1260, Oct 2015.

[23] C.-X. Liu, S.-C. Zhang, and X.-L. Qi, "The quantum anomalous hall effect: Theory and experiment," *Annual Review of Condensed Matter Physics*, vol. 7, no. 1, pp. 301–321, 2016.

[24] M. König, S. Wiedmann, C. Brüne, A. Roth, H. Buhmann, L. W. Molenkamp, X.-L. Qi, and S.-C. Zhang, "Quantum spin hall insulator state in hgte quantum wells," *Science*, vol. 318, no. 5851, pp. 766–770, 2007.

[25] V. Mourik, K. Zuo, S. M. Frolov, S. R. Plissard, E. P. A. M. Bakkers, and L. P. Kouwenhoven, "Signatures of majorana fermions in hybrid superconductor-semiconductor nanowire devices," *Science*, vol. 336, no. 6084, pp. 1003–1007, 2012.

[26] J. D. Sau, S. Tewari, R. M. Lutchyn, T. D. Stanescu, and S. Das Sarma, "Non-abelian quantum order in spin-orbit-coupled semiconductors: Search for topological majorana particles in solid-state systems," *Phys. Rev. B*, vol. 82, p. 214509, Dec 2010.

[27] G. Bihlmayer, O. Rader, and R. Winkler, "Focus on the rashba effect," *New Journal of Physics*, vol. 17, p. 050202, may 2015.

[28] Y. M. Koroteev, G. Bihlmayer, J. E. Gayone, E. V. Chulkov, S. Blügel, P. M. Echenique, and P. Hofmann, "Strong spin-orbit splitting on bi surfaces," *Phys. Rev. Lett.*, vol. 93, p. 046403, Jul 2004.

[29] C. R. Ast, J. Henk, A. Ernst, L. Moreschini, M. C. Falub, D. Pacilé, P. Bruno, K. Kern, and M. Grioni, "Giant spin splitting through surface alloying," *Phys. Rev. Lett.*, vol. 98, p. 186807, May 2007.

[30] J. C. R. Sánchez, L. Vila, G. Desfonds, S. Gambarelli, J. P. Attané, J. M. De Teresa, C. Magén, and A. Fert, "Spin-to-charge conversion using rashba coupling at the interface between non-magnetic materials," *Nature Communications*, vol. 4, no. 1, p. 2944, 2013.

[31] M. Isasa, M. C. Martínez-Velarte, E. Villamor, C. Magén, L. Morellón, J. M. De Teresa, M. R. Ibarra, G. Vignale, E. V. Chulkov, E. E. Krasovskii, L. E. Hueso, and F. Casanova, "Origin of inverse rashba-edelstein effect detected at the cu/bi interface using lateral spin valves," *Phys. Rev. B*, vol. 93, p. 014420, Jan 2016.

[32] L. Li, J. G. Checkelsky, Y. S. Hor, C. Uher, A. F. Hebard, R. J. Cava, and N. P. Ong, "Phase transitions of dirac electrons in bismuth," *Science*, vol. 321, no. 5888, pp. 547–550, 2008.

[33] B. Fauqué, H. Yang, I. Sheikin, L. Balicas, J.-P. Issi, and K. Behnia, "Hall plateaus at magic angles in bismuth beyond the quantum limit," *Phys. Rev. B*, vol. 79, p. 245124, Jun 2009.

[34] Z. Zhu, A. Collaudin, B. Fauqué, W. Kang, and K. Behnia, "Field-induced polarization of dirac valleys in bismuth," *Nature Physics*, vol. 8, no. 1, pp. 89–94, 2012.

[35] A. Takayama, T. Sato, S. Souma, T. Oguchi, and T. Takahashi, "One-dimensional edge states with giant spin splitting in a bismuth thin film," *Phys. Rev. Lett.*, vol. 114, p. 066402, Feb 2015.

[36] N. Kawakami, C.-L. Lin, M. Kawai, R. Arafune, and N. Takagi, "One-dimensional edge state of bi thin film grown on si(111)," *Applied Physics Letters*, vol. 107, no. 3, p. 031602, 2015.

[37] I. K. Drozdov, A. Alexandradinata, S. Jeon, S. Nadj-Perge, H. Ji, R. J. Cava, B. Andrei Bernevig, and A. Yazdani, "One-dimensional topological edge states of bismuth bilayers," *Nature Physics*, vol. 10, no. 9, pp. 664–669, 2014.

[38] Z. F. Wang, L. Chen, and F. Liu, "Tuning topological edge states of bi(111) bilayer film by edge adsorption," *Nano Letters*, vol. 14, pp. 2879–2883, 05 2014.

[39] H. W. Yeom, K.-H. Jin, and S.-H. Jhi, "Topological fate of edge states of single bi bilayer on bi(111)," *Phys. Rev. B*, vol. 93, p. 075435, Feb 2016.

[40] R. R. Q. Freitas, R. Rivelino, F. de Brito Mota, C. M. C. de Castilho, A. Kakanakova-Georgieva, and G. K. Gueorguiev, "Topological insulating phases in two-dimensional bismuth-containing single layers preserved by hydrogenation," *The Journal of Physical Chemistry C*, vol. 119, pp. 23599–23606, 10 2015.

[41] E. Aktürk, O. U. Aktürk, and S. Ciraci, "Single and bilayer bismuthene: Stability at high temperature and mechanical and electronic properties," *Phys. Rev. B*, vol. 94, p. 014115, Jul 2016.

[42] S. Zhang, M. Xie, F. Li, Z. Yan, Y. Li, E. Kan, W. Liu, Z. Chen, and H. Zeng, "Semiconducting group 15 monolayers: A broad range of band gaps and high carrier mobilities," *Angewandte Chemie International Edition*, vol. 55, no. 5, pp. 1666–1669, 2016.

[43] M. Rudolph and J. J. Heremans, "Electronic and quantum phase coherence properties of bismuth thin films," *Applied Physics Letters*, vol. 100, no. 24, p. 241601, 2012.

[44] T. Hirahara, T. Nagao, I. Matsuda, G. Bihlmayer, E. V. Chulkov, Y. M. Koroteev, P. M. Echenique, M. Saito, and S. Hasegawa, "Role of spin-orbit coupling and hybridization effects in the electronic structure of ultrathin bi films," *Phys. Rev. Lett.*, vol. 97, p. 146803, Oct 2006.

[45] J. P. Michenaud and J. P. Issi, "Electron and hole transport in bismuth," *Journal of Physics C: Solid State Physics*, vol. 5, pp. 3061–3072, oct 1972.

[46] N. Garcia, Y. H. Kao, and M. Strongin, "Galvanomagnetic studies of bismuth films in the quantum-size-effect region," *Phys. Rev. B*, vol. 5, pp. 2029–2039, Mar 1972.

[47] C. A. Hoffman, J. R. Meyer, F. J. Bartoli, A. Di Venere, X. J. Yi, C. L. Hou, H. C. Wang, J. B. Ketterson, and G. K. Wong, "Semimetal-to-semiconductor transition in bismuth thin films," *Phys. Rev. B*, vol. 48, pp. 11431–11434, Oct 1993.

[48] M. P. Vecchi, J. R. Pereira, and M. S. Dresselhaus, "Anomalies in the magnetoreflection spectrum of bismuth in the low-quantum-number limit," *Phys. Rev. B*, vol. 14, pp. 298–317, Jul 1976.

[49] V. S. Tsoi, "Focusing of electrons by a transverse magnetic field," *JETP Letters*, vol. 19, pp. 114–116, 01 1974.

[50] R. Hartman, "Temperature dependence of the low-field galvanomagnetic coefficients of bismuth," *Phys. Rev.*, vol. 181, pp. 1070–1086, May 1969.

[51] Y. Hasegawa, M. Murata, D. Nakamura, T. Komine, T. Taguchi, and S. Nakamura, "Mobility estimation in microsized bismuth wire arrays," *Journal of Applied Physics*, vol. 105, no. 10, p. 103715, 2009.

[52] A. Nikolaeva, D. Gitsu, L. Konopko, M. J. Graf, and T. E. Huber, "Quantum interference of surface states in bismuth nanowires probed by the aharonov-bohm oscillatory behavior of the magnetoresistance," *Phys. Rev. B*, vol. 77, p. 075332, Feb 2008.

[53] T. E. Huber, A. Nikolaeva, L. Konopko, and M. J. Graf, "Observation of three-dimensional behavior in surface states of bismuth nanowires and the evidence for bulk-bi surface quasiparticles," *Phys. Rev. B*, vol. 79, p. 201304, May 2009.

[54] T. E. Huber, A. Adeyeye, A. Nikolaeva, L. Konopko, R. C. Johnson, and M. J. Graf, "Surface state band mobility and thermopower in semiconducting bismuth nanowires," *Phys. Rev. B*, vol. 83, p. 235414, Jun 2011.

[55] B. Hackens, J. P. Minet, S. Faniel, G. Farhi, C. Gustin, J. P. Issi, J. P. Heremans, and V. Bayot, "Quantum transport, anomalous dephasing, and spin-orbit coupling in an open ballistic bismuth nanocavity," *Phys. Rev. B*, vol. 67, p. 121403, Mar 2003.

[56] B. Hackens, J. Minet, G. Farhi, G. Faniel, C. Gustin, and V. Bayot, "Weak antilocalization and ucfs in an open bismuth quantum dot," *Physica E: Low-dimensional Systems and Nanostructures*, vol. 17, pp. 156–158, 04 2003.

[57] C. R. Ast and H. Höchst, "Fermi surface of bi(111) measured by photoemission spectroscopy," *Phys. Rev. Lett.*, vol. 87, p. 177602, Oct 2001.

[58] T. Hirahara, K. Miyamoto, I. Matsuda, T. Kadono, A. Kimura, T. Nagao, G. Bihlmayer, E. V. Chulkov, S. Qiao, K. Shimada, H. Namatame, M. Taniguchi, and S. Hasegawa, "Direct observation of spin splitting in bismuth surface states," *Phys. Rev. B*, vol. 76, p. 153305, Oct 2007.

[59] N. Marcano, S. Sangiao, C. Magén, L. Morellón, M. R. Ibarra, M. Plaza, L. Pérez, and J. M. De Teresa, "Role of the surface states in the magnetotransport properties of ultrathin bismuth films," *Phys. Rev. B*, vol. 82, p. 125326, Sep 2010.

[60] C. R. Ast and H. Höchst, "Indication of charge-density-wave formation in bi(111)," *Phys. Rev. Lett.*, vol. 90, p. 016403, Jan 2003.

[61] Y. A. Bychkov and E. I. Rashba, "Oscillatory effects and the magnetic susceptibility of carriers in inversion layers," *Journal of Physics C: Solid State Physics*, vol. 17, pp. 6039–6045, nov 1984.

[62] A. Manchon, H. C. Koo, J. Nitta, S. M. Frolov, and R. A. Duine, "New perspectives for rashba spin–orbit coupling," *Nature Materials*, vol. 14, no. 9, pp. 871–882, 2015.

[63] M. Kohda, T. Bergsten, and J. Nitta, "Manipulating spin–orbit interaction in semiconductors," *Journal of the Physical Society of Japan*, vol. 77, no. 3, p. 031008, 2008.

[64] M. Cardona, N. E. Christensen, and G. Fasol, "Relativistic band structure and spin-orbit splitting of zinc-blende-type semiconductors," *Phys. Rev. B*, vol. 38, pp. 1806–1827, Jul 1988.

[65] J. C. R. Sánchez, L. Vila, G. Desfonds, S. Gambarelli, J. P. Attané, J. M. De Teresa, C. Magén, and A. Fert, "Spin-to-charge conversion using rashba coupling at the interface between non-magnetic materials," *Nature Communications*, vol. 4, no. 1, p. 2944, 2013.

[66] Y. M. Koroteev, G. Bihlmayer, E. V. Chulkov, and S. Blügel, "First-principles investigation of structural and electronic properties of ultrathin bi films," *Phys. Rev. B*, vol. 77, p. 045428, Jan 2008.

[67] A. Kimura, E. E. Krasovskii, R. Nishimura, K. Miyamoto, T. Kadono, K. Kanomaru, E. V. Chulkov, G. Bihlmayer, K. Shimada, H. Namatame, and M. Taniguchi, "Strong rashba-type spin polarization of the photocurrent from bulk continuum states: Experiment and theory for bi(111)," *Phys. Rev. Lett.*, vol. 105, p. 076804, Aug 2010.

[68] A. Takayama, T. Sato, S. Souma, and T. Takahashi, "Giant out-of-plane spin component and the asymmetry of spin polarization in surface rashba states of bismuth thin film," *Phys. Rev. Lett.*, vol. 106, p. 166401, Apr 2011.

[69] G. Dresselhaus, "Spin-orbit coupling effects in zinc blende structures," *Phys. Rev.*, vol. 100, pp. 580–586, Oct 1955.

[70] R. L. Kallaher, J. J. Heremans, N. Goel, S. J. Chung, and M. B. Santos, "Spin-orbit interaction determined by antilocalization in an insb quantum well," *Phys. Rev. B*, vol. 81, p. 075303, Feb 2010.

[71] H. Chen, J. J. Heremans, J. A. Peters, A. O. Govorov, N. Goel, S. J. Chung, and M. B. Santos, "Spin-polarized reflection in a two-dimensional electron system," *Applied Physics Letters*, vol. 86, no. 3, p. 032113, 2005.

[72] H. Chen, J. Peters, Y. Pan, J. Heremans, N. Goel, S. Chung, B. Santos, W. Roy, and G. Borghs, "Mesoscopic spin-dependent reflection experiments on insb- and inas-based heterostructures," *Physica E-low-dimensional Systems Nanostructures - PHYSICA E*, vol. 34, pp. 374–376, 08 2006.

[73] R. Lillianfeld, R. Kallaher, J. Heremans, H. Chen, N. Goel, S. Chung, M. Santos, W. Van Roy, and G. Borghs, "Oscillatory quantum interference effects in narrow-gap semiconductor heterostructures," *Physics Procedia*, vol. 3, no. 2, pp. 1231 – 1236, 2010. Proceedings of the 14th International conference on Narrow Gap Semiconductors and Systems.

[74] B. Shojaei, P. J. J. O'Malley, J. Shabani, P. Roushan, B. D. Schultz, R. M. Lutchyn, C. Nayak, J. M. Martinis, and C. J. Palmstrøm, "Demonstration of gate control of spin splitting in a high-mobility inas/alsb two-dimensional electron gas," *Phys. Rev. B*, vol. 93, p. 075302, Feb 2016.

[75] R. L. Kallaher, J. J. Heremans, W. Van Roy, and G. Borghs, "Spin and phase coherence lengths in inas wires with diffusive boundary scattering," *Phys. Rev. B*, vol. 88, p. 205407, Nov 2013.

[76] R. L. Kallaher and J. J. Heremans, "Spin and phase coherence measured by antilocalization in n-InSb thin films," *Phys. Rev. B*, vol. 79, p. 075322, Feb 2009.

[77] R. L. Kallaher, J. J. Heremans, N. Goel, S. J. Chung, and M. B. Santos, "Spin and phase coherence lengths in n-InSb quasi-one-dimensional wires," *Phys. Rev. B*, vol. 81, p. 035335, Jan 2010.

[78] Y. Zhang, R. L. Kallaher, V. Soghomonian, and J. J. Heremans, "Measurement by antilocalization of interactions between inas surface electrons and magnetic surface species," *Phys. Rev. B*, vol. 87, p. 054430, Feb 2013.

[79] Y. Zhang and J. Heremans, "Effects of ferromagnetic nanopillars on spin coherence in an ingaas quantum well," *Solid State Communications*, vol. 177, pp. 36 – 41, 2014.

[80] J. J. Heremans, Y. Xie, S. L. Ren, C. L. Priol, and M. B. Santos, "Mapping electromagnetic dualities via quantum decoherence measurements in 2D materials," in *Carbon Nanotubes, Graphene, and Emerging 2D Materials for Electronic and Photonic Devices IX* (M. Razeghi, M. Ghazinejad, C. Bayram, and J. S. Yu, eds.), vol. 9932, pp. 9 – 19, International Society for Optics and Photonics, SPIE, 2016.

[81] J. J. Heremans, R. L. Kallaher, M. Rudolph, and M. B. Santos, "Magnetoelectric mapping as observed in quantum coherence phenomena under strong spin-orbit interaction," *Integrated Ferroelectrics*, vol. 166, no. 1, pp. 10–16, 2015.

[82] V. Deo, Y. Zhang, V. Soghomonian, and J. J. Heremans, "Quantum interference measurement of spin interactions in a bio-organic/semiconductor device structure," *Scientific Reports*, vol. 5, no. 1, p. 9487, 2015.

[83] G. Bergmann, "Weak localization in thin films: a time-of-flight experiment with conduction electrons," *Physics Reports*, vol. 107, no. 1, pp. 1 – 58, 1984.

[84] G. Bergmann, "Weak localization and its applications as an experimental tool," *International Journal of Modern Physics B*, vol. 24, no. 12n13, pp. 2015–2052, 2010.

[85] J. J. Lin and J. P. Bird, "Recent experimental studies of electron dephasing in metal and semiconductor mesoscopic structures," *Journal of Physics: Condensed Matter*, vol. 14, pp. R501–R596, apr 2002.

[86] Y. Xie, C. L. Priol, and J. J. Heremans, "Geometrical dependence of quantum decoherence in circular arenas with side-wires," *Journal of Physics: Condensed Matter*, vol. 28, p. 495003, oct 2016.

[87] C. Texier, P. Delplace, and G. Montambaux, "Quantum oscillations and decoherence due to electron-electron interaction in metallic networks and hollow cylinders," *Phys. Rev. B*, vol. 80, p. 205413, Nov 2009.

[88] M. Ferrier, A. C. H. Rowe, S. Guéron, H. Bouchiat, C. Texier, and G. Montambaux, "Geometrical dependence of decoherence by electronic interactions in a GaAs/GaAlAs square network," *Phys. Rev. Lett.*, vol. 100, p. 146802, Apr 2008.

[89] C. Texier and G. Montambaux, "Dephasing due to electron-electron interaction in a diffusive ring," *Phys. Rev. B*, vol. 72, p. 115327, Sep 2005.

[90] T. Capron, C. Texier, G. Montambaux, D. Mailly, A. D. Wieck, and L. Saminadayar, "Ergodic versus diffusive decoherence in mesoscopic devices," *Phys. Rev. B*, vol. 87, p. 041307, Jan 2013.

[91] Z. Jiang, V. Soghomonian, and J. J. Heremans, "Dynamic nuclear spin polarization induced by the edelstein effect at bi(111) surfaces," *Phys. Rev. Lett.*, vol. 125, p. 106802, Sep 2020.

[92] F. Song, J. W. Wells, Z. Jiang, M. Saxegaard, and E. Wahlström, "Low-temperature growth of bismuth thin films with (111) facet on highly oriented pyrolytic graphite," *ACS Applied Materials & Interfaces*, vol. 7, pp. 8525–8532, 04 2015.

[93] K. Wan, T. Guo, W. Ford, and J. Hermanson, "Low-energy electron diffraction studies of si(111)-($\sqrt{3} \times \sqrt{3}$)r30°-bi system: Observation and structural determination of two phases," *Surface Science*, vol. 261, no. 1, pp. 69 – 87, 1992.

[94] S. Yaginuma, T. NAGAO, J. Sadowski, A. Pucci, Y. Fujikawa, and T. Sakurai, "Surface pre-melting and surface flattening of bi nanofilms on si(1 1 1)-7 × 7," *Surface Science*, vol. 547, p. L877, 12 2003.

[95] Z. Yang, Z. Wu, Y. Lyu, and J. Hao, "Centimeter-scale growth of two-dimensional layered high-mobility bismuth films by pulsed laser deposition," *InfoMat*, vol. 1, no. 1, pp. 98–107, 2019.

[96] P. Fei, Y. Shu-Li, X. Liang, and C. Dong-Min, "Anomalous magneto-transport properties of epitaxial single-crystal bi films on si(111)," *Chinese Physics Letters*, vol. 27, p. 107102, 10 2010.

[97] S. Xiao, D. Wei, and X. Jin, "Bi(111) thin film with insulating interior but metallic surfaces," *Phys. Rev. Lett.*, vol. 109, p. 166805, Oct 2012.

[98] K. Zhu, L. Wu, X. Gong, S. Xiao, and X. Jin, "Quantum transport in the surface states of epitaxial bi(111) thin films," *Phys. Rev. B*, vol. 94, p. 121401, Sep 2016.

[99] H. J. Osten, J. Klatt, and G. Lippert, "Van der waals epitaxy of thick sb, ge, and ge/sb films on mica," *Applied Physics Letters*, vol. 60, no. 1, pp. 44–46, 1992.

[100] P. Kraus, A. Tamtögl, M. Mayrhofer-Reinhartshuber, F. Apolloner, C. Gösweiner, S. Miret-Artés, and W. E. Ernst, "Surface structure of bi(111) from helium atom scattering measurements. inelastic close-coupling formalism," *The Journal of Physical Chemistry C*, vol. 119, pp. 17235–17242, 07 2015.

[101] T. D. Golding, J. A. Dura, H. Wang, J. T. Zborowski, A. Vigliante, H. C. Chen, J. H. Miller, and J. R. Meyer, "Investigation of sb/GaSb multilayer structures for potential application as an indirect narrow-bandgap material," *Semiconductor Science and Technology*, vol. 8, pp. S117–S120, jan 1993.

[102] P. Fantini, S. Gardonio, P. Barbieri, U. del Pennino, C. Mariani, M. Grazia Betti, E. Magnano, M. Pivetta, and M. Sancrotti, " -sn pseudomorphic growth on insb (111) and (111) surfaces: a high-resolution photoemission study," *Surface Science*, vol. 463, no. 3, pp. 174 – 182, 2000.

[103] S. Cho, Y.-H. Um, Y. Kim, G. K. L. Wong, J. B. Ketterson, and J.-I. Hong, "Bi epitaxy on polar insb(111)a/b faces," *Journal of Vacuum Science & Technology A*, vol. 20, no. 4, pp. 1191–1194, 2002.

[104] M. Kammler and M. Horn-von Hoegen, "Low energy electron diffraction of epitaxial growth of bismuth on si(111)," *Surface Science*, vol. 576, pp. 56–60, 02 2005.

[105] T. Payer, C. Klein, M. Acet, V. Ney, M. Kammler, F.-J. Meyer zu Heringdorf, and M. Horn-von Hoegen, "High-quality epitaxial bi(111) films on si(111) by isochronal annealing," *Thin Solid Films*, vol. 520, no. 23, pp. 6905 – 6908, 2012.

[106] T. Tono, T. Hirahara, and S. Hasegawa, "In situtransport measurements on ultrathin bi(111) films using a magnetic tip: possible detection of current-induced spin polarization in the surface states," *New Journal of Physics*, vol. 15, p. 105018, oct 2013.

[107] A. Koma, K. Sunouchi, and T. Miyajima, "Fabrication and characterization of heterostructures with subnanometer thickness," *Microelectronic Engineering*, vol. 2, no. 1, pp. 129 – 136, 1984. Special Issue on Nanometer Structure Electronics.

[108] A. Koma, K. Sunouchi, and T. Miyajima, "Summary abstract: Fabrication of ultrathin heterostructures with van der waals epitaxy," *Journal of Vacuum Science & Technology B: Microelectronics Processing and Phenomena*, vol. 3, no. 2, pp. 724–724, 1985.

[109] A. Koma, K. Saiki, and Y. Sato, "Heteroepitaxy of a two-dimensional material on a three-dimensional material," *Applied Surface Science*, vol. 41-42, pp. 451 – 456, 1990.

[110] K. Ueno, T. Shimada, K. Saiki, and A. Koma, "Heteroepitaxial growth of layered transition metal dichalcogenides on sulfur-terminated gaas111 surfaces," *Applied Physics Letters*, vol. 56, no. 4, pp. 327–329, 1990.

[111] K. Ueno, K. Saiki, T. Shimada, and A. Koma, "Epitaxial growth of transition metal dichalcogenides on cleaved faces of mica," *Journal of Vacuum Science & Technology A*, vol. 8, no. 1, pp. 68–72, 1990.

[112] F. S. Ohuchi, B. A. Parkinson, K. Ueno, and A. Koma, "van der waals epitaxial growth and characterization of mose2 thin films on sns2," *Journal of Applied Physics*, vol. 68, no. 5, pp. 2168–2175, 1990.

[113] L. A. Walsh and C. L. Hinkle, "van der waals epitaxy: 2d materials and topological insulators," *Applied Materials Today*, vol. 9, pp. 504 – 515, 2017.

[114] A. J. Littlejohn, Y. Xiang, E. Rauch, T.-M. Lu, and G.-C. Wang, "van der waals epitaxy of ge films on mica," *Journal of Applied Physics*, vol. 122, no. 18, p. 185305, 2017.

[115] M.-Y. Yao, F. Zhu, C. Q. Han, D. D. Guan, C. Liu, D. Qian, and J.-f. Jia, "Topologically nontrivial bismuth(111) thin films," *Scientific Reports*, vol. 6, no. 1, p. 21326, 2016.

[116] F. Y. Yang, K. Liu, K. Hong, D. H. Reich, P. C. Searson, and C. L. Chien, "Large magnetoresistance of electrodeposited single-crystal bismuth thin films," *Science*, vol. 284, no. 5418, pp. 1335–1337, 1999.

[117] F. Pang, X. Liang, Z. Liao, S. Yin, and D. Chen, "Origin of the metallic to insulating transition of an epitaxial bi(111) film grown on si(111)," *Chinese Physics B*, vol. 19, p. 087201, 05 2010.

[118] R. Hartman, "Temperature dependence of the low-field galvanomagnetic coefficients of bismuth," *Phys. Rev.*, vol. 181, pp. 1070–1086, May 1969.

[119] R. N. Zitter, "Small-field galvanomagnetic tensor of bismuth at 4.2°k," *Phys. Rev.*, vol. 127, pp. 1471–1480, Sep 1962.

[120] H. Chu and W. Zhang, "Quantum size effect and electric conductivity in thin films of pure bismuth," *Journal of Physics and Chemistry of Solids*, vol. 53, no. 8, pp. 1059 – 1065, 1992.

[121] V. B. Sandomirskiĭ, "Quantum Size Effect in a Semimetal Film," *Soviet Journal of Experimental and Theoretical Physics*, vol. 25, p. 101, July 1967.

[122] S. A. Solin, T. Thio, D. R. Hines, and J. J. Heremans, "Enhanced room-temperature geometric magnetoresistance in inhomogeneous narrow-gap semiconductors," *Science*, vol. 289, no. 5484, pp. 1530–1532, 2000.

[123] T. Arisaka, M. Otsuka, and Y. Hasegawa, "Investigation of carrier scattering process in polycrystalline bulk bismuth at 300 k," *Journal of Applied Physics*, vol. 123, no. 23, p. 235107, 2018.

[124] A. G. Mal'shukov, K. A. Chao, and M. Willander, "Magnetoresistance of a weakly disordered iii-v semiconductor quantum well in a magnetic field parallel to interfaces," *Phys. Rev. B*, vol. 56, pp. 6436–6439, Sep 1997.

[125] F. E. Meijer, A. F. Morpurgo, T. M. Klapwijk, T. Koga, and J. Nitta, "Competition between spin-orbit interaction and zeeman coupling in rashba two-dimensional electron gases," *Phys. Rev. B*, vol. 70, p. 201307, Nov 2004.

[126] F. Martins, F. K. Malinowski, P. D. Nissen, E. Barnes, S. Fallahi, G. C. Gardner, M. J. Manfra, C. M. Marcus, and F. Kuemmeth, "Noise suppression using symmetric exchange gates in spin qubits," *Phys. Rev. Lett.*, vol. 116, p. 116801, Mar 2016.

[127] E. Barnes and S. E. Economou, "Electron-nuclear dynamics in a quantum dot under nonunitary electron control," *Phys. Rev. Lett.*, vol. 107, p. 047601, Jul 2011.

[128] S. E. Economou and E. Barnes, "Theory of dynamic nuclear polarization and feedback in quantum dots," *Phys. Rev. B*, vol. 89, p. 165301, Apr 2014.

[129] A. Del Maestro, T. Hyart, and B. Rosenow, "Backscattering between helical edge states via dynamic nuclear polarization," *Phys. Rev. B*, vol. 87, p. 165440, Apr 2013.

[130] D. M. Nisson, A. P. Dioguardi, P. Klavins, C. H. Lin, K. Shirer, A. C. Shockley, J. Crocker, and N. J. Curro, "Nuclear magnetic resonance as a probe of electronic states of bi_2se_3," *Phys. Rev. B*, vol. 87, p. 195202, May 2013.

[131] V. Edelstein, "Spin polarization of conduction electrons induced by electric current in two-dimensional asymmetric electron systems," *Solid State Communications*, vol. 73, no. 3, pp. 233 – 235, 1990.

[132] J. Borge, C. Gorini, G. Vignale, and R. Raimondi, "Spin hall and edelstein effects in metallic films: From two to three dimensions," *Phys. Rev. B*, vol. 89, p. 245443, Jun 2014.

[133] K. Shen, G. Vignale, and R. Raimondi, "Microscopic theory of the inverse edelstein effect," *Phys. Rev. Lett.*, vol. 112, p. 096601, Mar 2014.

[134] D. Pesin and A. H. MacDonald, "Spintronics and pseudospintronics in graphene and topological insulators," *Nature Materials*, vol. 11, no. 5, pp. 409–416, 2012.

[135] E. L. Ivchenko, Y. B. Lyanda-Geller, and G. E. Pikus, "Photocurrent in structures with quantum wells with an optical orientation of free carriers," *Soviet Journal of Experimental and Theoretical Physics Letters*, vol. 50, p. 175, Aug. 1989.

[136] S. Emori, T. Nan, A. M. Belkessam, X. Wang, A. D. Matyushov, C. J. Babroski, Y. Gao, H. Lin, and N. X. Sun, "Interfacial spin-orbit torque without bulk spin-orbit coupling," *Phys. Rev. B*, vol. 93, p. 180402, May 2016.

[137] A. G. Aronov and Y. B. Lyanda-Geller, "Nuclear electric resonance and orientation of carrier spins by an electric field," *Soviet Journal of Experimental and Theoretical Physics Letters*, vol. 50, p. 431, Nov. 1989.

[138] M. Johnson, "Dynamic nuclear polarization by spin injection," vol. 77, no. 11, pp. 1680–1682, 2000.

[139] G. Salis, A. Fuhrer, and S. F. Alvarado, "Signatures of dynamically polarized nuclear spins in all-electrical lateral spin transport devices," *Phys. Rev. B*, vol. 80, p. 115332, Sep 2009.

[140] C. J. Trowbridge, B. M. Norman, Y. K. Kato, D. D. Awschalom, and V. Sih, "Dynamic nuclear polarization from current-induced electron spin polarization," *Phys. Rev. B*, vol. 90, p. 085122, Aug 2014.

[141] D. Paget, G. Lampel, B. Sapoval, and V. I. Safarov, "Low field electron-nuclear spin coupling in gallium arsenide under optical pumping conditions," *Phys. Rev. B*, vol. 15, pp. 5780–5796, Jun 1977.

[142] F. Meier and B. P. Zakharchenya, *Optical Orientation*. North Holland, 1984.

[143] I. Ţifrea and M. E. Flatté, "Nonequilibrium nuclear polarization and induced hyperfine and dipolar magnetic fields in semiconductor nanostructures," *Phys. Rev. B*, vol. 84, p. 155319, Oct 2011.

[144] S. A. Tarasenko and G. Burkard, "Limitation of electron mobility from hyperfine interaction in ultraclean quantum wells and topological insulators," *Phys. Rev. B*, vol. 94, p. 045309, Jul 2016.

[145] R. E. George, W. Witzel, H. Riemann, N. V. Abrosimov, N. Nötzel, M. L. W. Thewalt, and J. J. L. Morton, "Electron spin coherence and electron nuclear double resonance of bi donors in natural si," *Phys. Rev. Lett.*, vol. 105, p. 067601, Aug 2010.

[146] G. W. Morley, M. Warner, A. M. Stoneham, P. T. Greenland, J. van Tol, C. W. M. Kay, and G. Aeppli, "The initialization and manipulation of quantum information stored in silicon by bismuth dopants," *Nature Materials*, vol. 9, no. 9, pp. 725–729, 2010.

[147] P. A. Mortemousque, S. Berger, T. Sekiguchi, C. Culan, R. G. Elliman, and K. M. Itoh, "Hyperfine clock transitions of bismuth donors in silicon detected by spin-dependent recombination," *Phys. Rev. B*, vol. 89, p. 155202, Apr 2014.

[148] J. Schliemann, A. Khaetskii, and D. Loss, "Electron spin dynamics in quantum dots and related nanostructures due to hyperfine interaction with nuclei," *Journal of Physics: Condensed Matter*, vol. 15, pp. R1809–R1833, dec 2003.

[149] S. Mukhopadhyay, S. Krämer, H. Mayaffre, H. F. Legg, M. Orlita, C. Berthier, M. Horvatić, G. Martinez, M. Potemski, B. A. Piot, A. Materna, G. Strzelecka, and A. Hruban, "Hyperfine coupling and spin polarization in the bulk of the topological insulator bi_2se_3," *Phys. Rev. B*, vol. 91, p. 081105, Feb 2015.

[150] G. Feher, "Electron spin resonance experiments on donors in silicon. i. electronic structure of donors by the electron nuclear double resonance technique," *Phys. Rev.*, vol. 114, pp. 1219–1244, Jun 1959.

[151] E. Fermi, "Über die magnetischen momente der atomkerne," *Zeitschrift für Physik*, vol. 60, no. 5, pp. 320–333, 1930.

[152] V. Tripathi, A. C. H. Cheung, and N. R. Cooper, "Dynamic nuclear polarisation in biased quantum wires with spin-orbit interaction," *EPL (Europhysics Letters)*, vol. 81, p. 68001, feb 2008.

[153] B. F. Williams and R. R. Hewitt, "Nuclear magnetic resonance in bismuth metal," *Phys. Rev.*, vol. 146, pp. 286–290, Jun 1966.

[154] H. Hamaed, M. W. Laschuk, V. V. Terskikh, and R. W. Schurko, "Application of solid-state 209bi nmr to the structural characterization of bismuth-containing materials," *Journal of the American Chemical Society*, vol. 131, pp. 8271–8279, 06 2009.

[155] L. Petersen and P. Hedegård, "A simple tight-binding model of spin–orbit splitting of sp-derived surface states," *Surface Science*, vol. 459, no. 1, pp. 49 – 56, 2000.

[156] R. E. Taylor, B. Leung, M. P. Lake, and L.-S. Bouchard, "Spin–lattice relaxation in bismuth chalcogenides," *The Journal of Physical Chemistry C*, vol. 116, pp. 17300–17305, 08 2012.

[157] D. Koumoulis, B. Leung, T. Chasapis, R. Taylor, D. King, M. Kanatzidis, and L. Bouchard, "Understanding bulk defects in topological insulators from nuclear-spin interactions," *Advanced Functional Materials*, vol. 24, pp. 1519–1528, Mar. 2014.

[158] K. Saeedi, M. Szech, P. Dluhy, J. Z. Salvail, K. J. Morse, H. Riemann, N. V. Abrosimov, N. Nötzel, K. L. Litvinenko, B. N. Murdin, and M. L. W. Thewalt, "Optical pumping and readout of bismuth hyperfine states in silicon for atomic clock applications," *Scientific Reports*, vol. 5, no. 1, p. 10493, 2015.

[159] J. M. Nichol, S. P. Harvey, M. D. Shulman, A. Pal, V. Umansky, E. I. Rashba, B. I. Halperin, and A. Yacoby, "Quenching of dynamic nuclear polarization by spin–orbit coupling in gaas quantum dots," *Nature Communications*, vol. 6, no. 1, p. 7682, 2015.

[160] K. Hashimoto, K. Muraki, N. Kumada, T. Saku, and Y. Hirayama, "Effects of inversion asymmetry on electron-nuclear spin coupling in semiconductor heterostructures: Possible role of spin-orbit interactions," *Physical review letters*, vol. 94, p. 146601, 05 2005.

[161] J. A. Nesteroff, Y. V. Pershin, and V. Privman, "Polarization of nuclear spins from the conductance of quantum wire," *Phys. Rev. Lett.*, vol. 93, p. 126601, Sep 2004.

[162] A. M. Lunde and G. Platero, "Hyperfine interactions in two-dimensional hgte topological insulators," *Phys. Rev. B*, vol. 88, p. 115411, Sep 2013.

[163] Y. Hirayama, G. Yusa, K. Hashimoto, N. Kumada, T. Ota, and K. Muraki, "Electron-spin/nuclear-spin interactions and nmr in semiconductors," *Semiconductor Science and Technology*, vol. 24, p. 023001, 01 2009.

[164] G. Yusa, K. Muraki, K. Takashina, K. Hashimoto, and Y. Hirayama, "Controlled multiple quantum coherence of nuclear spins in a nanometre-scale device," *Nature*, vol. 434, pp. 1001–5, 05 2005.

[165] A. Córcoles, C. Ford, M. Pepper, G. Jones, H. Beere, and D. Ritchie, "Nuclear spin coherence in a quantum wire," *Physical Review B*, vol. 80, 06 2009.

[166] Z. Keane, M. Godfrey, J. Chen, S. Fricke, O. Klochan, A. Burke, A. Micolich, H. Beere, D. Ritchie, K. Trunov, D. Reuter, A. Wieck, and A. Hamilton, "Resistively detected nuclear magnetic resonance in n- and p-type gaas quantum point contacts," *Nano letters*, vol. 11, pp. 3147–50, 06 2011.

[167] W. Clark and G. Feher, "Nuclear polarization in insb by a dc current," *Physical Review Letters - PHYS REV LETT*, vol. 12, pp. 717–717, 06 1964.

[168] A. Karabanov, D. Wiśniewski, I. Lesanovsky, and W. Köckenberger, "Dynamic nuclear polarization as kinetically constrained diffusion," *Phys. Rev. Lett.*, vol. 115, p. 020404, Jul 2015.

[169] A. Aronov and Y. Lyanda-Geller, "Nuclear electric resonance and orientation of carrier spins by an electric field," *Jetp Letters - JETP LETT-ENGL TR*, vol. 50, 01 1989.

[170] G. Vignale and I. V. Tokatly, "Theory of the nonlinear rashba-edelstein effect: The clean electron gas limit," *Phys. Rev. B*, vol. 93, p. 035310, Jan 2016.

[171] F. Mahfouzi, N. Nagaosa, and B. K. Nikolić, "Spin-to-charge conversion in lateral and vertical topological-insulator/ferromagnet heterostructures with microwave-driven precessing magnetization," *Phys. Rev. B*, vol. 90, p. 115432, Sep 2014.

[172] Q. Shao, G. Yu, Y.-W. Lan, Y. Shi, M.-Y. Li, C. Zheng, X. Zhu, L.-J. Li, P. K. Amiri, and K. L. Wang, "Strong rashba-edelstein effect-induced spin–orbit torques in monolayer transition metal dichalcogenide/ferromagnet bilayers," *Nano Letters*, vol. 16, pp. 7514–7520, 12 2016.

[173] E. Lesne, Y. Fu, S. Oyarzun, J. C. Rojas-Sánchez, D. C. Vaz, H. Naganuma, G. Sicoli, J. P. Attané, M. Jamet, E. Jacquet, J. M. George, A. Barthélémy, H. Jaffrès, A. Fert, M. Bibes, and L. Vila, "Highly efficient and tunable spin-to-charge conversion through rashba coupling at oxide interfaces," *Nature Materials*, vol. 15, no. 12, pp. 1261–1266, 2016.

[174] Q. Song, H. Zhang, T. Su, W. Yuan, Y. Chen, W. Xing, J. Shi, J. Sun, and W. Han, "Observation of inverse edelstein effect in rashba-split 2deg between srtio3 and laalo3 at room temperature," *Science Advances*, vol. 3, no. 3, 2017.

[175] M. B. Jungfleisch, W. Zhang, J. Sklenar, W. Jiang, J. E. Pearson, J. B. Ketterson, and A. Hoffmann, "Interface-driven spin-torque ferromagnetic resonance by rashba coupling at the interface between nonmagnetic materials," *Phys. Rev. B*, vol. 93, p. 224419, Jun 2016.

[176] Y. Niimi and Y. Otani, "Reciprocal spin hall effects in conductors with strong spin–orbit coupling: a review," *Reports on Progress in Physics*, vol. 78, p. 124501, oct 2015.

[177] S. Sangiao, J. M. De Teresa, L. Morellon, I. Lucas, M. C. Martinez-Velarte, and M. Viret, "Control of the spin to charge conversion using the inverse rashba-edelstein effect," *Applied Physics Letters*, vol. 106, no. 17, p. 172403, 2015.

[178] I. Mertig, "Transport properties of dilute alloys," *Reports on Progress in Physics*, vol. 62, pp. 237–276, jan 1999.

[179] W. Luo, W. Y. Deng, H. Geng, M. N. Chen, R. Shen, L. Sheng, and D. Y. Xing, "Perfect inverse spin hall effect and inverse edelstein effect due to helical spin-momentum locking in topological surface states," *Phys. Rev. B*, vol. 93, p. 115118, Mar 2016.

[180] Y. Shiomi, K. Nomura, Y. Kajiwara, K. Eto, M. Novak, K. Segawa, Y. Ando, and E. Saitoh, "Spin-electricity conversion induced by spin injection into topological insulators," *Phys. Rev. Lett.*, vol. 113, p. 196601, Nov 2014.

[181] M. Jamali, J. S. Lee, J. S. Jeong, F. Mahfouzi, Y. Lv, Z. Zhao, B. K. Nikolić, K. A. Mkhoyan, N. Samarth, and J.-P. Wang, "Giant spin pumping and inverse spin hall effect in the presence of surface and bulk spin-orbit coupling of topological insulator bi2se3," *Nano letters*, vol. 15, p. 7126—7132, October 2015.

[182] A. Nomura, T. Tashiro, H. Nakayama, and K. Ando, "Temperature dependence of inverse rashba-edelstein effect at metallic interface," *Applied Physics Letters*, vol. 106, no. 21, p. 212403, 2015.

[183] W. Zhang, M. B. Jungfleisch, W. Jiang, J. E. Pearson, and A. Hoffmann, "Spin pumping and inverse rashba-edelstein effect in nife/ag/bi and nife/ag/sb," *Journal of Applied Physics*, vol. 117, no. 17, p. 17C727, 2015.

[184] H. Nakayama, H. An, A. Nomura, Y. Kanno, S. Haku, Y. Kuwahara, H. Sakimura, and K. Ando, "Temperature dependence of rashba-edelstein magnetoresistance in bi/ag/-cofeb trilayer structures," *Applied Physics Letters*, vol. 110, no. 22, p. 222406, 2017.

[185] G. Lampel, "Nuclear dynamic polarization by optical electronic saturation and optical pumping in semiconductors," *Phys. Rev. Lett.*, vol. 20, pp. 491–493, Mar 1968.

[186] W. Heil, H. Humblot, E. Otten, M. Schafer, R. Sarkau, and M. Leduc, "Very long nuclear relaxation times of spin polarized helium 3 in metal coated cells," *Physics Letters A*, vol. 201, no. 4, pp. 337 – 343, 1995.

[187] L. E. Golub, "Weak antilocalization in high-mobility two-dimensional systems," *Phys. Rev. B*, vol. 71, p. 235310, Jun 2005.

[188] H. Du, X. Sun, X. Liu, X. Wu, J. Wang, M. Tian, A. Zhao, Y. Luo, J. Yang, B. Wang, and J. G. Hou, "Surface landau levels and spin states in bismuth (111) ultrathin films," vol. 7, no. 1, 2016.

[189] V. K. Dugaev, P. Bruno, and J. Barnaś, "Weak localization in ferromagnets with spin-orbit interaction," *Phys. Rev. B*, vol. 64, p. 144423, Sep 2001.

[190] F. E. Meijer, A. F. Morpurgo, T. M. Klapwijk, and J. Nitta, "Universal spin-induced time reversal symmetry breaking in two-dimensional electron gases with rashba spin-orbit interaction," *Phys. Rev. Lett.*, vol. 94, p. 186805, May 2005.

[191] V. A. Froltsov, "Diffusion of inhomogeneous spin distribution in a magnetic field parallel to interfaces of a iii-v semiconductor quantum well," *Phys. Rev. B*, vol. 64, p. 045311, Jun 2001.

[192] S. Tenberg, R. P. G. McNeil, S. Rubbert, and H. Bluhm, "Narrowing of the overhauser field distribution by feedback-enhanced dynamic nuclear polarization," *Phys. Rev. B*, vol. 92, p. 195428, Nov 2015.

[193] R. W. Greening, D. A. Smith, Y. Lim, Z. Jiang, J. Barber, S. Dail, J. J. Heremans, and S. Emori, "Current-induced spin–orbit field in permalloy interfaced with ultrathin ti and cu," *Applied Physics Letters*, vol. 116, no. 5, p. 052402, 2020.

[194] B. Khodadadi, A. Rai, A. Sapkota, A. Srivastava, B. Nepal, Y. Lim, D. A. Smith, C. Mewes, S. Budhathoki, A. J. Hauser, M. Gao, J.-F. Li, D. D. Viehland, Z. Jiang, J. J. Heremans, P. V. Balachandran, T. Mewes, and S. Emori, "Conductivitylike gilbert damping due to intraband scattering in epitaxial iron," *Phys. Rev. Lett.*, vol. 124, p. 157201, Apr 2020.

[195] D. A. Smith, A. Rai, Y. Lim, T. Q. Hartnett, A. Sapkota, A. Srivastava, C. Mewes, Z. Jiang, M. Clavel, M. K. Hudait, D. D. Viehland, J. J. Heremans, P. V. Balachandran, T. Mewes, and S. Emori, "Magnetic damping in epitaxial Iron alloyed with vanadium and aluminum," *Phys. Rev. Applied*, vol. 14, p. 034042, Sep 2020.

[196] S. Emori, C. Klewe, J.-M. Schmalhorst, J. Krieft, P. Shafer, Y. Lim, D. A. Smith, A. Sapkota, A. Srivastava, C. Mewes, Z. Jiang, B. Khodadadi, H. Elmkharram, J. J. Heremans, E. Arenholz, G. Reiss, and T. Mewes, "Element-specific detection of sub-nanosecond spin-transfer torque in a nanomagnet ensemble," *Nano Letters*, vol. 0, no. 0, p. null, 0. PMID: 33084344.

Appendices

Appendix A

Improved Bi Deposition System

Before our group started to fabricate Bi films on mica and Si(111), we used to grow it on SiO_2, and the highest sample temperature needed for this process was 250 °C. To grow Bi on Si(111) which needs up to 1200 °C sample temperature (to flash off the SiO_2 layer and to prepare the Si(111)-7×7 reconstruction), an upgrade to the functionality of the temperature control system was needed, as well as a new Bi growth stage capable of stable temperature control up to 1250 °C in UHV conditions, as shown in Figure A.1(a). The UHV button heater is inside a custom-built stain steel holder, to connect the heater stage with the flange, an intermediate ring was designed for the heater lead and thermocouple. To isolate the heater lead without touching the holder, we used ceramic beads fitted around the heater wire, as shown in Figure A.1(b).

We describe how to operate the Bi deposition system below.

- Make sure the system is vented. Remove the sample stage flange bolts and nuts. Carefully and vertically lift the sample stage flange and cover the opening with clean cloth to avoid dust.
- While holding the whole flange upside down, place the sample on the surface of the button heater and tighten it with the clip (*if a shadow mask is needed, fully cover the sample with the mask, and tighten them with the clip*). Try to avoid adjusting the screws on the button heater holder and the intermediate ring. Flip the flange to make sure the sample is stable and won't drop off. Check the thermocouple and the heater lead, certify that they are connected properly and not shorted.
- Use a flash light to check if the Bi source in the chamber is sufficient for evaporation. To supply more Bi source, disassemble chamber by pulling out the source boat flange (charger side with two black cables) and place Bi nuggets into the boat with a pair of tweezers, in the meanwhile replacing the copper gasket.
- Insert the flange back onto the chamber, mark which lead is the positive heater lead and tighten the nuts/bolts symmetrically.
- Check to see if the quartz balance monitor is functional, then turn it off.
- Turn on the rotary pump, when the pressure gauge shows below 10 milliTorr, turn on the turbomolecular pump through the panel (*If the pressure does not reach 10*

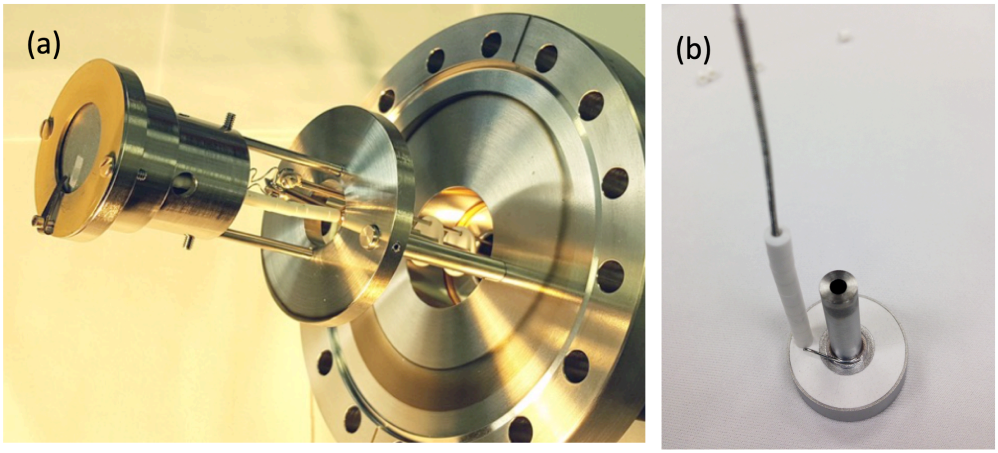

Figure A.1: (a)Specialized Bi growth stage capable of accepting 1“ ⌀ substrates and capable of stable temperature control up to 1250 °C in UHV environment. (b) UHV button heater with ceramic beads around the heater wire.

milliTorr, do not turn on the turbomolecular pump, check where the leak is). Wait for about 5 min until the turbomolecular pump starts running. The pressure should decrease rapidly to around 10^{-6} Torr range, until the turbomolecular pump speed is steady and maximal. Check for leaks if the pressure doesn't behave as expected.

- Bake the chamber by turning on the chamber ribbon heater voltage to 135 V. Slowly turn on the sample stage heater to a certain current value to anneal the substrates:
  - If the substrate is mica, the value is around 2.2 A, and the temperature should reach 250 °C. Bake out the substrate for 24 hours before slowly turning off the sample stage heater and the chamber heater.
  - If the substrate is Si(111), the certain value is around 3.5 A, and the temperature should reach 600 °C. Do not turn on the sample stage heater until after baking the chamber for at least 19 hours. After annealing Si(111) for 5 hours, slowly turn the sample stage heater to 8 A. Once the sample temperature reaches 1150 °C, turn the sample heater back to 7 A to flash-heat Si(111) for 2 min. Turn the sample heater to about 5 A, wait until the substrate temperature drops to 900 °C. From 900 °C to room temperature, the temperature dropping rate should be < 2 °C, so slowly turn off the sample heater. It is safe to fully turn off the sample heater when the substrate temperature decreases to around 500 °C. Meanwhile turn off the chamber heater.

  While the substrate is at its annealing temperature (e.g., 250 °C for mica, 600 °C for Si(111)), rotate the shutter to cover only the sample stage while leave the quartz balance exposed to Bi evaporant. Turn off the chamber heater (to avoid tripping the fuse), and slowly turn on the source heater to about 60-70 V. Evaporate around 10-15

nm thick Bi to outgas the source. Slowly turn off the source heater, and turn on the chamber heater again to 135 V. By covering only the sample, not only can we safely clean the source, also we can stabilize the growth rate before deposition on the substrates. When the shutter is set to 20°, both the sample and the quartz balance are shielded; at 0°, the sample is protected, while the quartz balance is exposed; and at 330°, both the sample stage and the quartz balance are exposed.

- Let the system pump with all heaters off to cool down the substrate until room temperature, and the pressure will drop to 10^{-9} Torr range.
- Move the shutter to expose both the substrate and the quartz balance. Slowly turn on the source heater to about 63 V to evaporate Bi on the substrate. Wait for the desired thickness.
- Stop the Bi film evaporation and start annealing process. Heat up the sample to about 90-100 °C (about 1.5 A shown on the sample stage heater) and anneal for an hour.
- Once the temperature of the sample stage reaches below 50 °C, vent the chamber. The two cylinder valves and the manual valve on the system need to be opened. Turn off the turbomolecular pump, wait for about 10 min until the electronically-controlled valve is opened by the system, then turn off the rotary pump. When the yellow light on the turbomolecular pump stops flashing, close all three valves.